Interactions in the Ultracold Lithium - Ytterbium $^3P_2$ System

William H. Dowd

A dissertation submitted in partial fulfillment
of the requirements for the degree of

Doctor of Philosophy

University of Washington

2015

Reading Committee:

Subhadeep Gupta, Chair

Boris Spivak

Blayne Heckel

Program Authorized to Offer Degree: Physics

University of Washington

Abstract

Interactions in the Ultracold Lithium - Ytterbium $^3P_2$ System

William H. Dowd

Chair of the Supervisory Committee:
Associate Professor Subhadeep Gupta
Physics

I detail the execution and results of experiments in a mixture of ultracold atomic gases using fermionic lithium (^6Li) and bosonic ytterbium (^{174}Yb) in the metastable $^3P_2$ state. We demonstrate efficient transfer of ground state Yb atoms to this metastable state in the presence of Li. A method to spin-purify the resulting metastable Yb atoms via a magnetic gradient is presented. We investigate intra-species and inter-species inelastic collisions over a wide range of magnetic fields. The resulting inelastic spectrum is linked to a potential collisional resonance between the $m_J = -1$ metastable state of Yb and ground state Li near 450G. This work begins the path towards creation of trapped ultracold and magnetic ground state molecules. Such molecules allow experiments which cannot be accessed by current generations of bi-alkali molecule experiments.

TABLE OF CONTENTS

LIST OF FIGURES

LIST OF TABLES

ACKNOWLEDGMENTS

I saved the writing of these acknowlegements for the last entry in my thesis, and I now find myself somewhat at a loss for words. As I think back on my career here at the University of Washington I feel a bittersweet nostalgia. These past seven years have held a tremendous variety of experiences both wonderful and aggravating. It has been a rocky road at times, and I nearly left the program to pursue other interests. Throughout these years, good and bad, there have been many people who have helped tilt the scales in my favor.

First, I must give a spirited thanks to my advisor Subhadeep Gupta. Deep has been wonderful in every regard and I find it hard to imagine a better person to work for and with. I often think back to an occasion early in my career where one of the other graduate students and I were wrestling with a problem, the details of which escape me now but probably involved the lithium MOT, for what seemed like hours on end. Just as we were giving up, Deep entered the lab to check on things and after a few questions promptly found and fixed the problem. I often found myself relying on Deep's seemingly limitless knowledge as I floundered in the dark. In addition to expertise in the lab, Deep has an incisive view of our experiment in particular and the field in general. I have learned much about physics due to Deep's tutelage, and I am forever in his debt.

I have had the privilege to work with an amazing cast of fellow graduate and post-graduate students during my time in the Deep lab. They have helped me to grow both as a physicist and as an individual. In no particular order, they are:

Alex Khramov who introduced me to maté, old new years, and an eclectic musical

selection. Alex is an ever present source of interesting conversation whether it be about physics or mushroom hunting. In addition to being an adept physicist, Alex is also a consummate linguist and seems to know more languages than should really even exist. One scarcely remembers they have little interest in etymology until well after a three hour conversation with Alex on the origins of a phrase.

Continuing the journey into foreign languages, I learned perhaps the most useful phrase in all of physics from Vladyslav Ivanov: blyat. This phrase encompasses all the grief and anger caused by a terrible, irreversible, mistake you have just made. I am happy to say the phrase has not made it into my everyday vocabulary through overuse, though mostly because alternative English words usually spring to mind first.

Anders Hansen and I always seemed to approach a problem from opposite ends. This often had the benefit of meeting in the middle and occasionally of missing each other entirely. Outside of the lab, Anders and I share a love of board games which culminated in many "games nights" where many nights of fun were had. Anders' connoisseurship of beer helped introduce me to the one and only IPA which does not taste like a rotten shoe, and for that I also thank him.

Alan Jamison and I share a dislike of IPA's, but for that I think I may have gone mad with doubt in the IPA drenched northwest. In addition to his excellent taste, Alan is an incredible physicist and a joy to work with in the lab, even with "Everyone I love is... dead" playing in the background (or indeed because it is).

The majority of the data presented in this thesis was collected by myself and Richard Roy over the course of many long nights filled with caffeine, horrid pizza, and laser unlocks. Ricky developed an affinity for the notorious 404nm laser which I could never get the knack for. This has likely saved us many months in data acquisition, and certainly what remains of my hair. Ricky has proven himself to be an excellent physicist and I feel confident in the lab's future success in handing the

reins over to him.

I would also like to thank Ben Plottkin-Swing, Rajendra Shrestha, and Alaina Green for their contributions to the lab. I did not spend as much time with them, but I am certain they will be wonderful assets for the lab in the coming years.

Last, but certainly foremost, I must thank my beautiful wife Beth. She has been a loving and steadfast presence during my time in graduate school. Without her support this thesis would almost assuredly not exist today.

Chapter 1

INTRODUCTION

Ultracold dilute gases offer a flexible system in which to perform studies of quantum degenerate gases [1, 2], simulation of condensed matter Hamiltonians [3], and precision measurements [4, 5, 6].

The pioneering work of several groups in the mid 1980's [7, 8, 9] demonstrated the ability to control the external degrees of freedom of an atom with lasers and magnetic fields interacting with the atom's internal configuration. Since then, a flurry of experiments using these techniques have been constructed. Initial efforts focused on the alkali metal atoms which are well suited to these techniques, and resulted in the first trapped Bose-Einstein condensates in rubidium and sodium [10, 11] and later degenerate Fermi gases in potassium [12].

The list of elements which can be cooled to the quantum degenerate regime has grown substantially in the intervening ~ 20 years. Notably, the alkaline-earth atoms have proven amenable to the same techniques as the alkali metals. These atoms feature extremely narrow intercombination transitions which are the basis for atomic optical clock experiments [13, 14, 15]. The metastable states accessed by these intercombination transitions also provide the ability to change the atom's behavior in the presence of external fields e.g. ground state alkaline earth bosons are magnetically insensitive while one of these metastable states is not.

Many of these systems also provide the capability of tunable interactions via magnetic Feshbach resonances [16]. The power and flexibility provided by this mechanism cannot be overstated. It has been used to incredible effect for studying Bose-Einstein condensates in the strongly interacting regime [17], for creating BCS-like superfluidity

states in degenerate Fermi gases [18], and for efficient ultracold molecule creation [19] to name a few applications.

It is this latter application, creation of ultracold molecules, which is the primary topic of this thesis. Ultracold molecules provide new degrees of freedom to interact with in our systems: rotational and vibrational excitations and potentially strong DC electric polarizability in heteronuclear two-atom molecules.

Creation of ultracold molecules is not a simple task. To date, only bi-alkali and homonuclear molecules have been transfered to their ground state in the ultracold regime [20, 21, 22, 23, 24]. Attempts to directly cool molecules, rather than assemble them from ultracold atoms, are also underway and showing promising results [25, 26, 27]. However, these efforts still have many technical hurdles to solve in order to reach the ultracold regime.

Our system is an ultracold atomic mixture experiment using the alkali atom lithium together with the alkaline-earth-like atom ytterbium. The ground state of LiYb molecules will feature a magnetic dipole moment which is absent from ground state bi-alkali molecules.

1.1 Dissertation Organization Information

This dissertation details the interactions of a novel ultracold atomic system at the University of Washington and the techniques used to produce that system. Our system of lithium and ytterbium offers the ability to produce ultracold ground state molecules with both a magnetic and electric dipole moment. This combination of attributes, while not unique to the lithium ytterbium system, has not yet been developed in other systems. Such molecules would provide access to a wealth of new experimental techniques and opportunities e.g. simulation of condensed matter lattice spin models [28]. This dissertation's primary thrust is measuring the inelastic interactions between lithium and an electronically excited metastable state of ytterbium. The lithium-metastable ytterbium interactions support Feshbach resonances which

may allow efficient creation of molecules via a process called magneto-association [29]. The presence of a Feshbach resonance can be deduced by measuring a peak in the inelastic interactions as a function of magnetic field. The results of our investigations into this system indicate that such a Feshbach resonance may occur in the ^{6}Li -^{174}Yb $^3P_2$ system near 450G. The details of this experiment are the subject of chapter 6.

The rest of the dissertation is organized as follows. Chapter 2 details the components of the vacuum apparatus and electromagnets in our apparatus. Chapter 3 gives an overview of the lithium and ytterbium atoms and the important electronic transitions we use to manipulate them. Chapter 4 describes the techniques used to cool and trap our atoms to ultracold temperatures. Chapter 4 also details the absorption imaging technique we use to measure the results of our cooling and trapping efforts. Examples and a brief description of the quantum degenerate gases of lithium and ytterbium that can be produced in our lab are found in chapter 4 as well. Chapter 5 gives an experimentalist's (yours truly) introduction to the theory of ultracold atomic interactions, including an overview of Feshbach resonances and the various forms they can take in our lithium-ytterbium system. Also presented here, for completeness, are the very first experiments with our ultracold mixture in which we measure the elastic interaction cross section of the ground state lithium-ytterbium system. These experiments are described in detail in the theses' of Anders Hansen [30] and Alex Khramov [31].

Chapter 2
EXPERIMENTAL APPARATUS

I joined the lab in the spring of 2009, shortly before the lab's first successful creation of an ultracold gas of ytterbium atoms. Many, if not all, of the important choices concerning the physical construction of the apparatus had already been made and implemented by the existing group. Here, I discuss some of the more important aspects and subsequent upgrades. Exhaustive information can be found in the theses of Anders Hansen [30] and Alex Khramov [31] who were the lead graduate students during this time. It would be remiss of me to not also mention Ryan Weh, Lee Willcockson, Billy English, and Kalista Smith who all made important contributions to the apparatus construction and lab in general during its formative years.

The vacuum apparatus features a main chamber, pictured in Figure 2.1, connected by hollow tubes (termed Zeeman slowers) to two atomic ovens. Hot atoms from atomic ovens speed down the Zeeman slowers to the main chamber where they are trapped, cooled, and taught the polka. The entire system sits on a stainless steel optical table which limits the effects of vibrations in the system.

2.1 Vacuum System

The atomic gases we wish to study are inherently fragile objects. Even a glancing collision between a room temperature molecule and an atom in our gas is enough to remove said atom from the gas. It is imperative to minimize these interactions between our gas and the surrounding environment.

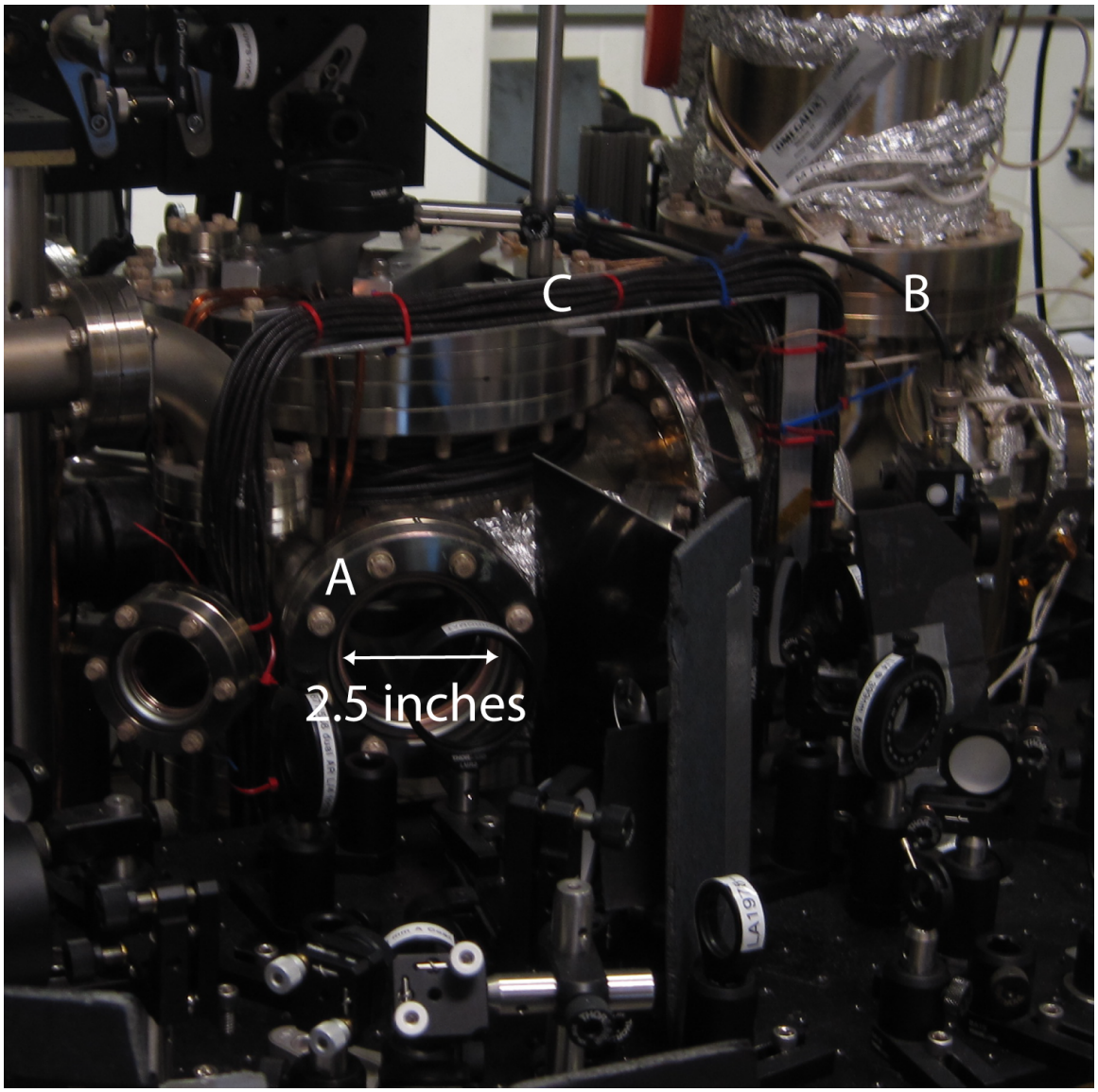

Figure 2.1: The main chamber in which we trap and cool lithium and ytterbium atoms. A) Viewport through which imaging light and the optical dipole trap enter the chamber. B) Adjacent chamber housing the ion and titanium sublimation pumps. C) Compensation coils used to cancel ambient and fringing magnetic fields along the ytterbium slower axis.

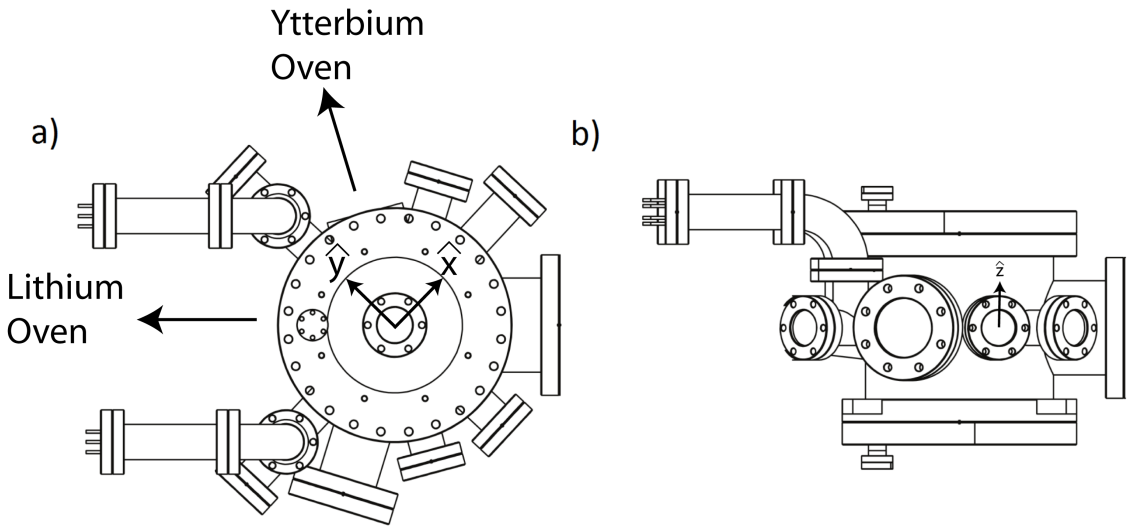

Figure 2.2: Main vacuum chamber schematic as seen from above (a) and the side (b). This and other schematics in this chapter are courtesy of Lee Willcockson.

2.1.1 Main Chamber

Isolation from the surrounding environment is achieved by performing our experiment within the confines of an ultra-high vacuum chamber. Typical pressures in the chamber, as measured by an ion gauge (Varian), during the experiment are $< 10^{-10}$Torr. The vacuum is maintained by a 75 L/s ion pump (Gamma vacuum) and titanium sublimation pump.

The main chamber was custom built by Sharon Vacuum. It is a hollow closed cylinder constructed from type-304 stainless steel. About the cylinder are twelve ports providing access to the chamber as shown in Fig 2.2. The ports are arranged in pairs providing a path through the center of the vacuum chamber. Three pairs provide optical access from the $\pm\hat{x}$, $\pm\hat{y}$, and $\pm\hat{z}$ directions. An additional pair gives

optical access in the xy plane aligned 12 degrees from the $\hat{x}$ axis. The final two pairs of ports, also in the xy plane, are configured to provide optical access on one side and Zeeman slower tubes connecting to the atomic ovens on the other.

The two glass ports directly across from the slower tubes are manufactured from sapphire glass. Flux from the atomic ovens adsorbs on to these viewports and so ruins their optical properties. The excellent thermal properties of sapphire glass allows us to maintain them at 200^{o}C, and so remove much of the adsorbed atoms. The other optical ports are manufactured from BK7 glass and feature broadband anti-reflection coating in the visible spectrum and narrowband anti-reflection coating for 1064nm light. The resulting transmission probabilities for important wavelengths in our lab are: 99.9% at 1064nm, 98.5% at 671nm, 99.8% at 556nm, and 95% at 399nm.

Two of the viewports extrude further from the main chamber in order to accomodate an elbow connector as shown in Fig 2.2. The ion gauges we use to measure the main chamber pressure reside in these elbow connections.

2.1.2 Atomic Ovens and Beamlines

The apparatus employs separate beamlines for our two atomic species, giving the experiment maximum flexibility at the expense of four (rather than two) main chamber ports dedicated to the cause of the Zeeman slowers. This flexibility is important as optimal Zeeman slowing conditions (see Ch. 4) are quite different for lithium and ytterbium. Having dedicated beamlines allows each one to be independently optimized-to whit, they have different lengths and magnetic field profiles.

Separate beamlines also allow us to "turn off" atomic flux from one species during single species experiments and calibration. Similarly, this allows us to break vacuum at the oven assembly for one species while experiments continue with the other species.

A final, unforeseen, benefit is avoiding chemical reactions between the atomic species and the vacuum assembly. The gaskets which exist between vacuum components are typically made from copper. However, at high temperatures copper tends

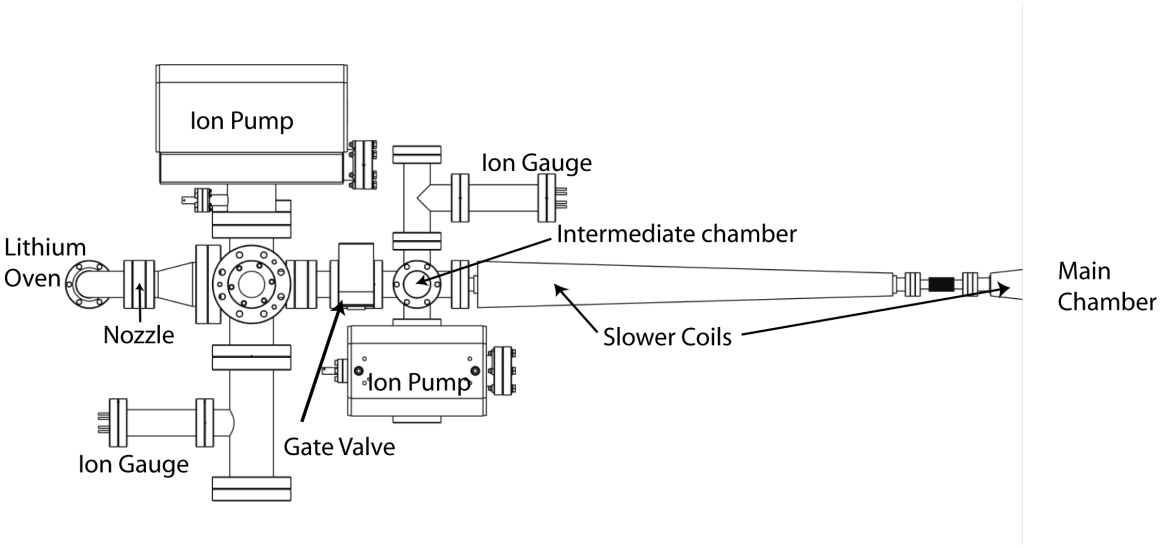

Figure 2.3: The lithium zeeman slower and oven assembly as seen from above.

to seize in the presence of lithium[32]. We use nickel gaskets in the lithium beamline to avoid this issue. However, nickel reacts with ytterbium, resulting in vacuum leaks in the first iteration of the oven design[31, 30] and forced the experiment to halt while vacuum was broken and the gaskets replaced. The separated design allows us to use copper gaskets in the ytterbium beamline and so avoid these unpleasant interruptions.

The two beamlines and oven assemblies are nearly identical save for the gaskets, electromagnets (see next section) and lengths; a schematic of the lithium assembly is shown in Figure 2.3. A small sample (25-50g) of metallic lithium (ytterbium) is heated to 400 C resulting in a small atomic vapor pressure around 10^{-7}Torr. A small fraction of the atoms in the vapor will travel along the tube connecting the oven assembly and main vacuum chamber; this is the atomic flux we will slow and trap. A 4mm nozzle aperture at the ovens and an 11cm long by 5mm diameter differential pumping tube between the oven and the "intermediate chamber" serve to collimate the atomic flux.

Connected to the beamline are two six-way crosses (see Fig. 2.3). Each of these is instrumented with an ion pump, which together with the narrow connecting tubes, allows us to maintain 10^{-10}Torr in the main vacuum chamber while the atomic oven pressures can be as high as 10^{-7}Torr. The pressure at these chambers is monitored by an ion gauge and is typically 1–2 $\times$ 10^{-9}Torr when the ovens are hot.

The chamber closer to the atomic oven has a mechanical feedthrough which allows us to rotate a small metal plate into or out of the atomic beamline. This allows us to quickly ($\sim$ 100ms) extinguish and revive atomic flux to the main vacuum chamber. Two optical viewports are instrumental in aligning the Zeeman slowing beams (see Ch. 4).

The chamber nearer to the main vacuum chamber has four optical viewports, which are useful for flourescence spectroscopy of the atomic flux. The beamline is also an effectively Doppler-free source of atoms, which is perfectly suited for laser locking purposes. The intermediate chamber viewports give an opportunity to use this source. Another possibility provided by these viewports is to implement a transverse cooling stage before the atoms enter the Zeeman slower, as has been demonstrated [33].

Between the two six-way crosses is a gate valve which, when closed, can maintain ultra-high vacuum on one side while the other is exposed to full atmosphere. While the machine is not in operation, these gate valves remain closed to limit the damage of any catastrophic vacuum loss.

2.2 Electromagnets

One of the simplest methods to interact with neutral atoms (and molecules!) is with a static magnetic field, should the atom (molecule) have a non-zero magnetic moment. The interaction is simple $H_{int} = -\mu \cdot B$ and its magnitude (typically $\sim$ 1.4MHz/G) lends itself to well known and mature technology. Creating simple magnetic fields is

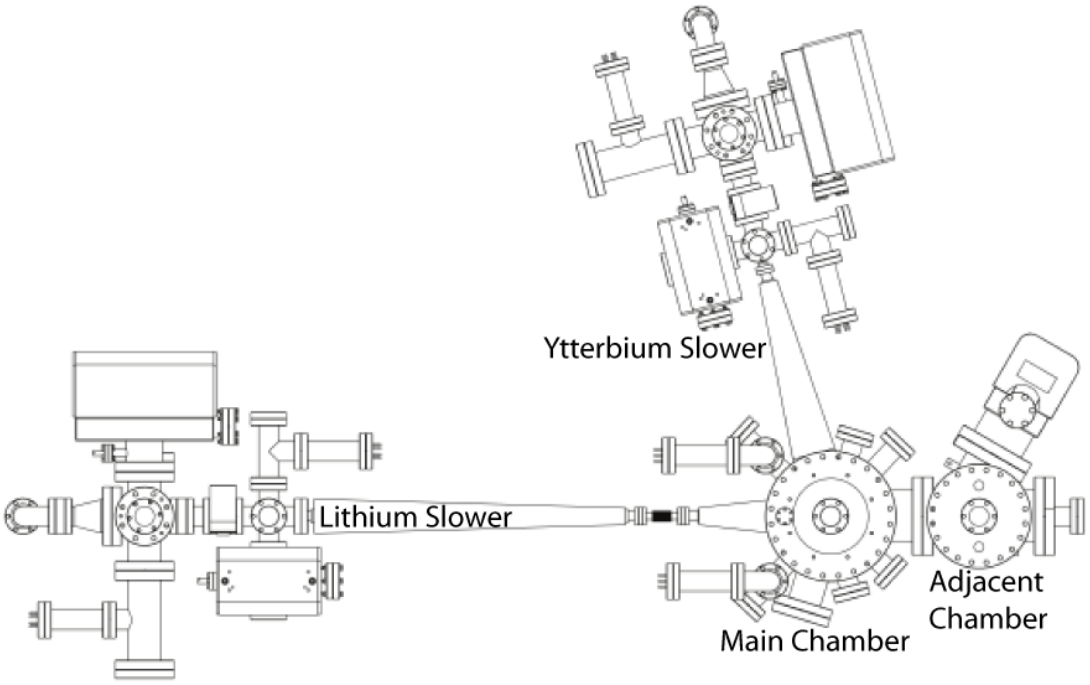

Figure 2.4: Schematic of the main chamber together with the beamlines and oven assemblies as seen from above. The adjacent chamber houses the ion and titanium sublimation pumps which maintain the vacuum.

also rather easy, requiring only a loop of wire and a current source. Our apparatus has nine electromagnets.

2.2.1 Slower Coils

The ytterbium beamline is surrounded by a large solenoid, with turn density tuned to produce a magnetic field profile $\vec{B} = B_0(I)(1 - \sqrt{1 - z/L_0})\hat{z}$. Here, L_0 is the length of the solenoid, z is the position along the solenoid (measured from the atomic oven side), and $B_0(I)$ is 16G at 1 amp. The solenoid is fed by a 30A power supply.

The lithium beamline design uses two solenoids, producing fields in opposite directions. The field profile of the entire slower is $\vec{B} = B_0(I)(0.44 - \sqrt{1 - z/L_0})\hat{z}$. The two solenoid coils producing the $+\hat{z}$ and $-\hat{z}$ fields are electrically isolated and powered by independent 30A supplies. The maximum delta between entrance and exit fields using these power supplies is 980G. The design of these magnetic field profiles is discussed in Ch. 4.

Because of the large currents, these solenoids experience fairly large Ohmic heating. To combat this, the coils are constructed from a hollow wire through which we pump chilled water. A diagnostics and failsafe system was implemented by Anders to prevent melting wires and insulation. For detailed information, I refer you to his thesis (Ch. 6.3 in particular) [30]; for our purposes it is sufficient to know that a "catastrophe regulator" is in place to prevent... catastrophes.

2.2.2 Compensation Coils

The first trapping technique we employ (discussed in Ch. 4) traps atoms at a zero of the magnetic field. Therefore, it is necessary to cancel any ambient magnetic field at the center of the chamber. The fringing fields introduced by the slower coils are the primary source of this ambient field, though other sources such as the Earth's magnetic field and ion pump magnets also contribute. Cancellation is accomplished

quite simply; solenoids are placed around the main vacuum chamber directly opposite of the slower coils. Running current through these compensation coils with the appropriate polarity produces a suitable cancellation magnetic field. These coils are limited to $\sim 15A$ as they are not water cooled, but this is sufficient for our purposes. An additional vertical compensation coil is also present (with a lower $\sim 6A$ rating), however is rarely used as the ambient vertical field is quite small.

2.2.3 (Anti) Helmholtz Coils

Two independent sets of vertically aligned solenoids provide the magnetic fields for interacting with trapped atoms. In the original design, one coil was intended to produce a uniform bias magnetic field (Helmholtz configuration), while the other was to provide magnetic field gradients (anti-Helmholtz configuration). These coils were often referred to as the "Feshbach" or "bias" and "MOT" or "anti-Helmholtz" coils, respectively, in prior works. Experimental necessities have since required us to abandon these constraints; each coil has served as both a Helmholtz and anti-Helmholtz coil. As such, I will refer to them here as the "large inductor" (previously the "Feshbach" coils) and "small inductor" (previously the "MOT" coils) which describes their relative inductance. The important characteristics of these coils are detailed in table 2.1. As these coils will see large currents, they are wound with hollow wire and instrumented as described in the slower coil section (chilled water and catastrophe regulation).

	Bias (G/A)	Gradient (G/cm/A)	Inductance (μH)	Resistance (mΩ)
Large Inductor	4.2	1.8	105	20.0
Small Inductor	2.4	1.0	23	10.8

Table 2.1: Relevant properties for the (Anti) Helmholtz coils[31, 30]. Note that inductances are given in Helmholtz configuration and are significantly smaller in Anti-Helmholtz configuration (and mostly irrelevant).

These electromagnets are driven with two hefty power supplies providing up to 3.3 and 1.0kW of power. In experiments where achieving large magnetic fields is of utmost importance, the more powerful supply drives the large inductor in Helmholtz configuration. This allows the experiment to reach fields as high as 840G for brief periods of time (limited by Ohmic heating constraints). Experiments which instead require fast ramping of the magnetic field have the more powerful supply drive the small inductor in Helmholtz configuration. Controlled ramps of +50G/ms are achievable in this fashion. Quenching of the circuits are handled by insulated gate bipolar transistors (IGBT) and a ringdown circuit with $\sim 300\mu$s time constant.

No matter the experiment we wish to run, a magnetic field gradient is required to employ our trapping techniques (see Ch. 4). Certain experiments (e.g. [34]) require the experiment to reach fields well in excess of 840G. To facilitate fields up to $\sim 1300G$, Anders constructed a switch for the small inductor coils which allow them to convert between Helmholtz and anti-Helmholtz configuration on a 500ms timescale. Beyond this, we are limited by the Ohmic heating within the coils. We can briefly achieve fields as large as 1600G by increasing the flow rate of chilled water through the coils with a booster pump. This, unfortunately, also has a negative effect on system stability, which we have attributed to vibrations from the booster pump being coupled to our optical table. A detailed account of both the switch and additional cooling can be found in Anders' thesis [30].

Two hall probes are used to monitor the current through each coil and gives us a precise measurement of the magnetic field and gradient in the vacuum chamber. Passive control of each current is achieved by an analog voltage input to the respective power supply. The power supply in constant current (voltage) mode attempts to maintain a constant current (voltage) through (across) its terminals determined by the input control voltage.

A concerted effort was made to actively control the current in these electromagnets via feedback. The power supply (in constant voltage mode) is directed to produce

more voltage than necessary to drive the electromagnets at the desired current level. Feedback on the IGBT quenching circuit to gate the additional voltage provides the active control of the system.

Operation of the active current control was attempted to achieve faster ramp speeds. As such, the over-voltage from the power supply was quite large. The resulting ramp speeds are in excess of 150G/ms. However, the large over-voltage leads to dramatic short timescale ($\sim 10ms$) current fluctuations. At large currents, this has a tendency to set fire to the varistors protecting the power supply and IGBT. Tuning of the PID circuit beyond the current capabilities, or a different feedback scheme entirely, are necessary to implement a working active current control system.

2.2.4 RF Antenna

The final electromagnet to be discussed is an RF antenna which resides within the main vacuum chamber, pictured in Figure 2.5. The antenna is two sets of square loops 14cm x 2.5cm separated by 5.4cm. This creates a magnetic field at the atoms of 0.12G per amp of drive current.

The resonant Rabi frequency of magnetic dipole transitions is $\Omega = \mu B/\hbar$. For atoms with magnetic moment equal to the Bohr magneton, RF transition rates are $2\pi \times 180$kHz per amp of current. The antenna is rated for up to 5.5A.

An 80MHz frequency synthesizer (BK Precision) followed by an RF amplifier is used to drive the antenna.

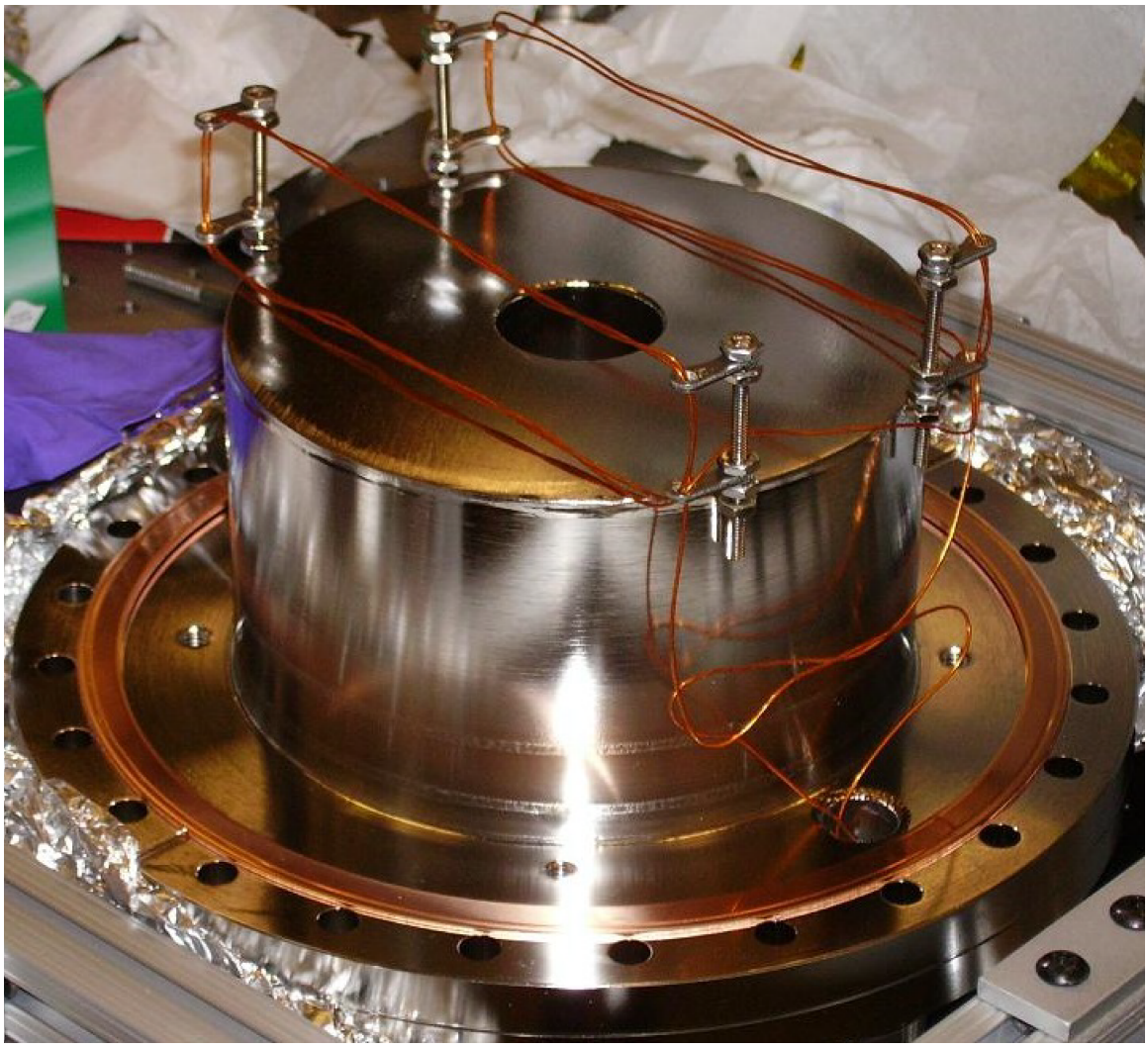

Figure 2.5: The RF antenna which resides within the vacuum chamber (this picture taken before final chamber assembly).

Chapter 3

THE LITHIUM AND YTTERBIUM ATOMS

The lithium and ytterbium atoms are the fundamental building blocks of our experiment. This chapter serves as an introduction to these atoms. All relevant optical transitions used in this experiment are collected in Table 3.1 for quick reference.

Transition	Wavenumber (cm^{-1})	Width (MHz)	Saturation Intensity (mW/cm^2)
Li D2	14904.00	5.87	2.54
Yb $^1P_1$	25068.22	28.9	59.5
Yb $^3P_1$	17992.007	0.182	0.138
Yb $^3D_2$	24751.922	—	—
Yb $^3P_2$	19710.388	—	—
Yb* $^3S_1$	12984.30	12	3.43
Yb' $^3S_1$	15406.25	12	5.74

Table 3.1: Important properties of the lithium and ytterbium electronic transitions used in this experiment. Yb (Yb*) (Yb') represents the ground (metastable $^3P_2$) (metastable $^3P_0$) state. The ground to $^3D_2$ and $^3P_2$ transitions are not dipole and do not have a conventional width or saturation intensity.

3.1 Lithium

Lithium is a naturally occurring element with two stable isotopes: ^6Li and ^7Li with 7.5% and 92.5% natural abundance, respectively. Our experiment is tooled for the fermionic isotope ^{6}Li , which is the subject of this section. Future experiments with ^7Li are possible with minor alterations to the experiment.

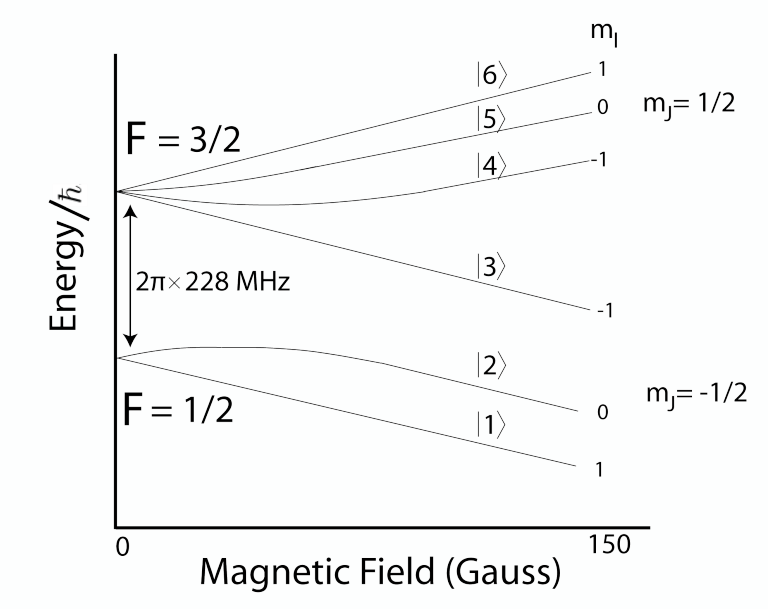

Figure 3.1: Lithium ground state energy as a function of magnetic field.

3.1.1 ^{6}Li *Ground State Structure*

Ground state ^{6}Li has one valence electron in the 2S orbital ($L = 0, S = 1/2$) and a nuclear spin I=1. At low magnetic fields ($< 50G$), the total atomic angular momentum $F = I + J$ is a good quantum number and results in a manifold with $|F, m_f\rangle$=$|3/2, m_F\rangle, |1/2, m_F\rangle$. At large magnetic fields ($> 150G$), the electronic spin decouples from the nuclear spin and $|J, m_J\rangle \times |I, m_I\rangle$ is the proper basis to describe the atom. Figure 3.1 illustrates the ground state spectrum in a magnetic field.

As there are no crossovers, these states are canonically labelled $|1\rangle$ (lowest energy) through $|6\rangle$ (highest energy) rather than by the relevant $|F, m_F\rangle$ or $|J, m_j; I, m_I\rangle$ quantum numbers; a convention I continue here.

Coherent state transfer between states can be achieved with an RF pulse tuned to the (magnetic field dependent) transition frequency.

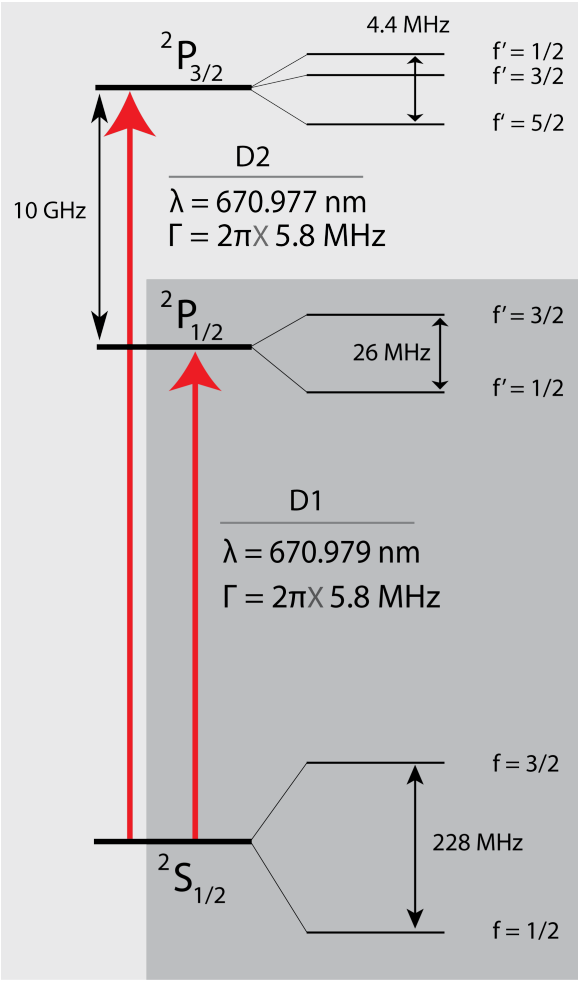

Figure 3.2: Lithium 671nm optical transitions we can address with our laser system. The D2 transition is used in this experiment.

3.1.2 Optical Transitions

We use the lithium $1S^2 2S^1 \rightarrow 1S^2 2P^1$ transition near 671nm which is illustrated in Figure 3.2. The $1S^2 2P^1$ configuration has fine structure splitting resulting in $J = 3/2$ and $J = 1/2$ levels. The transitions to these levels are labelled the D2 and D1 transitions, with $h \times 10GHz$ splitting. The $^2P_1$ states are further split by the hyperfine

interaction resulting in F=5/2,3/2,1/2 and F=3/2,1/2 substates for the $J = 3/2$ and $J = 1/2$ levels, respectively. The hyperfine splitting in the excited $J = 3/2$ state is smaller than the natural linewidth and so this substructure is unresolved. This has the unfortunate side effect that the $|F = 3/2, \pm 3/2\rangle \rightarrow |F' = 5/2, \pm 5/2\rangle$ transition is not cycling, as minor polarization imperfections will excite the $|F = 3/2, \pm 3/2\rangle \rightarrow |F' = 3/2, \pm 3/2\rangle$ transition, which may decay to the $|F = 1/2, \pm 1/2\rangle$ state. These atoms must then be repumped to the F=3/2 manifold to continue addressing them on the original transition.

The D2 transition features prominently in our experiment; it is used for slowing (Section 4.1), cooling (Section 4.2), and absorption imaging (Section 4.4) our lithium atoms. The D1 transition is unused; however future experiments may exploit the D1 transition to implement the novel "Gray Molasses" cooling scheme recently demonstrated [35, 36].

3.1.3 Lithium Lasers

A commercial external cavity diode laser plus tapered amplifier system (TOptica Photonics) which produces 340mW of power provides the bulk of the D2 transition light. One additional laser diode (PowerTech) produces another 35mW of 671nm light.

Acoustic optic modulators (AOMs) induce a modest (60-1600 MHz) frequency offset to a laser beam and are a major workhorse in our lab. The frequency (typical bandwidth of 1.5 times the central AOM frequency) and amplitude (0–$\sim$ 80% conversion rate) of the resulting beam is controllable on microsecond timescales. Ample use of these devices allows us to create many beams from a single source; of particular note, we can access the D2 transition from both the $|F = 1/2\rangle$ and $|F = 3/2\rangle$ lithium ground states with the same laser source despite the 228MHz difference in transition frequency.

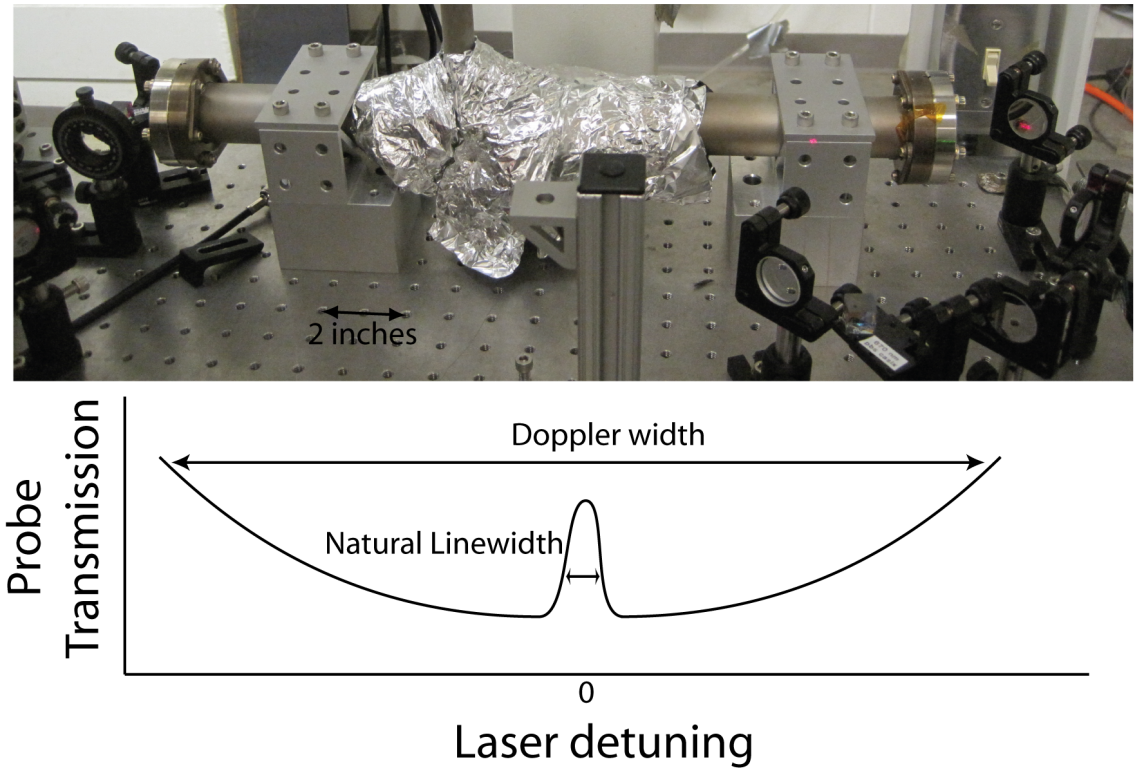

Figure 3.3: (top) The lithium vapor cell in which the saturated absorption spectroscopy occurs. A reflection from the transmitted pump beam is visible on the first mirror to the right of the vapor cell. (bottom) The probe-beam transmission through the vapor cell as a function of its detuning from the transition resonance with a strong pump beam of the same frequency.

The primary laser is locked to the lithium D2 transition frequency via a saturated absorption spectroscopy lock[37]. A sample of lithium heated to 420^{o}C provides a small partial pressure of lithium atoms in a 40cm long vapor cell as pictured in Figure 3.3. Two laser beams counter-propagate through the cell. Each beam is absorbed by a narrow velocity class of atoms determined by the beam's detuning from atomic resonance. When the beams interact with the same velocity class of atoms (0 velocity atoms when the beams have the same frequency), the absorption effect is reduced for each beam due to a reduced ground state fraction. By making one of these beams much stronger than the other (termed the pump beam), absorption in the other beam (termed the probe beam) is minimized in this overlap region. Scanning the frequency of the beams (via an AOM) produces a peak in the probe transmission signal, shown in Figure 3.3. The derivative of this signal is a suitable error signal to which we lock our laser.

An interesting additional feature termed the crossover peak can occur in atoms with hyperfine structure. A crossover peak occurs when the ground (or excited) state is resonant with the pump beam on one transition and the probe beam on another transition. For pump and probe beams with the same frequency, this crossover peak occurs halfway between the two transitions and involve atoms with velocity which exactly cancels the detuning with the doppler shift. If the thermal sample supports these velocities, the crossover peak can be much stronger than the fundamental as it can address twice as many atoms (atoms travelling in either direction). The ^{6}Li D2 velocity class for identical frequency pump and probe beams is a pedestrian $77m/s$ and well within range of our 420^oC thermal sample. As such, the lithium laser is locked to the crossover peak mid-way between the $|F = 3/2\rangle$ and $|F = 1/2\rangle$ D2 transitions.

As the offset frequency of an AOM is scanned, the efficiency is altered due to

changes in the Bragg matching condition and the static alignment of the beam with the AOM. Since this effect is exactly in phase with the saturated absorption signal, the effects are directly seen in the resulting probe transmission signal. For this reason, we use a pump-only modulation scheme which minimizes this power-modulation bleed through to the probe transmission signal. We observe qualitative improvements in the stability of the lithium laser lock after moving to a pump-only modulation scheme. A technical side effect of our lock is that our pump and probe beams do not have the same central laser frequency. The resulting lock is shifted by half the frequency difference between the laser beams (295MHz in our case), and involves a velocity class of atoms shifted by 100m/s.

The second diode laser is slaved to the primary laser with an injection lock using 1mW 732MHz red detuned from the F=3/2 D2 transition and an additional 0.1mW with the same detuning from the F=1/2 D2 transition. This light is used for Zeeman slowing the atoms (discussed in section 4.1). A 3:1 ratio of light would be ideal for this purpose, however the injection lock becomes unstable when moved beyond the 10:1 ratio currently used.

3.2 Ytterbium

Ytterbium is also a naturally occurring element with seven stable isotopes; 2 fermions (Z= 171, 173) and 5 bosons (Z= 168, 170, 172, 174, 176), all except ^{168}Yb having reasonable natural abundance.

Ground state ytterbium has two valence electrons in the 6S orbital ($L = 0, S = 0$). The bosonic isotopes have nuclear spin I=0 making them completely insensitive to magnetic fields in their ground state! The 171 (173) fermionic isotope has nuclear spin I=1/2 (5/2) and associated ground state structure.

It is relatively easy to switch ytterbium isotopes between experiments, requiring

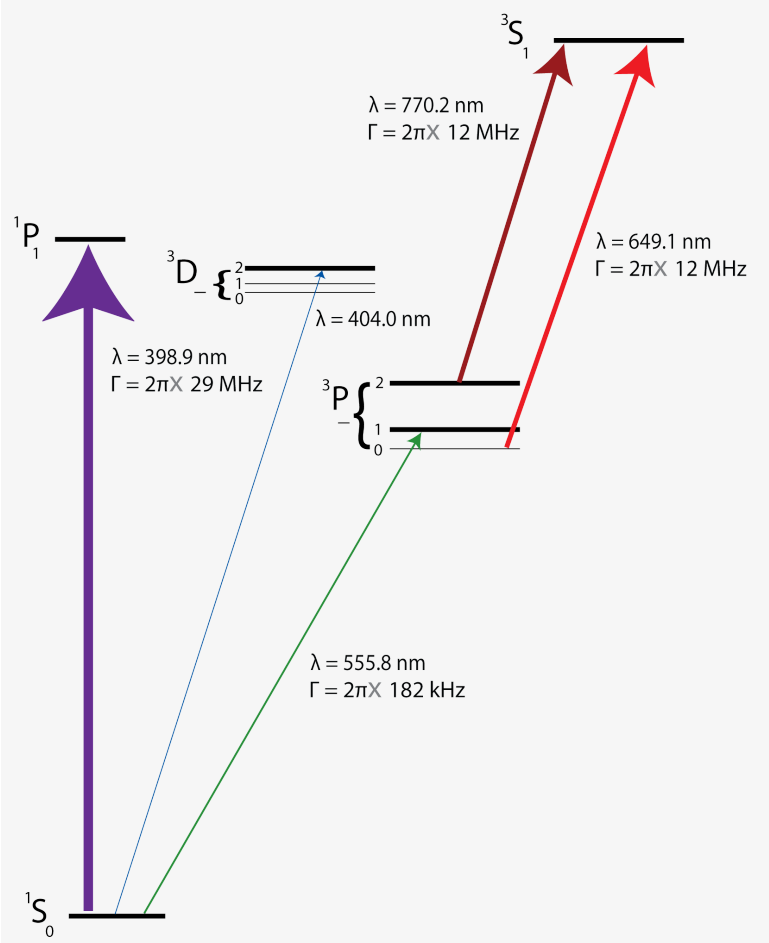

Figure 3.4: The low lying electronic manifold of ytterbium (hyperfine structure occurring in the fermionic isotopes omitted for clarity). Transitions used in this experiment are labelled with their wavelength and natural linewidths. The $^1S_0 \rightarrow ^3D_2$ transition at 404nm is not a dipole transition and does not have a conventional linewidth. The $^3D_2$ state has a natural lifetime of $2\pi \times 350$kHz.

only changes to our laser locks and minor tweaks to electromagnet settings. This flexibility allows our experiment to easily pursue diverse experimental goals such as SU(N) symmetry models [38], Bosonic and Fermionic degeneracy studies, and choice in the quantum statistics for the proposed Li-Yb dimer. The work presented here focuses on the ^{174}Yb isotope which affords us some simplicity in electronic structure compared to the fermionic isotopes, and greater natural abundance and favorable scattering properties compared to the other bosonic isotopes.

3.2.1 Optical Transitions

The strong dipole $6S^2 \rightarrow [6S^1 6P^1]\{^1P_1\}$ line at 399nm is the transition used for Zeeman slowing (Sec 4.1) and imaging (Sec. 4.4) of ytterbium atoms. This transition has a mild $(3 * 10^{-5})$ branching ratio to the $^3D_1$ metastable state[39], but is otherwise a cycling transition. Experiments which also cool on the 399nm transition can take advantage of branching to this metastable state to magnetically trap and cool ytterbium [40].

Our experiment takes a different tack, and cools on the intercombination $6S^2 \rightarrow [6S^1 6P^1]\{^3P_1\}$ line at 556nm. The 556nm transition is much narrower than the 399nm transition (182KHz vs 29MHz). This is vital for a cooling transition as it allows us to achieve much lower MOT temperatures (discussed in Sec. 4.2).

3.2.2 Ytterbium Lasers

The $^1S_0 \rightarrow {}^1P_1$ transition is addressed by a 800nm external cavity diode laser plus tapered amplifier and frequency doubling system (TOptica Photonics) which produces up to 300mW of 399nm laser power. The laser is locked to the transition using a saturated absorption spectroscopy scheme (discussed in Sec. 3.1.3). The locking scheme uses a hollow cathode lamp (Hamamatsu) as the atomic source and the pump-only modulation scheme discussed in Sec. 3.1.3.

The $^1S_0 \rightarrow {}^3P_1$ transition is addressed by an 1112nm diode laser plus tapered amplifier and frequency doubling system (TOptica Photonics) which produces up to 250mW of 556nm laser power. The laser is also locked to the transition using a saturated absorption spectroscopy scheme (see Sec. 3.1.3) using a vapor cell system similar in design to the lithium vapor cell. This transition linewidth is $2\pi \times 182$kHz and so requires a much smaller AOM frequency modulation to achieve a satisfactory saturated absorption signal. Therefore, the coupling between AOM efficiency and frequency is not an issue for this laser lock, and a standard dual pump-probe frequency modulation scheme is suitable for this laser lock.

3.3 Metastable Ytterbium

The nearby metastable $[6S^16P^1]\{^3P_2\}$ state of ytterbium (Yb*) plays a star role in our experiment. Transferring our atomic sample between the ground and metastable state allows us to selectively introduce magnetic lithium-ytterbium interactions to our system. This in turn, allows us to exploit potential Feshbach resonances (see Sec. 5.2) between these atoms and thus alter the system dynamics. The Yb* state has a single body lifetime of 15s [41] and Landé g factor 1.49 [42].

3.3.1 Optical Transitions

Transfer of ground state ytterbium atoms to the metastable state dominates the technical challenge of working with the Yb* state.

Direct transfer to the Yb* state is possible via the extremely narrow 507nm magnetic quadrupole transition. We instead use an indirect transfer scheme described in previous works [43, 44]. This scheme involves exciting ytterbium atoms to the $^3D_2$ state, an electric quadrupole transition at 404nm. The atoms subsequently decay after 0.45μs to the $^3P_1$ and $^3P_2$ states with 88% and 12% probability, respectively. Atoms which decay to the $^3P_1$ state decay back to the ground state with lifetime 0.87μs, where they can be re-excited to the $^3D_2$ state. On average, ytterbium atoms

will end in the $^3P_2$ state after absorbing $8.\bar{3}$ 404nm photons. This transfer scheme populates several Yb* Zeeman substates; these populations are determined by the dipole decay branching ratios listed in Table 3.2.

	$^3P_2$ State				
$^3D_2$ State	$m_j = 2$	$m_j = 1$	$m_j = 0$	$m_j = -1$	$m_j = -2$
$m_j = 2$	2/3	1/3	0	0	0
$m_j = 1$	1/3	1/6	1/2	0	0
$m_j = 0$	0	1/2	0	1/2	0
$m_j = -1$	0	0	1/2	1/6	1/3
$m_j = -2$	0	0	0	1/3	2/3

Table 3.2: Bosonic ytterbium branching ratios from the $^3D_2$ to $^3P_2$ state.

A full derivation of the selection rules and strengths for an electric quadrupole transition can be found e.g. [45]. The transition probability is determined by the atom-radiation interaction Hamiltonian coupling the ground and excited $^3D_2$ states: $\frac{\omega^5}{90c^5\hbar}|\langle\psi_g|D|\psi_e\rangle|$. Here ω is the transition frequency, c is the speed of light, $\langle\psi_g|$ is the ground state electronic wavefunction, $|\psi_e\rangle$ is the excited state electronic wavefunction, and D is the electric quadrupole moment tensor induced by the laser field. Decomposing the planar light field into the vector spherical harmonics $\vec{Y}_{L,M}$ provides a natural connection to the D tensor, where transitions satisfy $\Delta J = \pm L$, $\Delta m_J = M$. The final transition probability depends on the quadrupolar polarizability of the initial electronic wavefunction for the atom in question. Table 3.3 lists the decomposition of a planar light field inducing transitions to the various sublevels of the $^3D_2$ manifold for the two important laser incidence vectors in our experiment.

Transfer of the Yb* atoms back to the ground state for imaging is achieved via the $^3P_2 \rightarrow [6S^17S^1]\{^3S_1\}$ transition at 770nm. This state rapidly (13ns) decays back to the ^3P manifold. Atoms which decay to the $^3P_2$ state are repumped by the

	$\hat{k} \perp \hat{B}$		$\hat{k} \parallel \hat{B}$	
m_j	Strength	Polarization	Strength	Polarization
0	0	–	0	–
1	0.00796	$\hat{e} = \hat{B}$	0.0199	$\hat{e} = \sigma^+$
-1	0.00796	$\hat{e} = \hat{B}$	0.0199	$\hat{e} = \sigma^-$
2	0.228	$\hat{e} = \hat{B} \times \hat{k}$	0	–
-2	0.228	$\hat{e} = \hat{B} \times \hat{k}$	0	–

Table 3.3: Relative transition strengths and required polarizations for the Yb $^3D_2$ transition. Here, $\hat{k}$ is the momentum vector of the photon, $\hat{B}$ is the direction of the magnetic field, and $\hat{e}$ is the polarization vector.

resonant light, while atoms which decay to the $^3P_1$ state subsequently decay to the ground state. Atoms which decay to the $^3P_0$ state can be repumped by exciting the $^3P_0 \rightarrow [6S^1 7S^1]\{^3S_1\}$ transition at 649nm. Should such a light source be unavailable or inconvenient to use, the $^3P_0$ atoms will merrily continue their existence in the $^3P_0$ state for long periods of time ($\sim$ 20s) [46]. The fraction of Yb* atoms which end in the $^3P_0$ state without the 649nm repumping beam has been measured in our experiment to be 0.24(1) [43]. This is in agreement with the 0.26 value obtained from the $^3S_1 \rightarrow {}^3P$ reduced matrix elements calculated in [47].

3.3.2 Lasers for Metastable Ytterbium

The $^3P_2 \rightarrow {}^3S_1$ transition is addressed by a 770nm external cavity diode laser (TOptica Photonics) which produces up to 25mW of laser power of which 4mW is available to drive the atoms. The laser is locked to the transition using a scheme based on saturated absorption spectroscopy. The locking scheme uses a hollow cathode lamp (Hamamatsu) as the atomic source and pump-only amplitude modulation. The resulting laser lock is not a doppler-free spectroscopy lock as used in the laser locks

described previously. Nonetheless, we achieve $50\mu s$ transfers of Yb* atoms back to the ground state with the available 4mW of 770(649)nm laser light; this is more than adequate for our purposes. Full details of this scheme can be found in Anders' thesis [30].

The $^3P_0 \rightarrow {}^3S_1$ transition is addressed by a 649nm external cavity diode laser (TOptica Photonics) which produces up to 25mW of laser power of which 0.25mW is available to drive the atoms. Like the 770nm laser system, this laser is locked using a scheme based on saturated absorption which is detailed in Anders' thesis [30]. This laser system is instrumental for calibrating the $^3S_1 \rightarrow {}^3P_0$ branching ratio, however is not necessary in day to day operations of the experiment.

The $^1S_0 \rightarrow {}^3D_2$ transition is addressed by a 405nm diode laser (Mitsubishi) in a homebuilt external cavity in Littrow configuration. These diodes were originally manufactured for use in commercial BlueRay devices rather than precision laser applications. In the end, we have been successful, but thee diodes have become notorious in the lab for difficulty in tuning the wavelength and lasing in a single-mode. The diodes can produce up to 15mW of power at 100mA drive current in this configuration, but the lasing becomes extremely unstable at this point, staying single-mode for mere minutes. Thus, we run the diode at 65-70mA of current which produces 7mW of power and which remains stable for ~ 1 hour. Of this, 1mW is used to lock the laser, 1mW is available to drive the transition, and the rest is lost to parasitic absorptions and AOM inefficiencies.

A saturated absorption spectroscopy lock is not feasible due to the extremely weak transition strength. Instead, we use a cavity transfer lock [48]. A 1.5GHz Fabry-Pérot cavity (Thorlabs) is locked to the transmission peak of a frequency modulated beam derived from the locked 399nm source. The 404nm laser is then locked to the transmission peak through this length stabilized cavity. A precision wavelength meter (Angstrom High-Finesse) is used to tune the laser within 60MHz of the transition frequency.

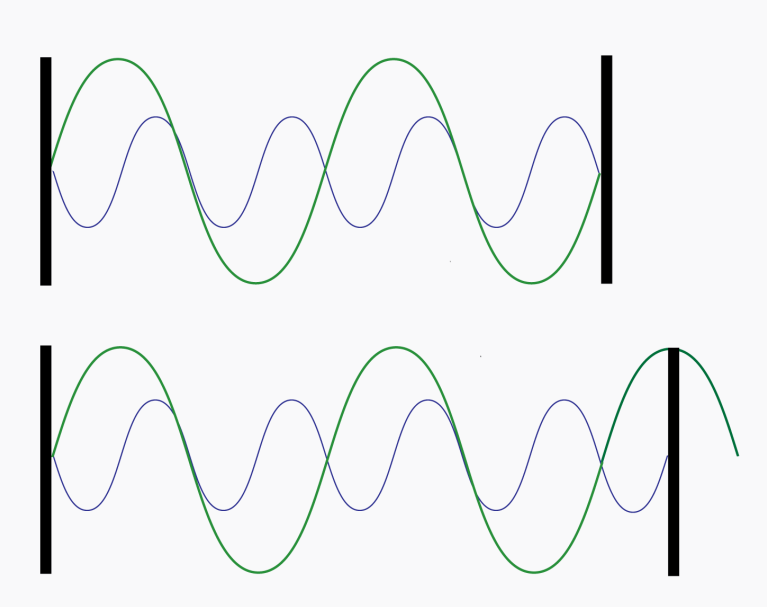

Figure 3.5: Ambiguity in exact frequency achieved using a cavity transfer lock. Extreme exaggeration of the effect experienced by the 399nm $\rightarrow$ 404nm cavity transfer lock is used for clarity (top) A cavity resonant with both 399nm (blue) and 404nm (green) photons in cavity mode n for the blue photons. (bottom) The same cavity moved to the $n' = n + 1$ cavity mode for 399nm photons is no longer resonant with the 404nm photons.

There is ambiguity in the exact frequency achieved for the 404nm laser using such a scheme. This ambiguity is dependent on the precise length of the cavity as illustrated in Figure 3.5. The frequency of the locked 404nm laser will shift by $\sim$ 18.6MHz when the cavity is tuned from the n to $n+1$ cavity mode for 399nm light. For this reason, we must perform a resonance scan every time the cavity lock fails. Such resonance scans indicate that our 404nm laser lock is $\sim$ 3MHz wide. It is unclear which component is limiting the performance of this lock.

A perfect cavity lock transfers the stability of one locked laser source to a second laser. We attempted to improve the 404nm laser linewidth by using the 556nm laser source, which is locked to a line 160 times narrower than the 399nm laser source.

Unfortunately, there was no improvement in the 404nm linewidth or lock stability. Anecdotal evidence suggests that the instantaneous 404nm laser-width is much narrower, and that noise on the 6-7ms timescale "bounces" the lock between its two endpoints. Many days of effort have been dedicated to finding the source of such noise, to no avail.

Chapter 4
COOLING AND TRAPPING

The technical pathways to cooling and trapping neutral atoms have become well travelled over the past 20 years. Research into novel and effective cooling and trapping mechanisms continues to this day [35, 49], but the main thrust of atomic physics research instead cools and traps as a prerequisite to achieve some other goal. Our experiment is no exception; nevertheless cooling and trapping remain ***the*** essential tools upon which we scaffold the rest of our experiment. Here I discuss the techniques and specific parameters used in cooling and trapping the atoms in our experiment.

4.1 The Zeeman Slower

The first step in creating our ultracold gas of atoms is to slow them to manage-able speeds: it is awfully hard to get a handle on atoms rocketing around at 1700m/s, the speed of a typical lithium atom at 450^{o}C!

The Zeeman slower nozzle and differential pumping tubes pre-select atoms with very small transverse velocities. The resulting un-slowed atomic flux has a momentum distribution proportional to $p_z e^{-p_z^2/2mKT}$ where p_z is the momentum along the slower tube, m is the mass of the atom and T is the temperature. The factor of p_z multiplying the familiar thermal distribution accounts for faster atoms overtaking slower atoms "released" at an earlier time.

Slowing is achieved by bombarding the atoms with counter-propagating resonant photons. Each time an atom absorbs a photon it receives a momentum kick $\hbar k$; here k is the wavevector associated with the photon. While these individual momentum kicks are small, even on the atomic scale, the scattering rate can be extremely large.

The resulting force on the atoms is

$$F_{slow} = \hbar k \Gamma_{scatter} = \hbar k \frac{\Gamma}{2} \frac{I/I_s}{1 + I/I_s + 4\delta^2/\Gamma^2} \tag{4.1}$$

where k is the photon wavevector, $\Gamma_{Scatter}$ is the total scattering rate, Γ is the natural linewidth of the transition, I is the beam intensity, I_s is the saturation intensity for the transition, and δ is the photon detuning from resonance in the atomic reference frame. For zero detuning and $I/I_s = 3$, this corresponds to accelerations of 10^4 and $2 * 10^5$ m/s^2 for ytterbium on the $^1P_1$ transition and lithium on the D2 transition, respectively.

Implementing a Zeeman slower then becomes an issue of manufacturing a way to keep the detuning close to zero as the atoms rapidly change velocity, and therefore the observed photon frequency due to the Doppler effect. This is not an insignificant effect, corresponding to $\sim$ 3GHz and $\sim$ 1GHz frequency shifts for lithium and ytterbium, respectively.

Assuming a constant detuning and beam intensity over the length of our Zeeman slower, the velocity of atoms which remain in resonance for the entire length of the slower is

$$V(z) = \sqrt{V_0^2 - 2az} \tag{4.2}$$

where V_0 is the velocity which is Doppler shifted into resonance at the beginning of the slower, a is the acceleration, and z is the distance over which the atoms have been slowed. Atoms initially slower (faster) than V_0 will eventually (never) fall into resonance with the Zeeman slower as illustrated in Figure 4.1.

We achieve zero detuning over the Zeeman slower for atoms with an initial velocity V_0 using a magnetic field with spatial profile

$$B(z) = \frac{\hbar k}{\Delta \mu} \sqrt{V_0^2 - 2az} + B_0 \tag{4.3}$$

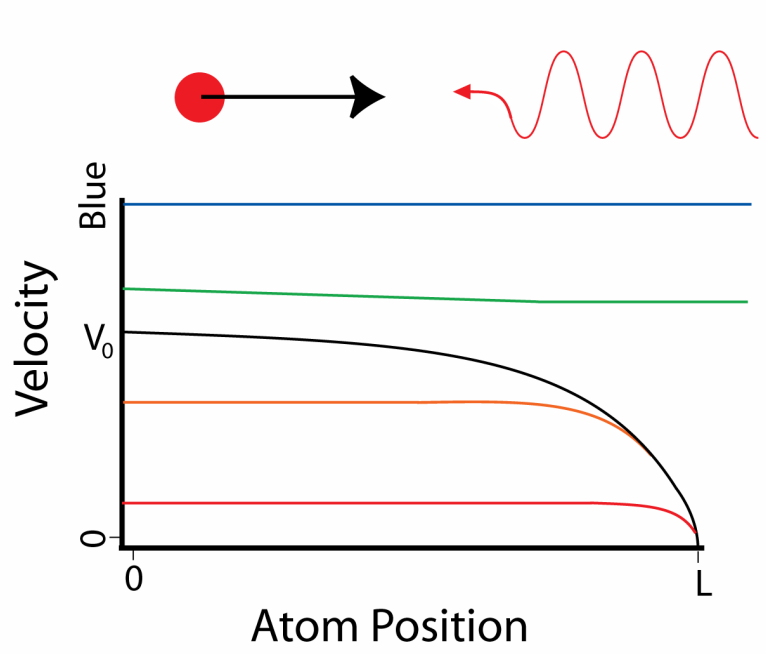

Figure 4.1: Atoms entering the Zeeman slower at velocity V_0 follow the velocity curve in Equation 4.2. (black curve). Atoms with initial velocity smaller than V_0 will eventually fall into resonance with the Zeeman slower and so be slowed (orange and red curves). Atoms with initial velocity greater than V_0 will never be in resonance with the Zeeman slower and continue through the slower mostly unaffected (green and blue curves).

where k is the rest frame transition wavevector, $\Delta\mu$ is the difference in magnetic moment of the ground and excited states, and B_0 is some arbitrary offset.

The major Zeeman slower design choice is in selecting the optimal maximum velocity atoms to slow. Targetting a larger V_0 requires a longer length slower. The larger V_0 slows a larger fraction of the incident atomic flux. However, the longer length also reduces the total atomic flux, as more trajectories end in collisions with the tube walls. Additionally, atoms with larger initial velocities must scatter more photons to be slowed. The emission portion of the scattering process contributes 0 average momentum to the atoms. However, this is a random walk process, and the final perpendicular momentum is expected to have a distribution with $\sqrt{N}\hbar k$ standard deviation, where N is the total number of photons scattered. Therefore, atoms with larger initial velocities are less likely to exit the Zeeman slower with trajectories taking them to the center of the vacuum chamber, where they can be captured by the trap. This effect is termed Zeeman bloom.

Another design choice is in selection of the offset magnetic field B_0. There are two points to consider here: detuning of the slower beam, and magnetic field generation. It is advantageous for the slower beam to have a large detuning from resonance, as the beam will interact weakly with the trapped atoms at the center of the vacuum chamber. Maximum detuning is achieved when $B_0 = -\hbar k V_0/\mu$. This arrangement is termed an increasing field slower as it starts at 0 field and increases to maximum value at its terminus. The ytterbium slower in this experiment is an increasing field slower.

Generation of the slower fields is done via an electromagnet, which dissipates power as I^2R. As large magnetic fields require large currents and many coil windings (large resistance), the power dissipation becomes an important consideration. The power dissipation can be reduced significantly by using a profile which begins at $\sim +\Delta B/2$ and ends at $\sim -\Delta B/2$. This type of slower, which goes through a zero crossing in field, is termed a spin-flip slower; the resonant transition begins as $m_F = F \rightarrow m'_F = F+1$

and at the zero crossing flips to $m_F = -F \rightarrow m'_F = -F - 1$. It is important to note that the atoms do not perform a spin-flip in the lab frame, but that the quantization axis has been rotated 180^o. The lithium slower is a spin-flip design due to the large V_0 (and so large magnetic fields) which must be addressed (created).

The lithium (ytterbium) Zeeman slower is operated with a target $V_0 = 920(135)$m/s which requires a 980(240)G change in magnetic field over the 75(40)cm total length. The lithium atoms traverse an additional 18cm region connecting the positive and negative field portions of the slower. The slower is driven with 22(100)mW of light 732(365)MHz red detuned from the F=3/2 D2($^1P_1$) transition. An additional 2mW of light 732MHz detuned from the F=1/2 D2 transition is used to repump lithium atoms from the F=1/2 to F=3/2 state.

The slowed atomic flux exiting the Zeeman slower has a minimum velocity determined by equating the linewidth of the slowing transition with the Doppler shift: $\Gamma = kv_{doppler}$. This limit is 24(12)m/s for lithium (ytterbium) atoms. Operating the Zeeman slower with such small exit velocities is not advisable for two reasons. First, half the slow atomic flux will have negative velocities and be travelling back towards the ovens. Second, the transverse velocity due to Zeeman bloom is $\sim$ 4(0.5)m/s for lithium (ytterbium) atoms. The atom flux will have an increased width at the trapping center of $L\sin(\arctan(v_{doppler}/v_{bloom}))$ with L the distance from the Zeeman slower exit to the trapping center. This results in increased sizes of 4(1)cm at the trap for the lithium (ytterbium) flux. Larger exit velocities will reduce this effect, and may lead to superior trap capture due to spatial overlap considerations.

4.2 The Magneto-Optical Trap

The slow atom flux entering the main vacuum chamber is trapped and cooled in a Magneto-Optical Trap (MOT)[50]. MOTs are a workhorse for many atomic physics laboratories, providing the first stage of strong cooling resulting in gases of millions to billions of atoms with microkelvin regime temperatures.

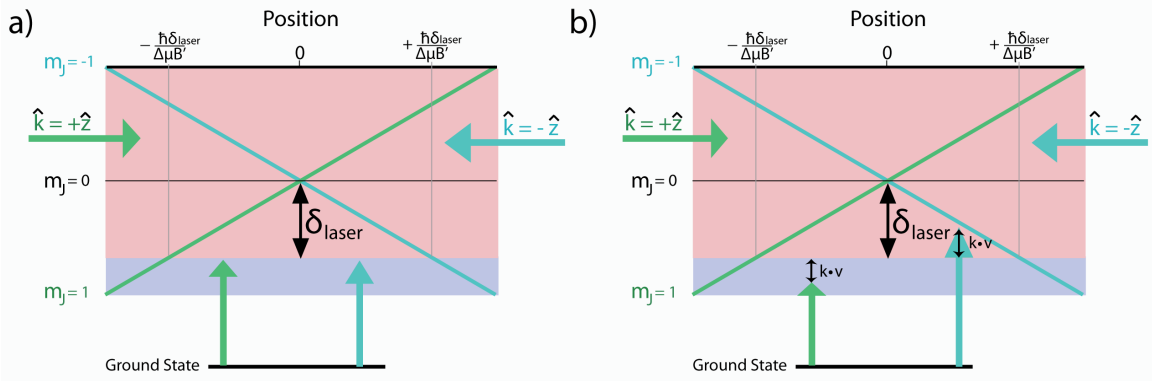

Figure 4.2: Diagram of the ytterbium magneto-optical trap action in 1-D. (a) A magnetic field gradient splits the $m_J = -1$ and 1 Zeeman sublevels of the $^3P_1$ state, represented by the teal and green diagonal lines, respectively. Atoms at positive (negative) positions relative to the zero of the magnetic field are tuned into resonance with the red-detuned laser light for the $m_J = -1(1)$ transition. Carefully selecting the polarization of the two laser beams to be σ^- and σ^+, here represented by the teal (σ^-) and green (σ^+) arrows, will provide a net force towards the zero of the magnetic field. (a) The lab-frame picture for atoms with zero velocity. (b) The lab-frame picture for atoms moving to the right with speed v. The Doppler effect blue(red)-shifts the beam with $-\hat{k}(+\hat{k})$ wavevector. The atom is thus more likely to scatter a photon from the $-\hat{k}$ beam and gain a recoil momentum $-\hbar k$ and thus slow down.

4.2.1 Principles of MOT Operation

The action of the ytterbium MOT in 1-D is illustrated in Fig. 4.2. Two counterpropagating beams of light are aligned to the center of the vacuum chamber and red-detuned from the atomic transition. Atoms travelling towards a beam source are Doppler shifted towards resonance and so more likely to scatter photons from said beam. This results in a velocity dependent force on the atoms termed an optical molasses[8], and is the principle behind the cooling action of the MOT. While the atoms are slowed in a molasses, they will perform a random walk in position; eventually exiting the area of the finitely sized molasses beams. We must introduce a force on the atoms which is also dependent on position to successfully trap them.

By adding a magnetic field with profile $\vec{B}(z) = B'z\hat{z}$, the transition is Zeeman shifted as the atom travels away from $z = 0$. Each beam's polarization is selected to excite only the transition which is red-shifted on the beam source side. In this way, the atoms experience a central restoring force as well as a velocity dependent force. The total force on the atoms in 1-D can be written as

$$F_{MOT} = \hbar k \Gamma \frac{I}{I_s} \left[\frac{1}{1 + 2I/I_s + 4{\delta_1}^2/\Gamma^2} - \frac{1}{1 + 2I/I_s + 4{\delta_2}^2/\Gamma^2} \right] \tag{4.4}$$

where δ_1 and δ_2 are the velocity and position dependent detuning from resonance for the two beams and I is the intensity for both beams. Where we write the δ_1 and δ_2 terms as

$$\begin{aligned} \delta_1 &= \Delta\mu_1 B'z/h + \dot{z}k - \delta_{laser} \\ \delta_2 &= \Delta\mu_2 B'z/h - \dot{z}k - \delta_{laser} \end{aligned} \tag{4.5}$$

Where $\Delta\mu_{1(2)}$ is the difference in magnetic moment between the ground and two excited states, B' is the magnetic field gradient, k is the transition wavevector, and δ_{laser} is the detuning from resonance (without fields and Doppler shifts).

Extending the MOT into three dimensions is achieved by adding similar beams and magnetic fields from the $\hat{x}$ and $\hat{y}$ directions. The magnetic field can be generated by a set of anti-Helmholtz coils, which produce magnetic fields $\vec{B}(x, y, z) = B_0\big(x\hat{x} + y\hat{y} - 2z\hat{z}\big)$ near the zero at the center of the structure.

4.2.2 MOT Performance

In addition to the atom-laser dynamics defined in Eqn 4.4, loss processes related to atom+atom and atom+background-gas collisions define the performance of the MOT. We will eventually wish to transfer the atoms from our MOT to a conservative trapping potential (described in the next section). This transfer process requires MOTs with low temperatures and large densities. On the other hand, atom+atom loss processes increase as the square of the spatial density; large laser detunings (and

therefore MOT temperatures) are ideal for capturing higher velocity atoms exiting the Zeeman slower. These competing interests cause us to operate our MOTs in two stages: the loading MOT, and the compressed MOT.

The loading MOT is optimized to capture the incoming atomic flux as well as minimize the loss process due to atom+atom collisions. The loading rate is determined by a quantity termed the capture velocity: the velocity above which atoms will pass through the MOT slowed, but untrapped. The true capture velocity is determined by integration of Eqn. 4.4 across the trapping region; a difficult task. Instead, we note that the loading MOT typically operates with $I/I_s \gg \delta^2/\Gamma^2$. A useful approximation in this regime (the co-atom propagating beam does not contribute to dynamics and omission of the δ^2/Γ^2 term) makes integration of the equations very simple. The resulting (overestimate) of the MOT capture velocity is

$$V_{cap} = (\hbar k \Gamma d/2m)^{1/2} \tag{4.6}$$

where k is the MOT photon wavevector, Γ is the MOT transition width, and d is the size of the MOT trapping region. The trapping region is defined by the size of the light beams; we value this so strongly that we intentionally throw away laser power through clipping on some optical components to maximize the trapping region. The size of the trapping region (1 cubic centimeter) yields an approximate $V_{cap} = 130(4.7)$m/s for Li(Yb) atoms.

The other concern for the loading MOT are the two-body loss processes that may occur when an excited state atom collides with another MOT-trapped atom. This process scales as the number density squared and so maximizing the size of the MOT will minimize its effects. The size of the MOT scales inversely with the magnetic field gradient. Thus, we should like a small magnetic field gradient to minimize such losses. A minimum magnetic gradient is required to create a trap sufficiently strong to capture atoms in the first place.

The compressed MOT (C-MOT) trades loading rate and lifetime considerations for

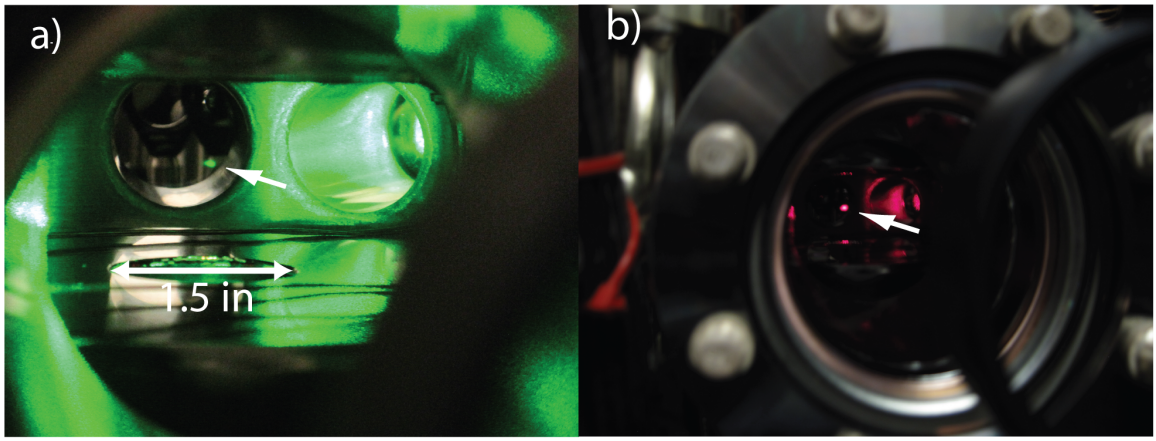

Figure 4.3: (a) Picture of the ytterbium loading MOT containing $\sim 10^8$ atoms at $\sim 500\mu$K. (b) Picture of the lithium loading MOT containing $\sim 5 \times 10^8$ atoms at ~ 4mK.

reduced temperature and spatial extent. This is achieved by increasing the magnetic field gradient and reducing the laser detuning. In order to maintain manageable loss rates, the light intensity is also reduced significantly in the C-MOT.

The minimum temperature that can be achieved in the lithium and ytterbium C-MOTs is limited by the so called Doppler limit, which is $T_{min} = \hbar\Gamma/2k_B$ where Γ is the linewidth of the MOT transition, and k_B is Boltzmann's constant. This is the primary impetus for running the ytterbium MOT on the $^3P_1$ transition which has a Doppler limited temperature of 4.5μK compared to 700μK for the $^1P_1$ transition.

It should be noted that resolved hyperfine structure allows the Doppler limit to be exceeded using the polarization gradient cooling scheme [51]. Unfortunately, this is not an option for lithium or bosonic ytterbium. An additional exciting development is the demonstration of a "gray" molasses on the lithium D1 line, which has allowed sub-Doppler cooling[35, 36]. This technique may be exploited in future work to further cool lithium.

Up to 115(110)mW of laser power is available to operate the lithium (ytterbium) MOT. The laser power is split into three beams and steered to the center of the vacuum chamber from three orthogonal directions. Polarization control of these beams is achieved via broadband polarizing beam splitters and dual-wavelength $\lambda/4$ waveplates. After exiting the vacuum chamber the beams are retro-reflected to create the necessary counter-propagating beam. An additional dual-wavelength $\lambda/4$ waveplate is used to achieve the correct polarization of the retro-reflected beam. It is important to note that approximately 25mW of the 115mW of lithium D2 light is resonant with the $F = 1/2 \rightarrow F' = 3/2$ transition in order to repump atoms which decay to the otherwise "dark" $F = 1/2$ state.

Optimal MOT loads are achieved with $\delta_{laser} = 6(55)\Gamma$ and $B' = 20(3)$G/cm with the available beam intensities of $I/I_s = 60(750)$ for lithium (ytterbium); the loading MOTs are pictured in Figure 4.3. Compression takes 40(200)ms and smoothly ramps the final values to $\delta_{laser} = 1.5(2)\Gamma$, $B' = 60(18)$G/cm, and $I/I_s = 0.07(0.8)$ for the lithium and ytterbium CMOTs. These CMOTs are strongly optimized to load into the dipole trap, rather than produce excellent CMOT statistics, and as such the temperature and number at the end of the CMOT stage is quite deceiving. Measuring the MOTs approximately 80% through the compression sequence yields CMOTs with $150(30) \times 10^6$ lithium (ytterbium) atoms at $400(30)\mu$K.

One additional optimization is made for the ytterbium loading MOT. The laser detuning is modulated at 150kHz giving a $\pm 20\Gamma$ fluctuation in the detuning from resonance. The larger detuning captures a larger fraction of the slowed atomic flux, while the smaller detuning maintains the necessary trapping force to operate a strong MOT. During the first half of MOT compression, the modulation is smoothly turned to zero.

Due to increased loss rates and vastly different optimal settings, it is not viable to run the loading MOT for both lithium and ytterbium at the same time. Instead, we employ a sequential loading scheme in which first a ytterbium MOT is loaded for up

to 20s, compressed, and loaded into the optical dipole trap. Second, a lithium MOT is briefly loaded for up to 2s, compressed, and loaded into the same optical dipole trap. The very short lithium MOT load time is due to strong loss processes in the ytterbium optical dipole trap during this time. Attempts to shift the lithium loading MOT away from the dipole trap via a small magnetic field offset have had limited success. Because of the brief lithium load, the lithium loading MOT settings are optimized essentially free from the loss mechanics which must normally be considered. As such, experiments which use long lithium MOT loads are unlikely to find these settings suitable.

4.3 The Optical Dipole Trap

The vast majority of cooling has already been achieved at this point, having reduced the temperature from hundreds of Kelvin to the microKelvin regime. We switch to a different trapping scheme to achieve even lower temperatures. The trap we use is an optical dipole trap (ODT). Unlike the MOT, the ODT is a simple conservative potential, and does not actively cool the atoms. Instead, we rely on forced evaporative cooling to achieve the 0.1–10μK temperatures typically obtained in our system. Dipole traps have been discussed in depth in many resources [52, 53].

4.3.1 Principles of Operation

The principle behind the ODT can be described simply: an electric field $\vec{E} \propto cos(\omega t)$ induces an electric dipole moment in an atom $\vec{d} \propto cos(\omega t + \phi)\hat{E}$. The interaction energy between the atom and electric field is then simply $H = -\vec{E} \cdot \vec{d}$. The behavior is then defined by the value of ϕ: 0 results in an attractive interaction and π a repulsive interaction.

The induced dipole is typically extremely small, and so incredibly large electric fields are required to generate effects at the 0.1–1mK scale necessary to capture atoms from our MOTs. The electric field generated at the focus of a powerful laser beam is

sufficient. The strength and sign of the interaction is parameterized by the polarizability α of the atom at the laser frequency ω. Typically, this can be calculated by considering coupling to the nearest one or two strong electric dipole transitions. The strength of the interaction will then be $H = \alpha E^2$, where α is the polarizability of the atom at frequency ω, and the proper time averaging of the electric field strength is conducted. It is often preferable to write this as $H = \alpha I/c\epsilon_0$, where I is the laser intensity, c is the speed of light, and ϵ_0 is the permittivity of free space.

The system can be thought of as a driven harmonic oscillator with natural frequency ω_0 the dipole transition, and driving frequency ω the frequency of the laser beam. The oscillations in such a system are in phase with the driving force if $\omega < \omega_0$ and π radians out of phase if $\omega > \omega_0$. Likewise, the atom-photon interaction will be attractive should the laser be red-detuned from the nearby electric dipole transitions, and repulsive if blue-detuned. Though the dipole trap is very far from resonance, atoms still scatter photons at a rate $\Gamma_{sc} = \frac{H\Gamma}{\hbar\Delta}$, with Γ the width of a nearby electronic transition and Δ the detuning.

The spatial intensity profile of a Gaussian beam focused along the z-axis is

$$\begin{aligned} I(r,z) &= \frac{2P}{\pi w^2} e^{-2r^2/w^2} \\ w(z) &= w_0(1 + z^2\lambda^2/\pi^2 w_0^4)^{1/2} \end{aligned} \tag{4.7}$$

where P is the laser power, w_0 is the $1/e^2$ radius at the focus, and λ is the laser wavelength. Atoms deep within this potential see an approximately harmonic trap with trapping frequencies

$$\begin{aligned} \omega_x = \omega_y &= \sqrt{8\alpha P/\pi c\epsilon_0 m w_0^4} \\ \omega_z &= \omega_x \lambda/\sqrt{2}\pi w_0 \end{aligned} \tag{4.8}$$

where m is the mass of the atom.

The simplest trap, and the first used in our lab, is a single beam tightly focused in the center of the chamber. Single beam traps are extremely robust and require

little to no upkeep. Their downside is that the resulting trapping potential is highly asymmetric. A collimated beam is focused to a size $f\lambda/\pi D$ where f is the focal length of the lens and D is the size of the beam at the lens. As our focusing lens is placed outside the vacuum chamber, the minimum focal length is $\sim$ 200mm resulting in focal sizes tens of microns in extent for reasonable initial beam sizes. The resulting axial trap frequency, ω_z, is then two orders of magnitude smaller than the radial trapping frequencies for typical traps.

This limitation can be overcome by a second dipole trapping beam which is aligned to the same focal location, but along a different axis. Such an arrangement is termed a crossed-beam ODT (XODT). The small axial trap frequency in one beam will be augmented by a large radial trap frequency in the other beam. It is a somewhat tricky task to align two $\sim 20\mu$m foci to the exact same position within the vacuum chamber, and typically takes 1-2 days of dedicated work. All dipole trap optical components are "no-touch" afterwards, as even minor bumps can ruin the alignment.

Additional considerations for XODTs must also be taken. Stimulated two-photon processes in which an atom absorbs from one beam and emits into the other are possible. Mitigation of these effects is crucial to maintain long XODT lifetimes. This can be achieved by either using different wavelength lasers to generate the two dipole traps, or by ensuring the polarizations are perpendicular.

4.3.2 Lithium and Ytterbium in a 1064nm ODT

Our experiment uses a 1064nm fiber laser (IPG Photonics) producing up to 100W of power. The polarizability of lithium (ytterbium) at 1064nm is $2.22(0.950) \times 10^{-39}\mathrm{A}^2\mathrm{s}^4/\mathrm{kg}$. As such, the ODT is 2.3 times stronger for lithium atoms than for ytterbium atoms. In addition, the trapping frequency for lithium is 8.2 times larger than for ytterbium. The polarizability of the $^3P_2$ metastable state of ytterbium is also of crucial interest. However, the coupling between metastable ytterbium and other electronic states is both Zeeman sub-level and laser polarization dependent;

best known values are given in Table 4.1.

$^3P_2$ substate	E⊥B $\times 10^{-39}$A^{2}s^4/kg	E||B $\times 10^{-39}$A^{2}s^4/kg
2	1	0.19
1	0.5	0.99
0	0.4	1.52
-1	0.5	0.99
-2	1	0.19

Table 4.1: Polarizability of $^3P_2$ metastable ytterbium at 1064nm for each Zeeman sub level with the electric field parallel and perpendicular to the quantization axis [43]. Values for E⊥B are approximations from a published plot [54].

Typical dipole trap operation uses 32W of laser power. Initial traps used as much as 60W of power at the laser output. However, this resulted in strong focal shifts and focus size aberrations, an effect we attribute to thermal lensing. With 32W of power, thermal lensing effects are still noticeable but much reduced; lower powers are insufficient to capture from the lithium CMOT. The laser operates without the safety of an optical isolater, which was one of the primary components leading to these thermal lensing issues. As such, extreme care must be taken to prevent strong retro-reflections from any laser optic as they could destroy the laser.

The dipole trap has undergone several major revisions during my tenure in the lab. The single beam trap first used produced insufficient collision rates to achieve quantum degeneracy, one of the first target experiments of the lab. Several XODT configurations which recycled the single beam laser power to derive the second beam were tried. However, these XODTs experienced strong two-photon processes related to imperfect polarization orthogonality and unacceptably difficult alignment procedures

for the second beam. These problems spurred the design decisions for the current XODT design.

The current optics layout for the dipole trap is presented in Fig. 4.4. The trap depth is controlled with an 80MHz AOM (IntraAction), from which we take the +1 diffraction order with 70% maximum efficiency. There appears to be some birefringence in the AOM crystal; a waveplate is used to align the laser polarization to an axis of this crystal which ensures easy polarization control of the exiting beam. A $\lambda/2$ waveplate and thin-film polarizing plate (CVI TFPN-1064-45P) is used to create the two beams of the XODT. In experiments where single beam operation is preferred, we rotate the waveplate to maximize transmission through the polarizer and block the small reflection with a black metal card.

The beams are overlapped and focused to $\approx 20\mu$m at the center of the vacuum chamber at an angle of 20^o. Measurements of the true focus size are surprisingly difficult to obtain. Re-imaging the focus of one beam onto a CCD camera, the focus is measured to be 23μm. However, this method reveals a large astigmatism; the x-axis is focused at a different location than the y-axis. Measurements of the single beam trap frequencies for ytterbium at a known laser power gives a focus size of 19μm. The conclusion we have drawn from these measurements is that our trapping laser beams are not TEM_{00}, and strong reservations should be had when attempting to calculate information relying on that assumption.

The splitting ratio for the XODT is a competition between optimal CMOT loads (single beam trap), lifetime considerations (single beam trap), and trap frequencies (50/50 XODT). An approximate 65/35 ratio seems to lead to the best results. Alignment of the XODT is further complicated by the astigmatic nature of the beams, as the overlap can occur at several valid locations. We choose the "strongest" location by evaporating (see Sec. 4.3.3) in the single beam trap and observe which location

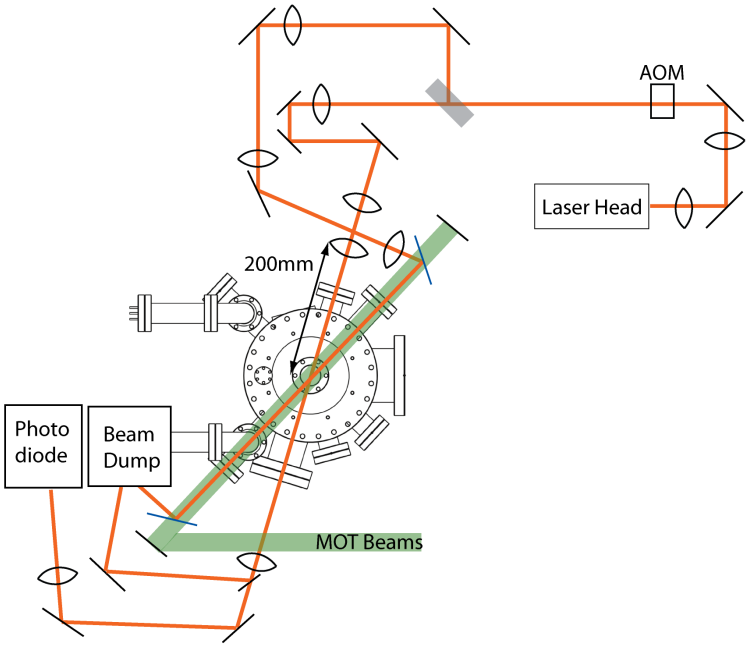

Figure 4.4: Schematic of the optics layout used to create the dipole trap as seen from above. The ODT beam paths (orange lines) are somewhat convoluted due to tight space constraints. An initial 2:1 telescope is used to fit the beam through the AOM aperture. The primary and secondary beams are split by a thin film polarizing plate (gray rectangle). The two resulting beams are re-magnified and focused at the center of the chamber by 200mm (primary beam) and 250mm (secondary beam) lenses. The secondary ODT beam shares an axis with one of the MOT beams (green lines). Dichroic mirrors (blue lines) which reflect 1064nm light and transmit 556nm and 671nm light are used to initially combine and then separate the ODT and MOT beams. Additional optics necessary to safely dispose of the un-diffracted light are not pictured here for clarity.

remains at the lowest trap depths.

Thermal lensing effects also change the focal plane. This is an important effect in an XODT, as the foci will only be well overlapped at a certain thermal load. We choose the best overlap to occur at the lowest trap depths (thermal loads), where the effects of increased trapping frequencies are most important.

A third laser beam at 1070nm (nearly identical polarizabilities) is aligned to the center of the single beam ODT with co-located focus and 90μm $1/e^2$ size. The eventual purpose of this laser beam is to create an optical lattice [55]; in the current experiment, it provides a very small "dimple" trap with radial trapping frequency along the axial direction of the single beam ODT.

The dipole trap has a maximum depth of 2.2(0.92)mK for lithium (ytterbium) atoms. The XODT has a somewhat smaller maximum depth of 1.5(0.65)mK due to additional parasitic absorptions in the optical components of the second beam, as well as imperfect overlap alignment. The lifetime of single beam dipole trapped gases is limited by background gas collisions to $\sim$ 28s. The lifetimes are somewhat reduced in the XODT due to the stimulated two-photon process. This is more properly treated as a heating effect, however evaporation connects heating and loss processes. Lifetimes are typically reduced to $\sim$ 22s, although this depends on the XODT trap depth.

4.3.3 Forced Evaporative Cooling

While the MOT and Zeeman slower are active cooling agents for the atoms, ODTs are conservative potentials. Without interference, we might expect our gas of trapped atoms to never change. The gases do, however, evolve through the process of evaporation.

Evaporation occurs as atoms with velocities sufficient to escape the trap do so. The remaining gas then has less energy per atom and so a lower temperature. Thermalization processes repopulate these large velocities according to the Maxwell-Boltzmann distribution. This evaporative cooling will typically continue until the ratio of trap

depth to temperature reaches ~ 10 –14, where repopulation of the high velocity tail becomes slower than atom loss processes due to background gas collisions. We can force the evaporation process to continue by lowering the dipole trap depth (via the AOM), thereby allowing lower velocity atoms to escape. Continuing this forced evaporation allows us to reach ever lower absolute temperatures.

Precise control over the trap depth is essential in achieving repeatable evaporation results. A standard PID feedback scheme has been implemented to provide this control. The weak transmission of ODT light through a mirror is aligned into a photodiode sensor as depicted in Figure 4.4. The resulting photodiode signal is subtracted from a control signal to obtain an error signal. The error signal is low-pass filtered at 12kHz, integrated, and fed back to the AOM intensity input. In this way, the AOM always attempts to set the output of the laser such that the photodiode signal is equal to the control signal, which is in turn controlled by the experimentalist. The system works very well, providing minute to minute and month to month reliability in trap depths, as well as damping noise below 12kHz. Extension beyond this feedback bandwidth is unnecessary for the dipole trap, but may be required for future projects e.g. a lithium optical lattice.

Detailed investigations into forced and quiescent evaporation in an ODT have been conducted e.g. [56]. As the laser power is reduced during forced evaporation, the trap frequencies are also reduced as detailed in Eq. 4.8. The thermalization rate depends on the trap frequencies, and so the rate of evaporation slows. One can account for this in the evaporation ramp by using a function which slows as evaporation continues e.g. an exponential with negative exponent. The ideal ramps derived in [56] have been used in our experiment to good effect. However, exponential ramps are nearly as effective in our experiment, and the ease of use is cause enough to use them for the majority of experiments.

Evaporation rates scale very strongly with the ratio of trap depth to temperature. Lithium atoms experience a trap 2.3 times deeper than ytterbium atoms: should the

lithium and ytterbium gases remain well thermalized, no lithium atoms will be lost during the forced evaporation process. This "piggyback" cooling process is called sympathetic cooling [57], and is the reason we strongly prioritize initial ytterbium atomnumber over initial lithium atomnumber in the ODT.

4.3.4 ODT Loading and Evaporation Parameters

Atomnumbers and temperatures in the ODT can vary drastically depending on the experimental requirements. A 20s ytterbium MOT load allows us to load up to 5×10^6 atoms at 60μK into our dipole trap. In dual species experiments, this is typically followed by a 1–2s lithium MOT load which results in 50×10^3 lithium atoms at 200μK loaded into the dipole trap. During the lithium load, large numbers of ytterbium atoms in the ODT are lost to evaporative and inelastic loss processes resulting in 1×10^6 ytterbium atoms at 40μK remaining.

Collisions between lithium atoms in the $F = 3/2$ manifold allow strong inelastic loss processes to occur. An immediate strong optical pumping beam resonant with the $F = 3/2$ D2 transition is used to transfer all lithium atoms to the $F = 1/2$ manifold and avoids these processes. The lithium atoms are then in a 50/50 mixture of the $|1\rangle$ and $|2\rangle$ states.

The ODT loads are followed by a 100ms thermalization period before forced evaporation commences. An exponential ramp with a 2.5(1.7)s time constant for single (crossed) beam ODTs is used. An additional thermalization period of up to 2s at the end of evaporation is necessary for the temperatures to fully stabilize. The final trap depth is dependent on the requirements of the experiment being run. Typical operating conditions are a final trap depth of $15(34)\mu$K with $500(50) \times 10^3$ ytterbium (lithium) atoms at 1.5μK in the single beam ODT and $300(35) \times 10^3$ ytterbium (lithium) atoms at 1.5μK in the XODT.

4.3.5 Quantum Degeneracy

Evaporative cooling can be continued until the occupation number of the low lying states approaches 1. At this point, the quantum statistics of the atoms plays an important role. Bosons, such as ^{174}Yb , will aggregate atoms in the lowest available energy state and form a Bose-Einstein condensate (BEC). BECs were first produced in gases of rubidium [10] and sodium [11], a feat which was awarded the Nobel prize in physics in 2001. Identical fermions, such as ^{6}Li and ^{173}Yb atoms in the same substate, are precluded from occupying the same state as one another by the Pauli exclusion principle. Continued evaporation of such a system will form a degenerate-Fermi-gas (DFG). DFGs were first created in gases of potassium [12] and later recreated in many other elements, including lithium [58].

We have demonstrated the ability to make quantum degenerate gases in our apparatus [60], example images and momentum profiles are shown in Figure 4.5. Pure BECs of up to 3×10^5 ^{174}Yb atoms, DFGs of ^{6}Li with 1×10^5 and ^{173}Yb with 1×10^5 atoms, and simultaneous degenerate ^{174}Yb and ^{6}Li gases have been demonstrated in our apparatus [59]. These gases are created in the XODT, as the thermalization rate becomes too small in the single beam ODT. Absorption images (see Sec. 4.4) of these degenerate gases are shown in Fig. 4.5.

4.3.6 Gravity, Magnetic Gradients, and Trap Frequencies

The trapping potential experienced by the atoms is modified by the presence of gravity and magnetic field gradients. The shift in trapping center is easily derived to be g/ω_g^2 and $\mu B'/m\omega_B^2$ with g the acceleration due to gravity, ω_g the trap frequency in the direction of gravity, μ the magnetic moment of the atom, B' the magnetic gradient in the direction of the quantization axis, m the mass of the atom, and ω_B the trap

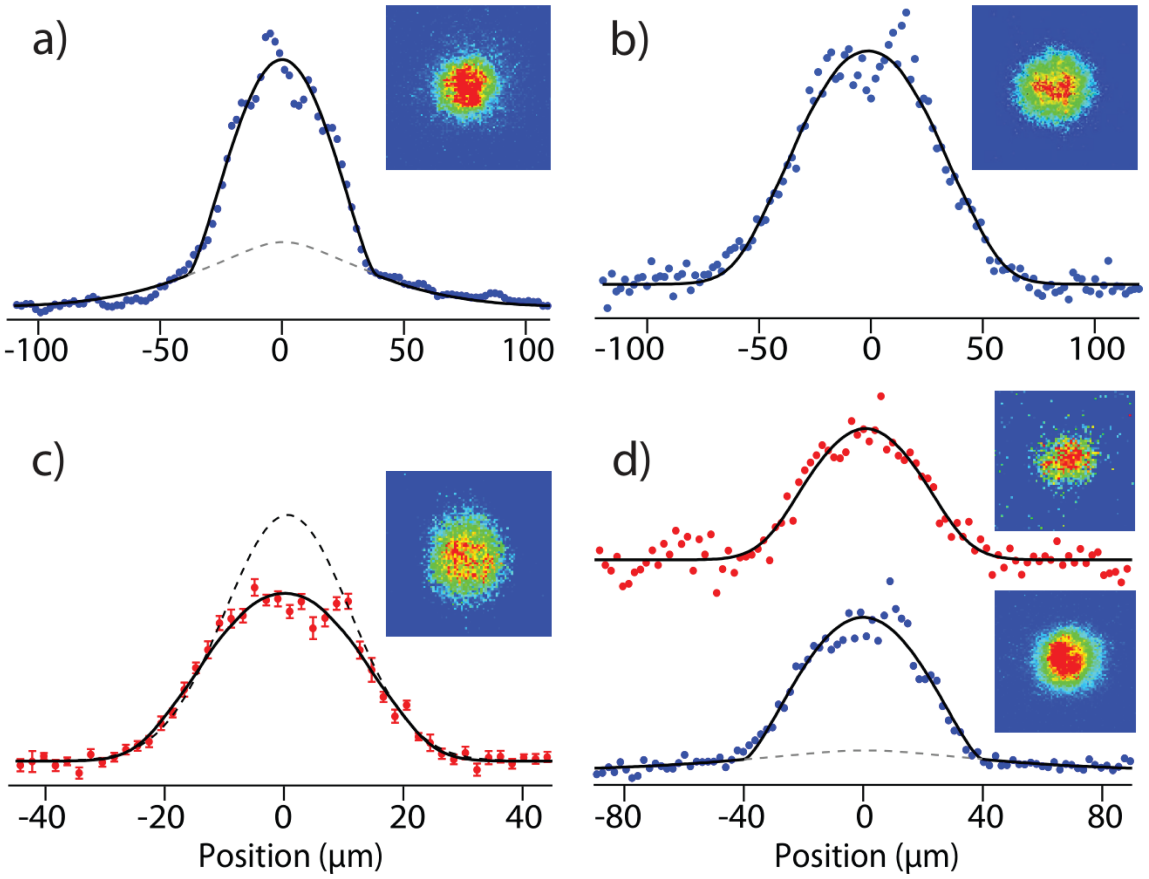

Figure 4.5: Measured momentum distributions in the $\hat{y}$ direction for atoms with nearly 0 momentum in the $\hat{x}$ direction for quantum degenerate gases created in our apparatus and false color absorption images of the corresponding gas (inset). (a) A BEC of ^{174}Yb atoms containing 2.5×10^5 atoms. The dashed line is a fit to the thermal wings of the momentum distribution demonstrating the increased concentration of atoms near the zero momentum center. (b) A DFG of an un-polarized ^{173}Yb gas with 1.7×10^4 atoms per spin state. (c) A DFG of 1.6×10^4 spin-polarized ^{6}Li atoms. The dashed curve is a fit to the thermal wings of the momentum distribution demonstrating the reduced concentration of atoms near the zero momentum center due to Pauli blocking. (d) Simultaneous degeneracy of ^{174}Yb and ^{6}Li gases with $2(3) \times 10^4$ lithium (ytterbium) atoms. This figure appears as Fig. 5 in a previous work [59].

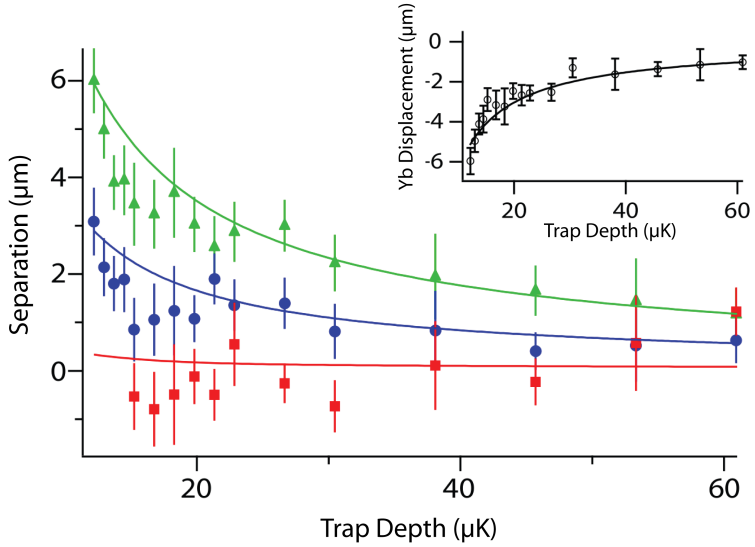

Figure 4.6: Separation between the lithium and ytterbium clouds as a function of trap depth for magnetic field gradients of 13G/cm (green data) 35G/cm (blue data) and 64G/cm (red data). (inset) Absolute displacement of the ytterbium gas as a function of trap depth. This image adapted from Fig. 2. in our previously published work [43].

frequency in the quantization axis. The bias field in our experiment is usually oriented vertically, therefore the effects of any magnetic gradient will be (anti) aligned with the effects of gravity.

The effect of gravity becomes pronounced in the ytterbium gas starting around trap depths of 40μK, resulting in displacements of 2μm, approximately the size of the ytterbium gas. This is especially important as the displacement effect of gravity on lithium is a factor of 65 times smaller. Continued evaporation can lead to the ytterbium and lithium gases becoming physically separated from one another. Contact can be re-established with a magnetic field gradient together with a large bias magnetic field (where the lithium $|1\rangle$ and $|2\rangle$ states have the same magnetic moments) which

forces lithium to be displaced an equal amount[59], and demonstrated in Figure 4.6. The two lithium spin components can also be separated by using a large magnetic field gradient at low magnetic fields, where the lithium $|1\rangle$ and $|2\rangle$ state have opposite magnetic moments.

Obtaining accurate trap frequencies is vital to analysis of our experiments. We can rely on the scaling between lithium, ytterbium, and metastable ytterbium trap frequencies according to their different masses and polarizabilities. However, the trap frequencies predicted by Eqn. 4.8 are not nearly accurate enough to rely on. Instead, we measure our trap frequencies directly. The two ways we have found to be most reliable are parametric heating and center of mass oscillations.

Parametric heating is achieved by mildly modulating the ODT trap depth at a given frequency. Should the modulation frequency be twice the oscillation frequency of atoms, they will be given some small additional energy on every oscillation. The added energy is visible as an increase in the temperature (size) of the resulting cloud, and reduced atomnumber due to increased evaporation, as shown in Figure 4.7. Higher order harmonics of the trapping frequency are also present in the resulting data.

The center of the atom-loss line-shape is systematically red-shifted from the center of the temperature (size) line-shapes. More energetic atoms experience a smaller effective trap frequency in a gaussian potential. This causes them to be quickly ejected from the trap for modulation frequencies slightly smaller than the trap frequency at the bottom of the gaussian.

Care must be taken when using parametric heating to ensure a constant oscillation number, as the energy increase is related to the number of oscillations. The resulting modulation time at the lowest frequencies is often comparable to other loss mechanisms, such as background gas collisions. In this case, an initial variable hold time before the oscillation begins is used to make the total loss due to these processes

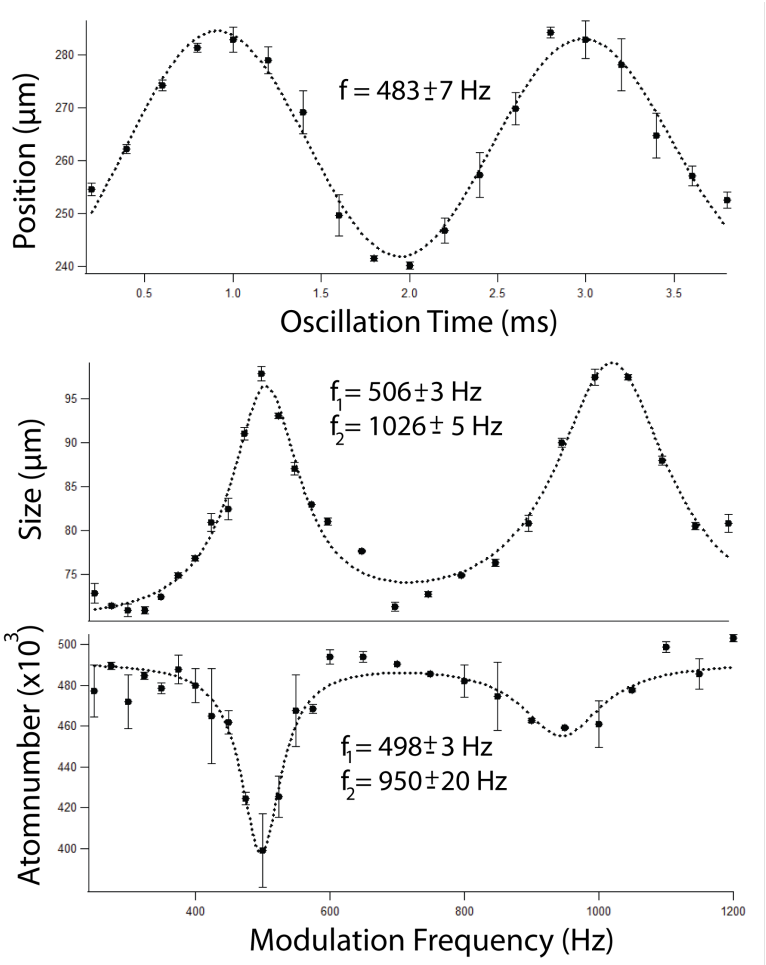

Figure 4.7: Ytterbium trap frequency measurements by parametric heating and center of mass oscillations.

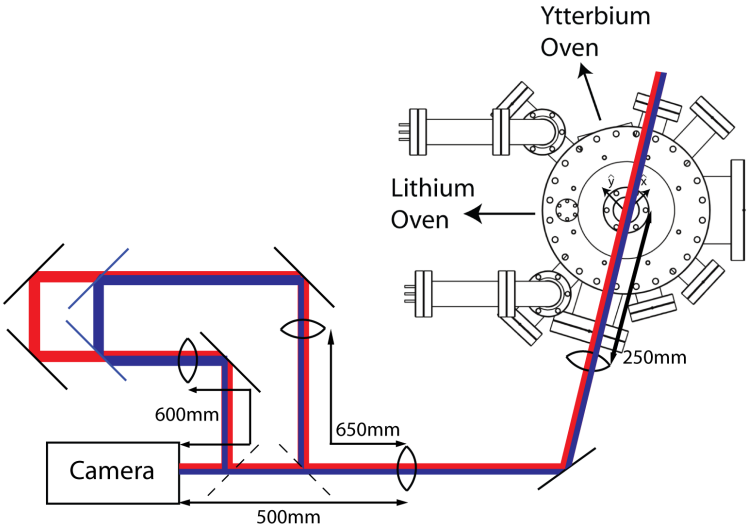

Figure 4.8: Schematic of the absorption imaging setup. Lithium (ytterbium) imaging beams represented by thick red (blue) lines. Removable kinetic mirrors represented by dashed lines. The dichroic mirrors which allow the lithium and ytterbium clouds to be imaged to different areas of the ODT are the blue lines. All lenses are 2 inches in diameter.

equal across all modulation frequencies.

Center of mass oscillations are achieved by displacing the entire atomic gas, after which the gas oscillates about its natural position at the trapping frequency. Our imaging system resolution is not sufficient for in situ images of this oscillation. However, we are sensitive to the in trap momentum oscillations which become much larger position oscillations after release and short expansion from the dipole trap, as shown in Figure 4.7. Inducing a center of mass oscillation is most easily achieved by evaporating low enough that ytterbium atoms become displaced due to gravity, followed by a sudden re-compression of the trap to the target depth.

4.4 Absorption Imaging

Number and temperature measurements of the atomic gases is achieved by absorption imaging. Absorption imaging is a destructive process, as each atom scatters hundreds of photons in the process. A pulse of resonant light is sent through the cloud of atoms, collected by a lens, and focused by a second lens onto a CCD camera as shown in Fig. 4.8.

Most imaging is conducted along an axis $\sim 7^o$ from the primary single beam ODT axis. CMOT imaging is accomplished with a 250mm collecting lens follwed by a 500mm focusing lens. Images of the ODT typically go through an extra 150mm→600mm telescope to magnify the image by an additional factor of 4. Switching between the two modes is done by a pair of mirrors on a removable kinetic mount. Dichroic mirrors in the second imaging path allow the lithium and ytterbium images to be steered to different parts of the CCD.

Imaging along the vertical axis is also available with a 150mm collecting lens and 300mm focusing lens. However, the imaging must share the vertical MOT optical path, and the required optics degrade MOT function considerably. As such, imaging along this axis is typically reserved for use as a temporary diagnostic.

The amount of light hitting the CCD is dictated by Beer's law

$$I = I_0 e^{-\sigma \int n dz} \tag{4.9}$$

where I_0 is the intensity of light before the atomic cloud, σ is the photon-atom interaction cross section, n is the density of the atomic cloud, and the integration direction $\hat{z}$ is performed along the photon wavevector $\hat{k}$. The 2-dimensional density profile $n(x, y)$ is then $-ln(I(x, y)/I_0(x, y))/\sigma$. The quantity $I(x, y)/I_0(x, y)$ can be extracted by taking three images: one with a light pulse interacting with the atomic cloud (A), one with an identical light pulse and no atomic cloud (B), and an image with no light pulse (C). I/I_0 is then simply $(A-C)/(B-C)$. An example absorption image is presented in Figure 4.9.

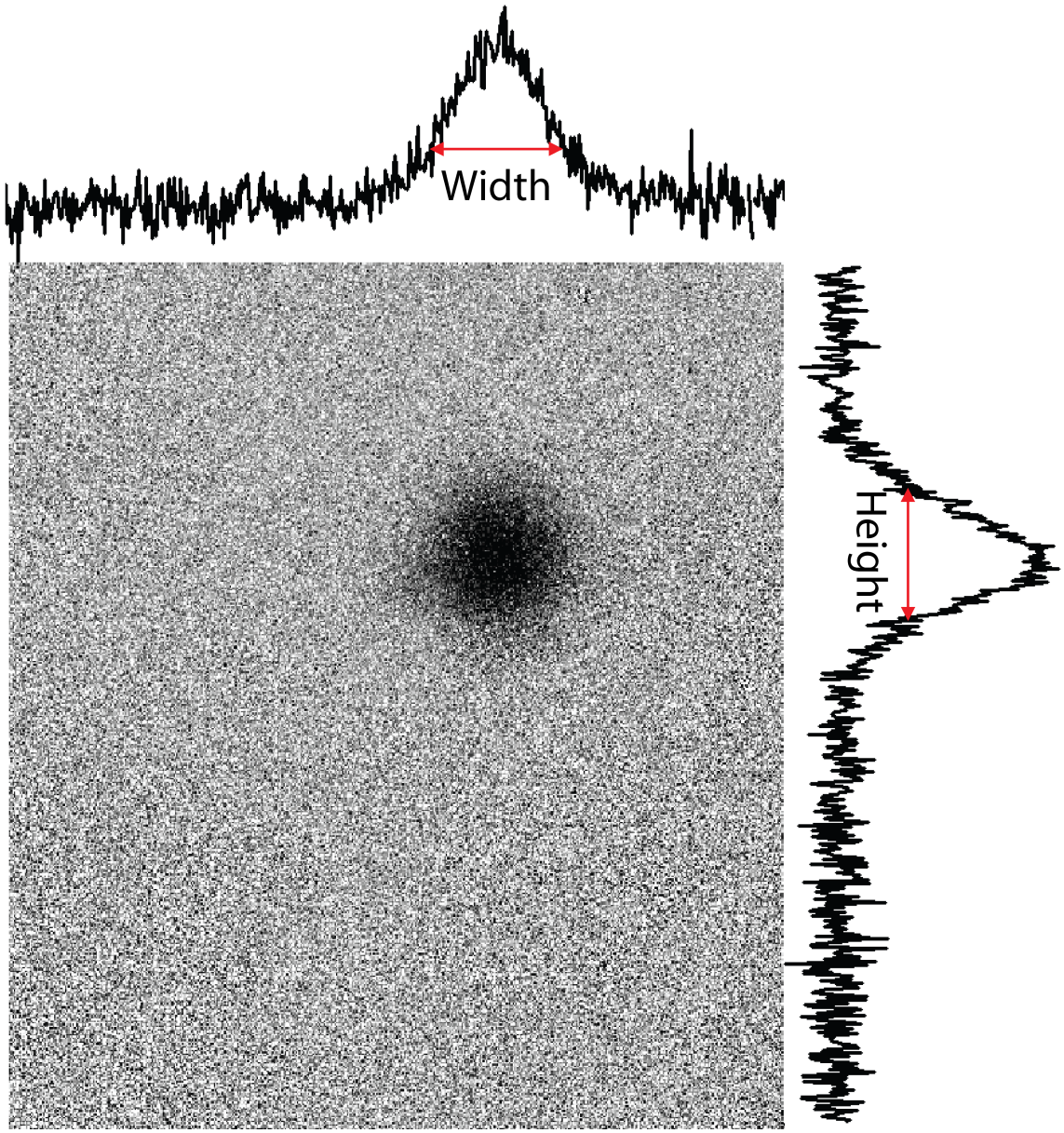

Figure 4.9: An absorption image of a ytterbium ODT after release from the dipole trap. The number density is related to the darkness of the pixels here. Above and to the side of the image are the 1-dimensional density profiles $n(x)$ and $n(y)$ obtained by summing the columns and rows of the image.

Obtaining atom numbers from the absorption images is done by summing across one dimension of the 2-dimensional density profile. For thermal gases, the subsequent one-dimensional density is fit to a gaussian profile, the area under which is proportional to the total atomnumber. Quantum degenerate gases do not have gaussian momentum distributions, and more careful analysis must be performed to extract accurate information.

The atomnumber is, of course, dependent on the atom-photon interaction strength σ. In the regime where $I/I_s \ll 1 + 4\delta^2/\Gamma^2$

$$\sigma = 3\lambda^2/2\pi \times \frac{1}{1 + 4\delta^2/\Gamma^2} \times C_g \tag{4.10}$$

where λ is the transition wavelength, Γ is the transition width, δ is the light detuning from resonance, and C_g is the Clebsch-Gordon coefficient for the laser polarization used in the transition. Typically, we operate at $\delta = 0$ to maximize photon scattering from our limited intensity beam. Off resonant imaging is required for accurate density profiles in situations where the atomic cloud is optically dense i.e. all photons are scattered along some optical paths.

The temperature of the atomic gases can also be extracted from the absorption images by relating the width and height of the clouds to the expansion time. We release the atomic gases from the ODT, which proceed to expand ballistically. After expansion time much greater than the inverse trapping frequency, the spatial density distribution will be an image of the trapped gases' momentum distribution. Usually data quality is not sufficient to achieve a reliable temperature measurement from a single image. The size of non-degenerate thermal clouds after release from the ODT follows the form

$$w(t) = w_0 \sqrt{1 + \frac{2k_B T}{m w_0^2} t^2} \tag{4.11}$$

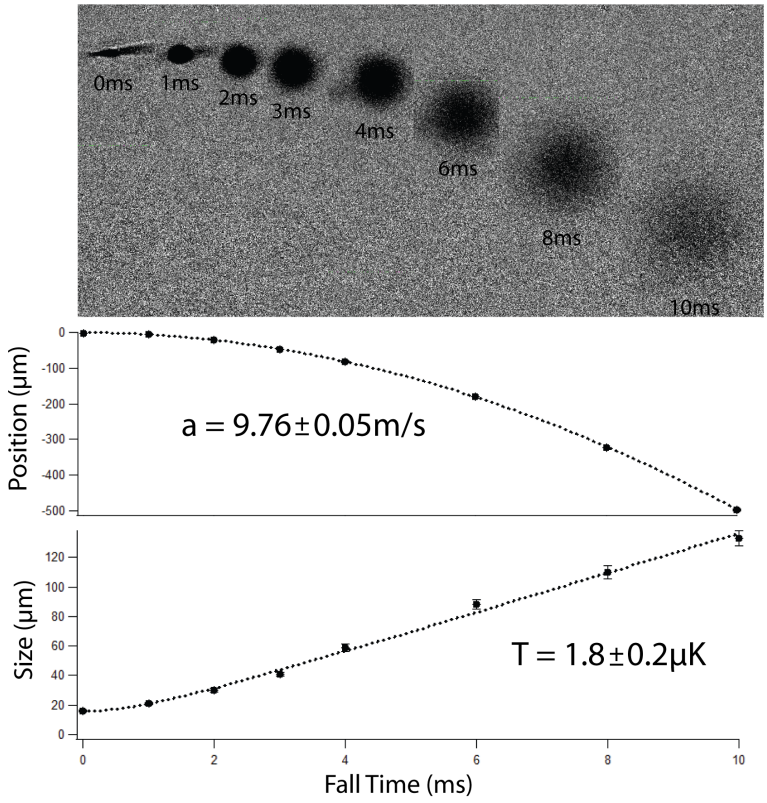

Figure 4.10: A gas of ytterbium atoms is allowed to freely expand and fall after release from the dipole trap. Equating the perceived acceleration with that of g provides a good measurement of the magnification of the system. Fitting the size of the cloud as it falls to Eq. 4.11 provides a measurement of the thermal cloud temperature.

where w_0 is the initial size, T is the temperature, m is the atomic mass, and k_B is Boltzmann's constant. Fitting the size of the cloud as a function of expansion time to this form extracts a reliable measure of the temperature as illustrated in Fig. 4.11.

Conversion between pixel coordinates and real-space coordinates is required to extract the real two-dimensional density profile. Each pixel in the CCD is 8μm on a side, and images a region of space that is $\frac{8}{M}\mu$m on a side, where M is the magnification of the imaging system. The magnification is a simple ratio of f_2/f_1 where f_1 is the focal length of the collecting lens and f_2 is the focal length of the focusing lens. However, wavelength shifts and minor lens misplacements can alter the magnification from the expected value.

The magnification of our system can be determined by dropping cold gases from the ODT, and allowing them to accelerate under the influence of gravity. We extract the magnification by fixing the observed acceleration to the value of g as shown in Fig. 4.11. Though we use achromatic lenses in our imaging system, the focal plane of the lenses shift by enough to alter the magnification of the lithium and ytterbium systems. Unfortunately, the gravity technique is only effective to fix the magnification of ytterbium atoms. Lithium atoms pose several problems. The magnetic moment of ground state lithium allows additional accelerations by magnetic field gradients, resulting in potentially erroneous measurements. Lithium is also extremely light and the gas disperses quite quickly. Imaging the lithium cloud beyond $\sim$ 1ms of expansion time is not feasible for the temperatures attainable in our system. During this time, the lithium cloud will only fall 5μm. Instead, we allow the lithium and ytterbium gases to thermalize for long periods of time. We then fix the lithium magnification to ensure that the lithium and ytterbium gases have the same extracted temperatures.

An additional method to determine the magnification involves placing a test pattern with known line spacings at the same distance from the collecting lens as the atoms (though clearly not in the same location). This technique works very well, however requires some unfortunate maneuvering given the density of optics 200mm

from the collecting lens.

Extension of the absorption imaging technique to image both atomic gases at once would seem simple; take two additional images, one with the second resonant light source and atoms, the other with just the second resonant light source. Unfortunately, our CCD camera system requires $\sim$ 300ms between subsequent shots. This is more than enough time for the system to evolve given the many photon recoils added to the first atomic gas. In the case where we do not wish to image the atoms in situ (the vast majority of the time), the scheme is wholly unworkable as the untrapped atoms have long since left the image area.

Instead, we use a scheme with four pictures: one in which both resonant light sources are on for the image with atoms (A), one with the light pulse for lithium atoms (B), one with the light pulse for ytterbium atoms (C), and the image with no light sources (D). Images of the lithium atoms are then obtained by performing $(A - C)/(B - D)$; similarly ytterbium images are $(A - B)/(C - D)$. The lithium and ytterbium lights take different paths to the camera system, allowing the co-located gases to be imaged to different parts of the CCD. An example dual-absorption image is shown in Fig. 4.12. The signal to noise in such dual-absorption images is approximately one-half that of the corresponding single-absorption images.

The light pulses must be kept short enough that momentum kicks from photon recoils cannot appreciably affect atom positions. Typical exposure times of 10–40μs are used in our experiment. The intensity must be kept well below the saturation intensity to ensure a linear scattering response. If this condition is not satisfied, spatial intensity variations must be accounted for in the subsequent absorption image. For these two reasons, total photon counts on the camera can be quite low. A camera with low background noise, large quantum efficiency, and large electron gain capabilities is essential in obtaining high quality images.

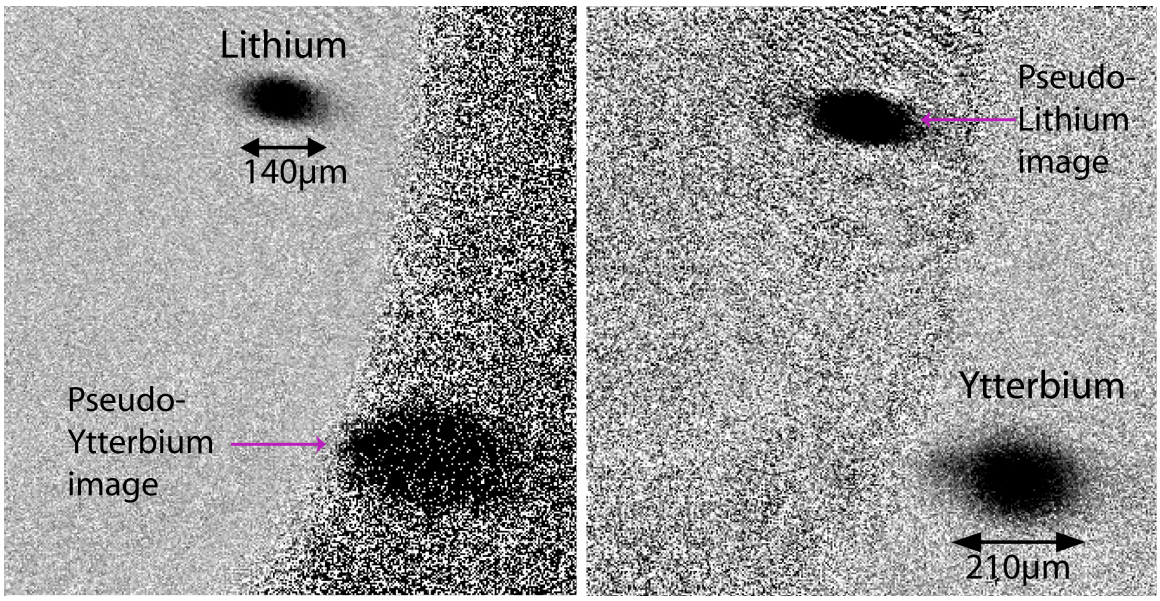

Figure 4.11: Dual absorption image of ytterbium and lithium atoms in the ODT. Clearly, should the two clouds be imaged to the same section of the camera, the resulting images would be ruined. The lithium light is blocked by a strategically placed card from hitting the camera where the ytterbium atoms are imaged, which mitigates the effects of the reduced signal to noise in dual-absorption imaging. This is the cause for the apparent large noise for half of the lithium image. The corresponding improvement in ytterbium image quality is also apparent.

We use a 1024X1024 CCD array camera (Andor Ixon-3^{EM}+) for our imaging duties. The sensor is cooled to -80^{o}C to minimize background counts. Electronic gain on the CCD photo-electrons of up to 300 are possible, although typical usage is 10-30. The CCD sensor is frontlit to maximize quantum efficiency, which is 93(63)% for the 671(399)nm transition. Cooled CCD sensors must have a protective film to prevent water condensing and freezing on the sensor. The protective film in our camera is optical quality glass with a broadband anti-reflection coating. The glass is wedge shaped to eliminate interference effects due to interior reflections in the glass, which can degrade image quality.

The resolution of our imaging system is almost entirely defined by the numerical aperture and placement of the collecting lens. We use a 2" 250mm lens which gives a numerical aperture (NA) of 0.101; the best resolution achievable is λ/NA, where λ is the wavelength of light: 6.6 and 3.9μm for lithium and ytterbium, respectively. The lens must be placed such that the focal plane is aligned with the atomic cloud to achieve this resolution. However, the focal shift between 671 and 399nm light, despite our use of an achromatic lens, is large enough to make this impossible. As such, we must choose to sacrifice some resolution for one or both of the species.

Ytterbium imaging is conducted at zero magnetic field, where both the 399nm and 556nm transitions have a Clebsch-Gordon coefficient of 1 for all polarizations for bosonic isotopes. The 399nm transition is the preferred imaging transition due to the larger saturation intensity and linewidth of the transition. The larger saturation intensity allows us to use more photons resulting in superior image quality. The large linewidth allows us to ignore Doppler broadening of the transition for gases below $\sim$ 500μK in temperature. Typical ytterbium imaging beams have 150–300μW of power in a $\sim$ 5mm^2 beam giving a saturation paramater of 0.1.

Lithium imaging is conducted in either the "high-field" or "zero-field" regime. The zero-field regime has a Clebsch-Gordon factor of 1/3, and is polarization and Zeeman substate independent. Imaging in the zero-field regime requires additional $F = 3/2$

resonant D2 light to repump atoms lost to this otherwise dark state. Because atoms spend some amount of time in the dark state, the zero-field imaging numbers are typically slight underestimates.

Lithium high-field imaging has a Clebsch-Gordon factor of 1/2 for light polarized parallel to the quantization axis. A single frequency beam is engineered to be resonant with the $|1\rangle$ D2 transition at 528G and the $|2\rangle$ D2 transition at 475G. These transitions are cycling and avoid the undercounting error present in zero-field imaging. High field imaging light also allows us to selectively remove $|1\rangle$ or $|2\rangle$ state lithium atoms from the ODT, leaving behind a spin-purified sample. Typical lithium imaging beams have 100μW of power in a $\sim 5\text{mm}^2$ beam giving a saturation parameter of 0.7.

Chapter 5
INTERACTIONS

The details of the microscopic interactions between atom pairs leads to wildly varying behavior in the bulk gas. In the ultracold regime, these interactions are often defined by a single parameter: the s-wave scattering length. Diverse system properties are already available with different scattering lengths. Condensates tend to self-destruct if the scattering length is negative[61], but are often stable for positive scattering lengths. Degenerate fermi gases can form molecular condensates at large positive scattering lengths [62], exhibit BCS-like superconductivity at large negative scattering lengths [63], and altogether different behavior in the so-called "cross-over" regime between these two extremes [64]. Multi-species experiments have observed phase separation of the gases in systems with particularly large scattering lengths [65].

Magnetic atoms and molecules also feature anisotropic dipole-dipole interactions. These interactions lead to even more diverse behaviors. Molecules can also have significant DC electric polarizabilities thus extending the possibilities for anisotropic interactions to two independent axes. This paves the way for many exciting experiments e.g. the 2-D lattice-spin models recently proposed [28].

5.1 Contact Interactions

Atom-atom interactions are almost exclusively electromagnetic. While the effects of other interactions (e.g. gravitational) can in principle be observed [66], their effects are extremely small and can be safely ignored in our experiment.

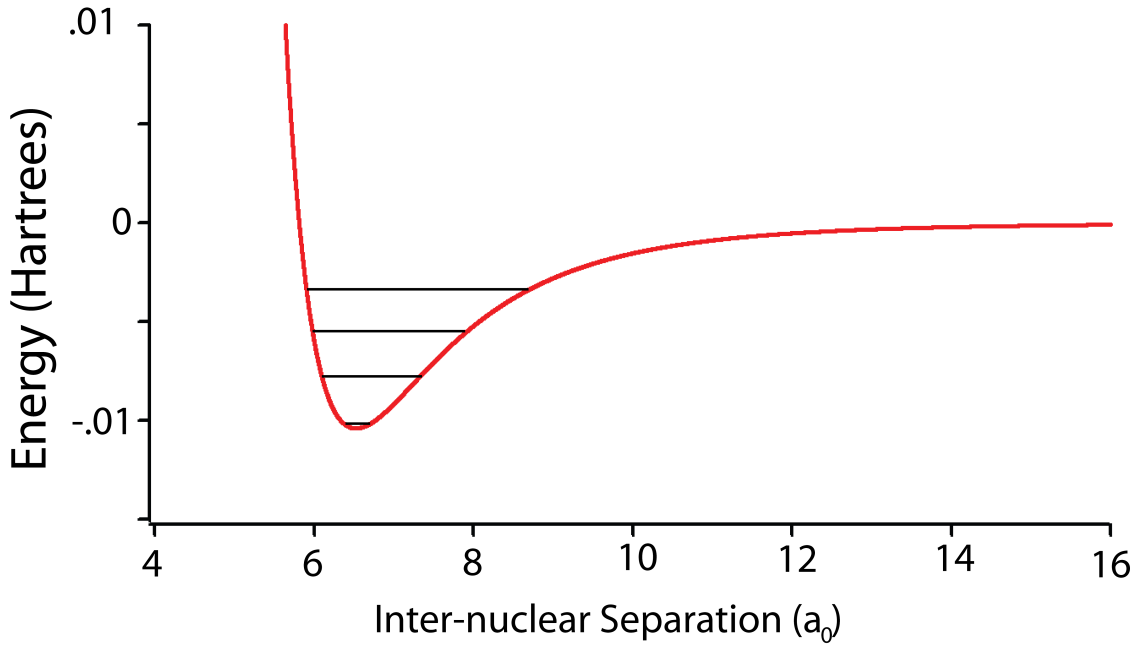

Figure 5.1: An approximation of the interaction potential between ground state lithium and ytterbium atoms. Black lines indicate the presence of bound states in this potential: LiYb molecules! The locations of the bound states in this plot are for illustration purposes only, and not accurate.

The electric and magnetic interactions we treat as a potential $U(r) = \sum -C_n/r^n$, where C_n characterizes the strength of the r^n interaction, and r is the inter-nuclear distance. The presence of an external electric or magnetic field makes these terms anisotropic; in this case C_n will be a function of the relative orientation of the atoms. The full potential also includes terms which account for the hard core repulsion due to the two electron clouds physically overlapping. The resulting potential often supports bound states (molecules!), as illustrated in Fig. 5.1.

The full interaction potential adds the angular-momentum pseudo-potential $L^2/2\mu r^2$ to the electro-magnetic potential. Here L is the angular momentum operator, μ is the reduced mass, and r the inter-nuclear distance. The long range potential is determined by this angular momentum term and the first term in the C_n/r^n expansion, typically the induced electric dipole-dipole term (C_6). The long range interaction is illustrated in Fig. 5.2.

Collisions which reach the strong repulsive core are termed contact interactions, and allow the atoms to exchange energy and (angular) momentum, as well as relax to lower lying bound states. Contact interactions are the microscopic processes behind the thermalization and inelastic decay processes we observe in the bulk gases. As shown in Fig. 5.2, contact interactions are strongly suppressed if the collision energy is less than the potential barrier created by the angular-momentum pseudo-potential. The barrier height is

$$U_{bar} = -C_n/\chi^n + \frac{L^2}{2\mu\chi^2} \tag{5.1}$$

with C_n the lowest non-zero term in the interaction, and χ the location at which the potential is maximized

$$\chi = \left(\frac{n\mu C_n}{L^2}\right)^{1/n-2} \tag{5.2}$$

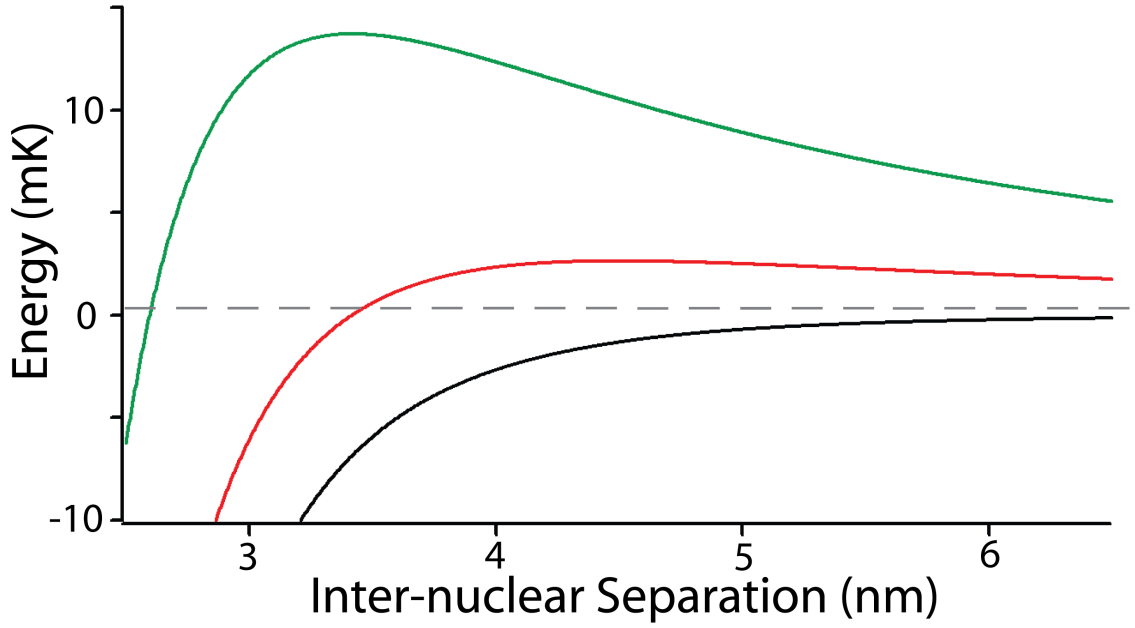

Figure 5.2: The long range interaction between lithium and ytterbium atoms in the $L = 0$ (black curve), $L = 1$ (red curve), and $L = 2$ (green curve) angular momentum channels. An isotropic interaction is assumed where $L^2 = l(l+1)$. The value of $C_6 =$ 1606a.u. used in these plots is derived from a calculation of the lithium ytterbium potential [67]. The gray dashed line indicates the approximate energy of a 400μK collision between a ytterbium atom and a lithium atom recently loaded into the ODT from the CMOT.

For an isotropic potential, we can write $L^2 = \hbar^2 l(l+1)$ where l is the eigenvalue of the L operator. The $l = 1$ "p-wave" barriers in the isotropic case are of particular interest, and listed in Table 5.1.

	Li			Yb			Yb*		
	C_6 a.u.	χ nm	U_{bar} mK	C_6 a.u.	χ nm	U_{bar} mK	C_6 a.u.	χ nm	U_{bar} mK
Li	1389	3.7	8.0	1606	4.5	2.7	2736	5.2	2.1
Yb	1606	4.5	2.7	1929	9.2	.043	–	–	–
Yb*	2736	5.2	2.1	–	–	–	7423	13	.021

Table 5.1: The leading term coefficients (atomic units) [68, 67, 69], and resulting p-wave barrier inter-nuclear distances and magnitudes for collisions in our system. The C_6 coefficients for Yb* interactions reported here are the maximum C_6 coefficients of many potentials which asymptote to the Yb*+X energy level. The proper averaging, which requires knowledge of the Yb* substate(s) involved in the collision, will result in a smaller typical C_6. The Yb+Yb* interaction strength is unknown at the time of publication .

Symmetry constraints must also be satisfied, making "d-wave" interactions the first relevant barrier for spin-polarized bosonic Yb+Yb and Yb*+Yb* interactions. The first relevant terms in these interactions are C_6/r^6 and the resulting barrier is $3^{3/2} \approx 5.2$ times larger than the p-wave barrier. Every p-wave (d-wave) barrier is much larger than the largest collision energies in our system. This allows us to consider only $l = 0$ "s-wave" collisions. In this case, the entire elastic collision process is determined by a single constant, the s-wave scattering length a which subsumes all details of the full potential.

Precise determination of the scattering length can be achieved by measuring the binding energies of the most weakly bound dimers via photo-association spectroscopy

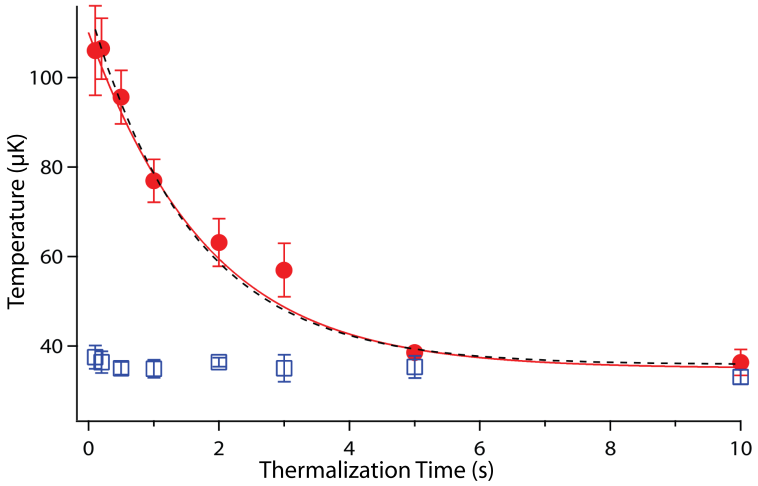

Figure 5.3: Lithium and ytterbium atoms thermalizing in a single beam dipole trap. The lithium gas (red data) is cooled by the presence of the cold ytterbium gas (blue data). The temperatures equilibrate with an exponential time constnat of 1.7 ± 0.2s (black dashed line).

[70]. Such experiments have been conducted to determine the scattering length between all ytterbium isotopes [71]: ^{174}Yb $+^{174}$Yb interactions have a $+5.55$nm scattering length.

Lacking spectroscopic data, one can determine the collision cross section between species in thermalization experiments as has been done for the Li-Yb interaction [72, 73]. Each collision transfers average energy $\propto k_b \Delta T \xi$, with ΔT the temperature difference and $\xi = 4m_{Li}m_{Yb}/(m_{Li} + m_{Yb})^2$ accounting for unequal mass collision partners [74]. Two particles will thermalize after an average of α/ξ collisions, with $\alpha = 2.7$ the average number of collisions for equal mass partners.

The thermalization rate between two unequal temperature gases is then

$$\gamma_{th} = \frac{\xi}{\alpha} \bar{n} \sigma \bar{v} \tag{5.3}$$

where $\bar{n}\sigma\bar{v}$ is the average collision rate. The s-wave collision cross section is $\sigma = \{0, 4, 8\}\pi a^2$, where a is the s-wave scattering length and 0 is taken for identical fermions, 8 for identical bosons, and 4 for distinguishable particles. $\bar{n}$ is the particle number overlap density $\int n_{Li} n_{Yb} d^3x/(N_{Li} + N_{Yb})$ with $n_{Li(Yb)}$ and $N_{Li(Yb)}$ the lithium (ytterbium) density and total atom number, respectively. $\bar{v}$ is the average collision velocity $\sqrt{\frac{8k_B}{\pi}\left(\frac{T_{Li}}{m_{Li}} + \frac{T_{Yb}}{m_{Yb}}\right)}$ with $T_{Li(Yb)}$ and $m_{Li(Yb)}$ the lithium (ytterbium) temperature and mass, respectively.

Thermalization data between lithium and ytterbium shortly after they are loaded into the ODT is presented in Fig. 5.3. An exponential fit to the data gives a thermalization time constant of 1.7 ± 0.2s, and subsequent scattering length of $|a|_{Li-Yb} = 0.69 \pm 0.15$nm given the experimental parameters [72]. A small energy dependent term in the collision cross section must be included by expanding σ to fourth order in the collision momentum $\hbar k$: $\sigma = \frac{4\pi a^2}{(1-k^2 r_e a/2)^2 + k^2 a^2}$ with r_e the effective range of the interaction satisfying $\cot\phi = -1/\mathrm{ka} + \mathrm{r_e k}/2$, ϕ being the phase shift of the collision. A similar experiment in the Kyoto University Li-Yb group gives $|a|_{Li-Yb} = 1.0 \pm 0.2$nm [73]. As the thermalization rate scales with a^2, this method cannot determine the sign of the scattering length, only its magnitude.

The ^{6}Li $+^6$Li scattering length is a more complicated topic. For identical substates, it is simply zero, as these collisions are excluded by symmetry. For non-identical substates, the scattering length is strongly dependent on the magnetic field, and is the topic of Section 5.2.

5.1.1 Inelastic Collisions

Collisions allow atoms to relax to states with lower energy, a process we call inelastic loss. Except in special circumstances (see Sec. 5.2), the relaxation energy is much greater than the trapping potential, and all collision partners are ejected from the trap. Inelastic processes are categorized by the number of atoms involved in the collision: two-body, three-body, etc collisions.

Two-body collisions involve relaxations of single-atom degrees of freedom, such as an atom in an electronically excited state. These are the types of inelastic processes which make gases of lithium atoms in the $F = 3/2$ manifold unstable, as they are able to relax to the $F = 1/2$ manifold and release $h \times 228$MHz (11.4mK) of energy.

The two-body collision process can be described by using a complex scattering length $a = \alpha - i\beta$ with α the familiar s-wave scattering length and $\beta = \mu K_2/4\pi\hbar$. Here, μ is the reduced mass and K_2 is the bulk gas loss constant defined by the relation $\dot{n_1} = \dot{n_2} = -K_2 n_1 n_2$ where n_1 and n_2 are the local particle densities of the two gases. Crucially, K_2 depends on temperature and any other quantity which may affect the collision dynamics.

Three-body collisions involve relaxations of atom-pair degrees of freedom, such as two atoms relaxing to a bound molecular state. The third collision partner is required in order to satisfy the momentum and energy conservation laws. Three-body loss processes are also modelled in the bulk, with the defining equation $\dot{n_1} = \dot{n_2} = \dot{n_3} = -K_3 n_1 n_2 n_3$. Three-body collisions are often the limiting factor in atomic physics experiments. Consideration of four and larger body collisions is typically unnecessary.

5.2 Feshbach Resonances

One of the great triumphs of ultracold atomic experiments is the ability to tune the scattering length of the system quickly and easily. This is achieved by the mechanism known as a magnetic Feshbach Resonance [16]. Resonances in cold atomic collisions have been described in detail e.g. [75].

The presence of a nearby bound state in the interaction potential strongly affects the collision properties of a system. Tuning the collision energy into resonance with such a bound state causes the scattering length to diverge. Magnetic Feshbach

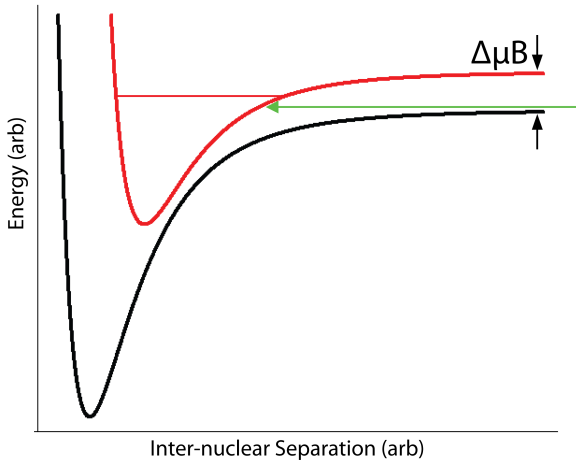

Figure 5.4: Spin singlet (black curve) and spin triplet (red curve) interaction potentials of a synthetic system. Atoms colliding in the spin singlet channel (green arrow) have their scattering dynamics perturbed by the nearby bound state of the spin triplet channel. The detuning between collision energy and bound state energy can be tuned with a magnetic field (B) if the states have different magnetic moments ($\Delta\mu$), resulting in a magnetic Feshbach resonance.

resonances are a common experimental realization of this idea, in which two interaction potentials with different magnetic moment are tuned against one another, as illustrated in Fig. 5.4.

The detuning between the entrance collision channel and the bound state allows one to precisely tune the scattering length. In magnetic Feshbach resonances, the scattering length response is parameterized as

$$a(B) = a_{bg}\left(1 - \frac{\Delta}{B - B_0}\right) \tag{5.4}$$

where a_{bg} is the scattering length in the absence of a scattering resonance, Δ is the width of the resonance, and B_0 is the location of the resonance.

The strength of the resonance, defined as $\Gamma = \Delta\delta\mu$ with $\delta\mu$ the differential magnetic moment, is determined by the coupling between the scattering and bound states. The hyperfine interaction, which is not diagonal in the total spin of the two collision partners, often provides strong coupling between scattering and bound states.

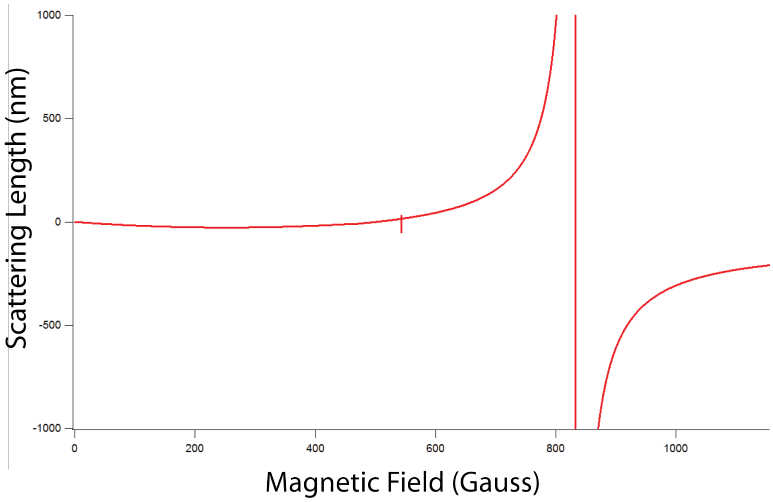

Figure 5.5: Scattering length between $|1\rangle$ and $|2\rangle$ lithium as a function of magnetic field. The Feshbach resonance at 832G features prominently. The much weaker resonance at 543G is also visible.

The scattering length between the $|1\rangle$ and $|2\rangle$ states of lithium is dominated by a Feshbach resonance at 832G. This resonance is parameterized with width -300G and $a_{bg} = -2160\mathrm{a}_0$ [76, 77]; the scattering length is plotted in Fig. 5.5. The background scattering length only parameterizes the Feshbach resonance, and other dynamics determine the scattering length far from resonance; notably, the scattering length goes to 0 at 0 magnetic field. An additional weak resonance at 543G, as well as a p-wave resonance at 185G are also of interest in some applications.

Feshbach resonances in systems with two body loss processes have a reduced tuning of the scattering length. With $a = \alpha - i\beta$, the scattering length in the presence of a Feshbach resonance becomes

$$\begin{aligned} \alpha(B) &= \alpha_{bg}\left(1 - \frac{\Delta(B - B_0)}{(B - B_0)^2 + \gamma^2/4}\right) \\ \beta(B) &= \frac{2\alpha_{bg}\Delta\gamma}{4(B - B_0)^2 + \gamma^2} \end{aligned} \tag{5.5}$$

with α_{bg} the background scattering length, Δ the width of the resonance, B_0 the center of the resonance, and $\gamma = \hbar\Gamma/\delta\mu$ with Γ the inelastic decay rate of the bound state, and $\delta\mu$ the difference in magnetic moment of the scattering and bound states.

5.2.1 Magneto-Association

Adiabatic tuning of the bound state from above the collision energy to below the collision energy allows resonant formation of so called "Feshbach molecules". The presence of the resonance dresses the bound state, altering its properties. Feshbach molecules are extremely weakly bound and large, with binding energy $E_b = \hbar^2/2\mu a^2$ and bond length a, where μ is the reduced mass and a is the scattering length. Spontaneous relaxation is inhibited due to poor wave-function overlap with lower lying states because of the large size mismatch. Thus, Feshbach molecules are fairly stable in isolation. Collisions are another avenue of relaxation and tend to spoil the Feshbach molecule stability if not mitigated.

The efficiency of Feshbach molecule creation can be comparatively large at 10-15% [78] for cold gases with good phase-space overlap. Once created, the molecules must be quickly transferred to protected states (e.g. the ground state via STIRAP [79]) to prevent collisional relaxations. The decent efficiency makes magneto-association of cold atom gases an excellent choice for creation of ultracold molecular gases.

5.2.2 Lithium-Ytterbium Feshbach Resonances

There is only one interaction potential for the lithium-ytterbium ground state system. However, weak Feshbach resonances can still occur. Bound states of the lithium-ytterbium potential with a different magnetic moment than the scattering state can be tuned into resonance with a magnetic field. The coupling mechanism relies on the nuclear magnetic moment of ytterbium interacting with the electronic spin of lithium. The coupling is much weaker than the hyperfine interaction; Feshbach resonances between lithium and fermionic ytterbium are expected to have widths of $\sim$ 1mG [80].

The approximate location of the nearest bound state and its calculated magnetic moment indicate a lithium-ytterbium resonance at $\sim$ 1000G fields. The bosonic isotopes of ytterbium have a nuclear spin of 0, and must rely on even weaker couplings; predicted widths are $\sim 1\mu$G at similar bias fields [80].

Precise knowledge of the bound state energy allows one to accurately predict where these ultra-narrow Feshbach resonances occur. Measurements of the lithium-ytterbium s-wave scattering length indicate the Feshbach resonance to occur near 960G or 1600G, dependent on the sign of the scattering length [80]. Initial attempts to detect a Feshbach resonance between ^{173}Yb and ^{6}Li near these fields have not produced results. Future experiments with more accurate knowledge of the interaction potential and therefore theoretical resonance locations are planned.

5.2.3 Lithium-$^3P_2$ Ytterbium Feshbach Resonances

Feshbach resonances between lithium and metastable ($^3P_2$) ytterbium offer another avenue for tunable interactions. The fermionic isotopes of ytterbium should feature strong Feshbach resonances with lithium which feature standard hyperfine coupling.

The bosonic isotopes of ytterbium feature an anisotropic coupling mechanism in which collisions in one Zeeman substate couple to a bound state of another Zeeman substate [81, 82]. These types of Feshbach resonances couple the entrance channel to bound states with angular momentum such that $\Delta l = \pm 2, \pm 4, ...$ Here, Δl is the difference in angular momentum associated with atomic motion about the system's center of mass. Such resonances have been observed in the Yb-Yb* system [83].

Chapter 6

INTERACTIONS IN THE ULTRACOLD LITHIUM - METASTABLE YTTERBIUM SYSTEM

We have observed strong magnetic-field dependent inelastic losses in a mixture of metastable $^3P_2$ ytterbium and ground state ^{6}Li . Together with theoretical work from our collaborators [84], our observations can be linked to anisotropy induced interspecies Feshbach resonances.

Collisions between lithium and metastable $^3P_2$ ytterbium can result in inelastic loss processes in which the ytterbium atom relaxes to lower energy Zeeman sublevels in the $^3P_2$ level, or to the $^3P_1$ and $^3P_0$ levels. A Feshbach resonance will influence these loss rates as described in Eqn. 5.5. We look for evidence of Feshbach resonances between spin purified substates of ^{6}Li and $^3P_2$ ^{174}Yb by measuring the interspecies inelastic loss rate constant K_2' as a function of magnetic field. The full experimental time sequence is detailed in Fig. 6.1. The results reported in this section have been published previously in two papers [84, 43].

6.1 Preparation of the Lithium-Ytterbium System

We sequentially load and compress ^{174}Yb and ^{6}Li MOTs into a single beam ODT. The ytterbium MOT is loaded for 20s, followed by a brief 1s lithium MOT load designed to maximize ytterbium atom number while maintaining reasonable lithium atom number. We obtain gases of 1.5 million (50 thousand) ground state ytterbium (50/50 mixture of $|1\rangle$ and $|2\rangle$ lithium) atoms.

After 4s of forced evaporation using an exponential ramp with time constant of

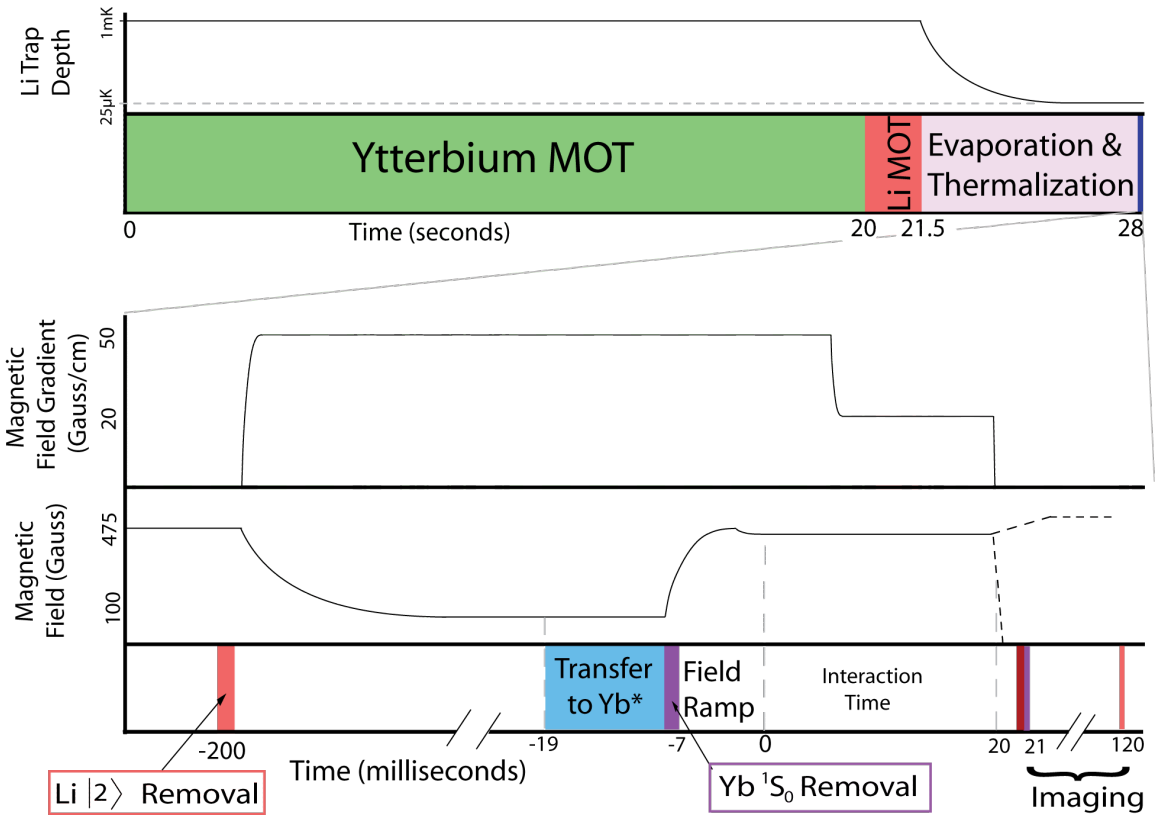

Figure 6.1: Time sequence of events for the Li-Yb* interactions experiment. The colored bars indicate important lasers used in that section: Yb ${}^1S_0 \rightarrow {}^3P_1$ (green), Li D2 (pale red), Yb ${}^1S_0 \rightarrow {}^3D_2$ (light blue), Yb ${}^1S_0 \rightarrow {}^1P_1$ (violet), and Yb ${}^3P_2 \rightarrow {}^3S_1$ (dark red). The field ramp time-step is variable length, dependent on the final target field. Here, the ramp time of 7ms is for the largest final fields. The interaction time varies from 0ms to 20ms. The magnetic field is either turned to 0 for Yb imaging, or ramped to 528G for lithium imaging. The Yb/Yb* removal lasers used when imaging lithium are not pictured for clarity.

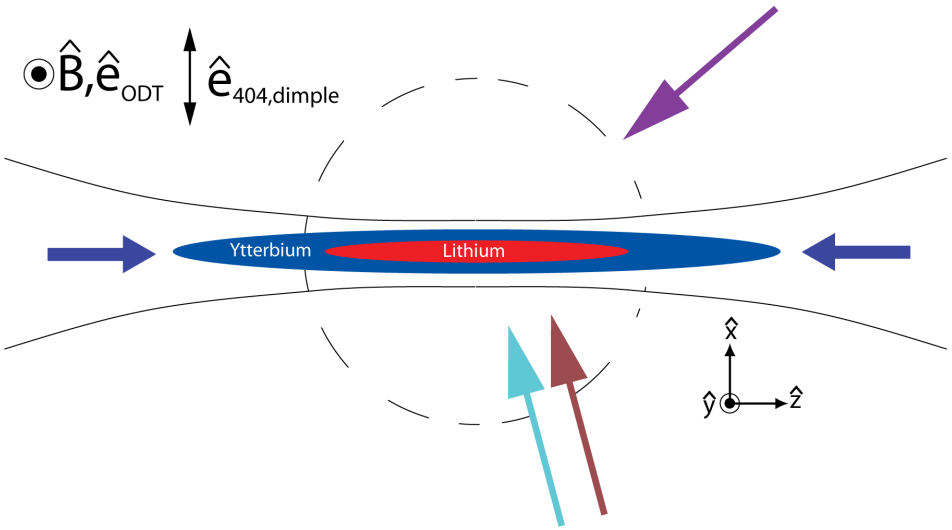

Figure 6.2: Schematic diagram of the lasers used in transferring ytterbium atoms to and from the metastable state as viewed from above. Ytterbium (blue ellipse) and lithium (red ellipse) are trapped in the horizontally aligned ODT (black curves) with the optional vertically aligned dimple trip (dashed black curve). Transfer to the Yb* state is achieved by 404nm light (blue arrows) incident on the atoms aligned along the ODT axis. Remaining ground state atoms are removed by a resonant pulse of 399nm light (violet arrow). Transfer back to the ground state is achieved by 770nm light (brown arrow) and optional 649nm light (teal arrow), where they can be imaged or removed by the 399nm light.

2.5s, and a 2s thermalization time, we obtain gases of $500(50)\times10^3$ ytterbium (lithium) atoms at 1.1μK. A brief (100μs) pulse of resonant light at high magnetic field removes the $|2\rangle$ state lithium atoms, leaving a spin purified sample of 25×10^3 $|1\rangle$ lithium atoms. The trap frequencies at this stage are $\omega_x = 2\pi\times513(4210)$Hz, $\omega_y = 2\pi\times508(4170)$Hz, and $\omega_z = 2\pi\times5.41(44.4)$Hz for ground state ytterbium (lithium) atoms.

6.2 Transfer to the Metastable $^3P_2$ State

Transfer of the ytterbium atoms to the $^3P_2$ metastable state is achieved via the intermediate $^3D_2$ state. The $^1S_0 \rightarrow ^3D_2$ electric quadrupole transition corresponds to

404nm light. The excitation laser beam has 1mW of power and is aligned along the axis of the dipole trapping beam with a waist of $\sim 30\mu$m, to maximize the beam intensity and spatial overlap with the ytterbium atoms (see Fig. 6.2). The bias magnetic field is perpendicular to the ODT axis; thus we are allowed to excite the $m_J = \pm 1, \pm 2$ sublevels of the $^3D_2$ state (see Sec 4.3).

A 10ms excitation beam exposure time, controlled by a shutter, is used to transfer the ytterbium atoms to the $^3P_2$ state. Our beam intensity ($5 \times 10^5 \mathrm{W/m^2}$), ytterbium quadrupole polarizability ($0.5a_0^2$[85]), and the beams' overlap with the correct vector spherical harmonic (0.228) give an expected $^1S_0 \rightarrow ^3D_2$ excitation rate of 5.5kHz. However, we cannot reduce the excitation time to the expected 2ms total transfer time as we are limited by $6-9$ms noise on the cavity lock used to keep the 404nm laser in resonance with the transition. Exposure times smaller than this noise timescale result in drastic fluctuations in the number of atoms transferred to the $^3P_2$ state. Unfortunately, the speed of the transfer process is a primary limit on the data quality; the high leverage data where inelastic losses are largest is unavailable for us to examine.

We use a single beam ODT in this experiment, as the increased density of an XODT causes the loss dynamics to become much faster than the transfer rate. The XODT also must use perpendicular beam polarizations to achieve long lifetimes necessary for efficient evaporation; the two beams would have very different strengths for the different Zeeman sublevels of the $^3P_2$ state. This effect may make the spin purification scheme we use less effective or impossible.

We use a 100G bias field during the transfer process, which splits the $^3D_2$ Zeeman sublevels by $h \times 163$MHz. The bias is chosen as a compromise between inelastic loss rates (lower at small magnetic field) and time spent ramping the electromagnets to the target magnetic field. Transfers using magnetic fields above ~ 250G are not feasible due to losses during the transfer process.

Transfer is completed via the $^3D_2, m_J = -2$ sublevel, which decays to the $m_J = -1$ and -2 sublevels of the $^3P_2$ state with 1/3 and 2/3 probability, respectively. In the

absence of lithium, up to 150×10^3 Yb* atoms in a spin mixture of $m_J = -1$ and -2 substates are trapped after the 10ms transfer process. In the presence of lithium, we achieve up to $75(15) \times 10^3$ spin-mixture Yb* (spin-pure lithium) atoms.

Each ytterbium atom absorbs 8.3 404nm photons on average during the transfer process. The transits through the ${}^1S_0 \rightarrow {}^3D_2 \rightarrow {}^3P_1 \rightarrow {}^1S_0$ cycle deposit $\approx 1.35\mu$K of average energy into each atom ending in the ${}^3P_2$ state. We should expect our Yb* gas to have risen significantly in temperature to 2.4μK. In fact, we observe a rise in temperature from $1.1(1.1)\mu$K to $1.7(1.5)\mu$K for the Yb*(Li) atoms. The discrepancy is explained by thermalization with the bath of ground state Yb atoms which remain at low temperatures, and that the trapped atoms are strongly biased to be those atoms which happened to make the transit fewer times.

In addition to the heating effect, a momentum kick is experienced, which adds 0.9mm/s per photon of velocity to the atoms. After 8.3 absorptions, center of mass sloshing and breathing modes in the trap with magnitude $v/\omega_z \approx 220\mu$m are excited. This results in strongly time dependent spatial overlap with the lithium cloud, and a difficult analysis of the resulting atom-loss data. We eliminate this potentially disastrous effect by using a balanced excitation scheme in which the atoms are equally driven by resonant beams from both sides of the trap.

A weak dipole trap aligned along the vertical axis is used in many data sets to further mitigate the sloshing and breathing mode effects. The weak trap has a radial trapping frequency $\omega = 2\pi \times 500(44)$Hz for Li(Yb*) atoms which supplements the weak axial trap and also improves spatial overlap between the lithium and metastable ytterbium gases. This trap is derived from a 1070nm laser source. The two-photon scattering process described for XODTs is suppressed here because the laser polarizations are perpendicular, and the broadband 1064nm source has very weak intensity at 1070nm to satisfy the stringent two-photon resonance condition.

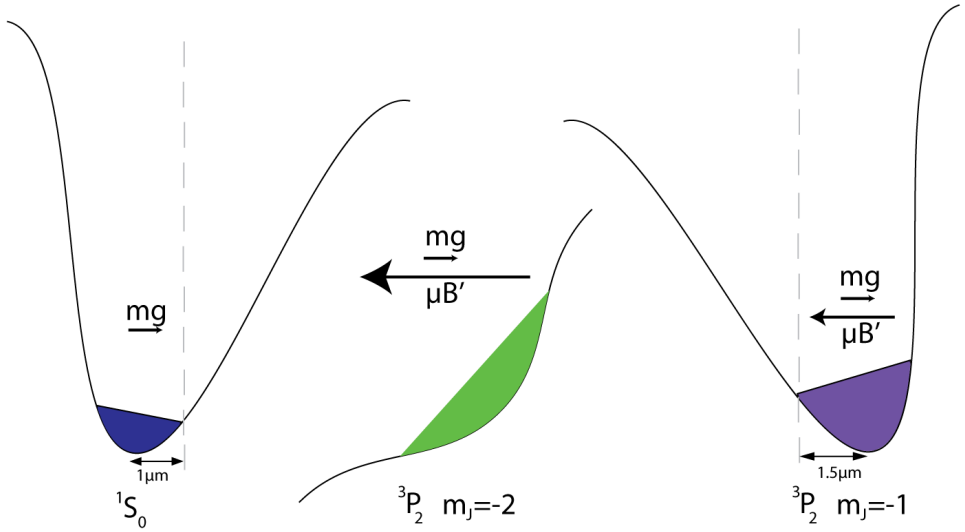

Figure 6.3: Diagram of the Yb* spin polarization scheme. A magnetic field gradient tilts the trap for the magnetic $^3P_2$ state atoms, while ground state $^1S_0$ atoms are unaffected. The tilt combined with the much weaker trap for $m_J = -2$ atoms causes them to be spilled from the trap while $m_J = -1$ atoms are minimally affected. The arrows illustrate the directions and relative magnitudes of the magnetic gradient and gravitational forces for the different substates of ytterbium. The center of mass displacement from trap center (dashed lines) during the excitation process is also noted for the trapped substates.

6.3 Spin Purification of Metastable Ytterbium

Each Zeeman sub-level of ytterbium will have different resonance locations with lithium as the difference in magnetic moment of the free and bound states will be different. This makes pure spin-states of metastable ytterbium an important prerequisite for accurate understanding of the resulting data.

Our spin purification scheme relies on spilling the $m_J = -2$ atoms from the trap as illustrated in Fig 6.3. This is achieved by setting the electric field of the dipole trap to be parallel to the bias magnetic field, resulting in a trap that is 1/5 the strength

for $m_J = -2$ as for $m_J = -1$ (and ground) state atoms. A magnetic field gradient of 50G/cm produces 5(2.5)mg of force on the $m_J = -2(-1)$ atoms, where m is the mass of ytterbium and g is the acceleration of gravity. We choose the force to be in the opposite direction of gravity for these sublevels of Yb*. The net 4mg of force, together with the reduced trap depth, causes the $m_J = -2$ atoms to be wholly untrapped. The net 1.5mg force on the $m_J = -1$ atoms results in a fairly mild 1.5μm shift in the cloud center (2.5μm from the ground state Yb cloud center). The magnetic field gradient's effect on lithium is a factor of $\frac{\mu_{Li}/m_{Li}\omega_{Li}^2}{\mu_{Yb*}/m_{Yb*}\omega_{Yb*}^2} \approx 0.29$ weaker than the effect on Yb* in the $m_J = -1$ state, resulting in a 0.3μm shift in the cloud center.

Adapting the scheme to purify the $m_J = -1$ state by spilling is not possible using a magnetic gradient with a 1064nm ODT, as the maximum difference in polarizability exactly cancels the magnetic moment difference; the atoms would spill at the same time. A pure state of $m_J = 0$ atoms can be obtained by exciting to the $m_J = -1$ sublevel of the intermediate $^3D_2$ state, which can decay to the $m_J = 0, -1, -2$ substates. Spilling both the $m_J = -1$ and -2 with a magnetic gradient leaves a pure sample of $m_J = 0$ atoms. In these experiments, we choose to spin-purify to the $m_J = -1$ substate.

Once the spin purified sample is obtained, arbitrary spin-compositions can be created using coherent RF transitions. The bare RF transition frequency between neighbouring levels is 2.1MHz/G. However, the transition frequency is also modified by the differential AC stark shift due to the ODT, which spectroscopically resolves the transitions. The shift is $-17(+11)$kHz per microkelvin of trap depth for $m_J = -1 \rightarrow m_J = -2(0)$ transitions. We are able to transfer the spin purified $m_J = -1$ atoms to the $m_J = 0, -2$ states with a 300μs resonant RF pulse. We note that the $m_J = -2$ atoms experience a very different trap from the $m_J = -1$ atoms, and transfer to this substate results in excitation of strong center-of-mass breathing and sloshing modes, greatly reduced densities, and strong evaporation processes. For these reasons, transfer to the $m_J = -2$ level is not feasible for this experiment.

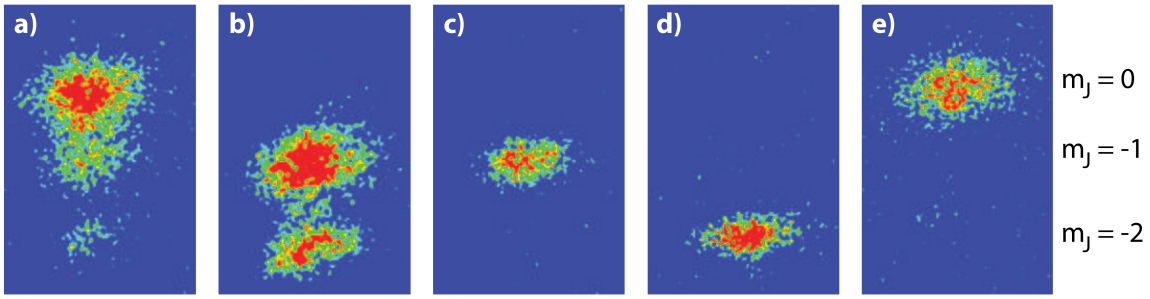

Figure 6.4: Stern Gerlach absorption images of the Yb* atoms in several spin mixtures. The false color indicates atomic density, while position indicates the spin state. (a) A mixture of $m_J = 0, -1$ and -2 atoms obtained by transferring via the ${}^3D_2$ $m_J = -1$ state. (b) A mixture of $m_J = -1$ and -2 atoms obtained by transferring via the ${}^3D_2$ $m_J = -2$ state. (c) Spin-purified cloud of $m_J = -1$ atoms using the magnetic field gradient spill technique. (d-e) RF transfer to the $m_J = -2$ and 0 states after obtaining a spin-purified $m_J = -1$ cloud.

Spin purity is ascertained through Stern-Gerlach imaging of the resulting sample as shown in Fig. 6.4. The trap is turned off and the magnetic gradient is ramped to ~ 150G/cm. After a short expansion time of 1–2ms, the different spin states spatially separate under the differential force of the magnetic gradient ($\sim 80\mu$m between spinstates for a 1.5ms expansion time).

6.4 Imaging

Imaging of metastable ytterbium is achieved by transferring the atoms back to the ground state, and imaging on the standard ${}^1P_1$ transition at zero magnetic field. Transfer to the ground state is accomplished by exciting the metastable ytterbium atoms to the ${}^3S_1$ state with a pulse of resonant 770nm light. The ${}^3S_1$ state decays to the ${}^3P$ manifold very quickly (13ns). Atoms returning to the ${}^3P_2$ state are quickly repumped with resonant light. Atoms entering the ${}^3P_0$ state can be repumped with a light source resonant with the ${}^3P_0 \rightarrow {}^3S_1$ transition at 649nm. Atoms entering the

$^3P_1$ state decay to the ground state after 0.9μs, where they can be imaged using the standard $^1P_1$ transition. A 100μs, 6mW, 1mm waist-size pulse is sufficient to transfer all atoms out of the $^3P_2$ state. Typically, the experiment is run without the $^3P_0 \rightarrow ^3S_1$ repumping beam; the experimentally calibrated fraction of un-imaged atoms in this case is 0.24. Absorption imaging is performed immediately after to minimize the impact of the photon recoils imparted in the transfer process.

We perform high field imaging of lithium, which requires a $\sim$ 100ms ramp to the required 528G magnetic field. We eliminate interactions during this ramp by first removing all ytterbium atoms from the trap with a 1ms pulse of resonant 770nm and 399nm light. $^3P_0$ atoms are untrapped at 1064nm and do not affect the lithium atoms.

6.5 Measuring the Interactions

After transfer to the metastable state, we reduce the magnetic field gradient to 20G/cm which exactly cancels the effects of gravity for Yb* in the $m_J = -1$ substate. Coincident with this, we ramp the magnetic field from the transfer field of 100G to the variable target field. A Hall probe is used to measure the current in the Helmholtz coils generating the magnetic field; accurate calibration of magnetic fields is obtained using well known lithium $|1\rangle \rightarrow |2\rangle$ RF transition frequency curves.

Magnetic field ramp speed is of paramount importance, and so we use our larger power supply with the small inductor coils in Helmholtz configuration for field generation. The smaller supply powers the large inductor in anti-Helmholtz configuration to produce the magnetic field gradient.

In this configuration, the magnetic field ramps exponentially to the target field with a $\sim$ 5ms time constant, still far too slow for our needs. Instead, the magnetic field ramp is engineered to overshoot the target field followed by a quick damping to reach the target field. Effective ramp speeds of 50G/ms are achieved in this way.

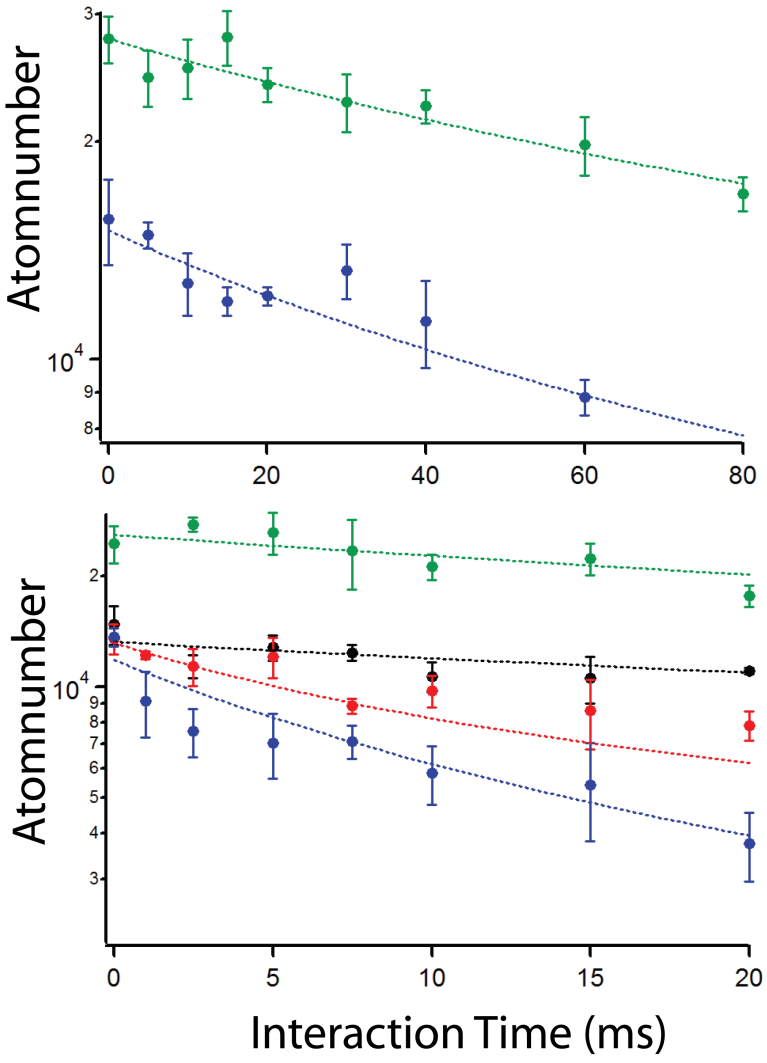

Figure 6.5: Comparison of atom loss curves for lithium and ytterbium at 100G and 450G magnetic fields. (top) Inelastic loss curve without the presence of lithium at 100G (green data) and 450G (blue data). The dashed lines are the best fits of these data sets with extracted K_2 inelastic loss constants of $1.3 \pm 0.2 \times 10^{-11}\text{cm}^3/\text{s}$ (100G) and $3.7 \pm 0.6 \times 10^{-11}\text{cm}^3/\text{s}$ (450G). (bottom) Inelastic loss curves in the Yb*+Li system at 100G and 450G. Yb* atom numbers are the green (100G) and blue (450G) datasets and Li atom numbers are the black (100G) and red (450G) datasets. The dashed lines are the best fits of these data sets fit to the 0–15ms data (100G) and 0–10ms data (450G). The extracted Li+Yb* inelastic constants are $1.5 \pm 0.4 \times 10^{-11}\text{cm}^3/\text{s}$ at 100G and $2.6 \pm 0.3 \times 10^{-10}\text{cm}^3/\text{s}$ at 450G.

Once at the target field, we allow the lithium and metastable ytterbium atoms to interact for a variable amount of time before imaging the remaining atoms. This results in lithium and metastable ytterbium atom-loss curves which contain information about the inelastic loss constant, shown in Fig. 6.5.

An experimental run consists of typically 7–10 interaction times between 0 and 20ms. The order of the interaction times is randomized to guard against systematic effects e.g. magnetic fields changing slightly due to electromagnets heating. For every Li-Yb* interaction time, up to 16 single species images are taken, each requiring the entire $\sim$ 30s experimental sequence. Single species imaging is used to maximize the signal to noise of each image; obtaining accurate density profiles with as few as 2000 atoms remaining in the gas is essential.

The experiment is repeated at every magnetic field with lithium removed from the trap. This allows us to ascertain the Yb*+Yb* dynamics without the influence of lithium. The inelastic loss constant is much smaller for Yb*+Yb* interactions and requires interaction times of up to 80ms.

6.6 Analysis

The atom-loss dynamics we observe are the sum of all loss processes, which include the two-body inelastic processes we wish to study, as well as collisions with background gases, single body relaxation of the Yb* atoms, three-body inelastic processes, and losses due to evaporation.

Background gas collisions and single body relaxation of the Yb* atoms are $\sim$ 25s and 15s processes which contribute negligibly to the $\sim$ 10ms processes we observe.

Losses due to evaporation can be modelled as [56]

$$\dot{N} = -2(\eta - 4)e^{-\eta}\gamma N \tag{6.1}$$

where η is the ratio of trap depth to temperature and γ is the thermalization rate $n\sigma v$. Ascertaining the magnitude of this effect is difficult as the thermalization rate

is dependent on the scattering length, which may have attenuated resonance features due to the presence of the lossy Feshbach resonance. A very large 100nm Yb*+Yb* scattering length results in an evaporative time constant of $\sim$ 130ms for our experimental parameters ($\eta = 6.5$). Therefore, evaporative effects should only affect Yb* losses on the timescales of our experiment near a Yb*+Yb* Feshbach resonance. Lithium remains immune to evaporative effects due to its large ratio of trap depth to temperature.

Three-body inelastic loss processes are unlikely to contribute to system dynamics due to the relatively small Yb*(Li) peak densities of $1.0(5.1) \times 10^{12}/\mathrm{cm}^3$. Near a Feshbach resonance, three-body inelastics are also strongly enhanced, however two-body loss processes are still expected to dominate the dynamics. Our data quality is not sufficient to extract separate K_2 and K_3 loss constants. As such, care must be taken in interpreting K_2 values extracted near potential Feshbach resonances.

The atom-loss curves are fit to the integrated two-body loss equations

$$\begin{aligned} \dot{N}_{Yb*} &= -2K_2 N_{Yb*}^2 \langle n_{Yb*} \rangle - K_2' N_{Yb*} N_{Li} \langle n_{Li} \rangle \\ \dot{N}_{Li} &= -K_2' N_{Yb*} N_{Li} \langle n_{Yb*} n_{Li} \rangle \end{aligned} \tag{6.2}$$

where $N_{Yb*(Li)}$ is the Yb*(Li) atom number, $K_2(K_2')$ are the two-body loss coefficients for Yb*+Yb*(Yb*+Li) interactions, and $\langle n_{Yb*} \rangle (\langle n_{Li} \rangle)$ are the Yb*(Li) particle density overlaps with Yb*

$$\begin{aligned} \langle n_{Yb*} \rangle &= \left(8\pi^{3/2} \bar{R}_{Yb*}^3 \right)^{-1} \\ \langle n_{Li} \rangle &= \left((2\pi)^{3/2} (R_{x_{Li}}^2 + R_{x_{Yb*}}^2)^{1/2} (R_{y_{Li}}^2 + R_{y_{Yb*}}^2)^{1/2} (R_{z_{Li}}^2 + R_{z_{Yb*}}^2)^{1/2} \right)^{-1} \\ \bar{R} &= (R_x R_y R_z)^{1/3} \\ R_i &= (\frac{k_B T}{m \omega_i^2})^{1/2} \end{aligned} \tag{6.3}$$

where ω_i is the trapping frequency in the $\hat{i}$ direction, T is the temperature of the gas, and m is the mass of the atom. Perturbations to the density overlaps due to the

vertical dimple trap are numerically calculated and included in the density overlaps used in our fits.

In addition to the atom-loss dynamics, temperature dynamics are important to understand for accurate analysis of the data. While evaporative effects do not play a role, inelastic losses tend to cause heating in the system. Atoms from the densest and coldest regions of the trap experience the largest loss rates. We have measured the heating of the lithium and ytterbium gases at several magnetic fields, and find a very mild increase in temperature; up to $\sim 0.3\mu$K/atom of energy is deposited into the Yb* gas. Lithium is nearly unaffected as the density of ytterbium is approximately constant over the lithium cloud. The effects of this temperature increase do not appreciably affect our results.

An additional unforeseen effect alters the atom-loss dynamics: a time dependent spatial offset of the Yb* atoms. The Yb* atoms consistently move along the single beam trap axis during the interaction time. The movement emulates that of a constant force, starting slow and becoming faster. The effect becomes more pronounced as the magnetic field increases. At the time of writing, the exact cause is unknown.

We postulate that the magnetic field created by the small inductor in Helmholtz configuration is not aligned perpendicularly to the ODT axis. The force along the axis of the ODT in this case would be $F = \mu B' \cos(\theta)$ with θ the angle between the ODT axis and the local magnetic field direction. A one degree misalignment results in a 0.02g force resulting in a $\sim 190\mu$m shift in the trap center due to the intentionally applied anti-gravity magnetic gradient. Reasonable mis-alignments of the magnetic field cannot result in the large (mm scale) spatial offsets that we observe. The increased effect at larger fields points towards the small inductor creating its own sizable magnetic gradient in Helmholtz configuration.

The end result of the spatial offset, is that the density overlap of the atomic gases changes in time in a field dependent manner. Attempts to accurately model and account for these effects are possible, however, we take the simpler route and exclude

data for which the spatial offset of the Yb* atoms would lead to a
$gt10\%$ change in the spatial overlap function. This typically limits the interaction times to 12-15ms.

The Yb*+Yb* inelastic loss parameter is fit using the data collected with lithium removed from the trap. The atom-loss has a closed form solution $N(t) = N_0/(1 + K_2 N_0 \langle n_{Yb*} \rangle t)$ with N_0 the initial Yb* atom number and K_2 the inelastic loss constant. Example fits are shown in Fig. 6.5. The resulting Yb*+Yb* inelastic loss spectrum is shown in Figure 6.6.

The Li+Yb* inelastic loss parameter is somewhat more difficult to extract as there is no closed form solution. A fit is obtained by numerical integration of the differential equations with a given set of fit parameters. There are three free parameters: the two initial atom numbers, and the Yb*+Li inelastic loss constant (the Yb*+Yb* loss constant is fixed to the value extracted from the Yb* only data). A gradient descent search is used to find the best local values for a given starting set of these three parameters. Performing many such gradient searches with widely varying starting conditions allows one to approximate a best global value. Example fits are shown in Fig. 6.5. The resulting Yb*+Li inelastic loss spectrum is shown in Fig. 6.6.

While the Yb*+Yb* inelastic loss remains fairly constant over the 100–520G data range, the Yb*+Li inelastic loss has several exciting features. First, we note that the Yb*+Li inelastic loss constant at 450G approaches the universal limit for two-body collisions at these temperatures of $2.9 \times 10^{-10}\text{cm}^3/\text{s}$ [86]. This indicates a very strong collision channel at 450G.

The factor of ~ 8 increase in the inelastic loss constant from 100G to 450G shows that there are strong magnetic field dependent interactions. The reduction in the inelastic loss constant for 490–520G data suggest that these interactions may be related to resonant behavior.

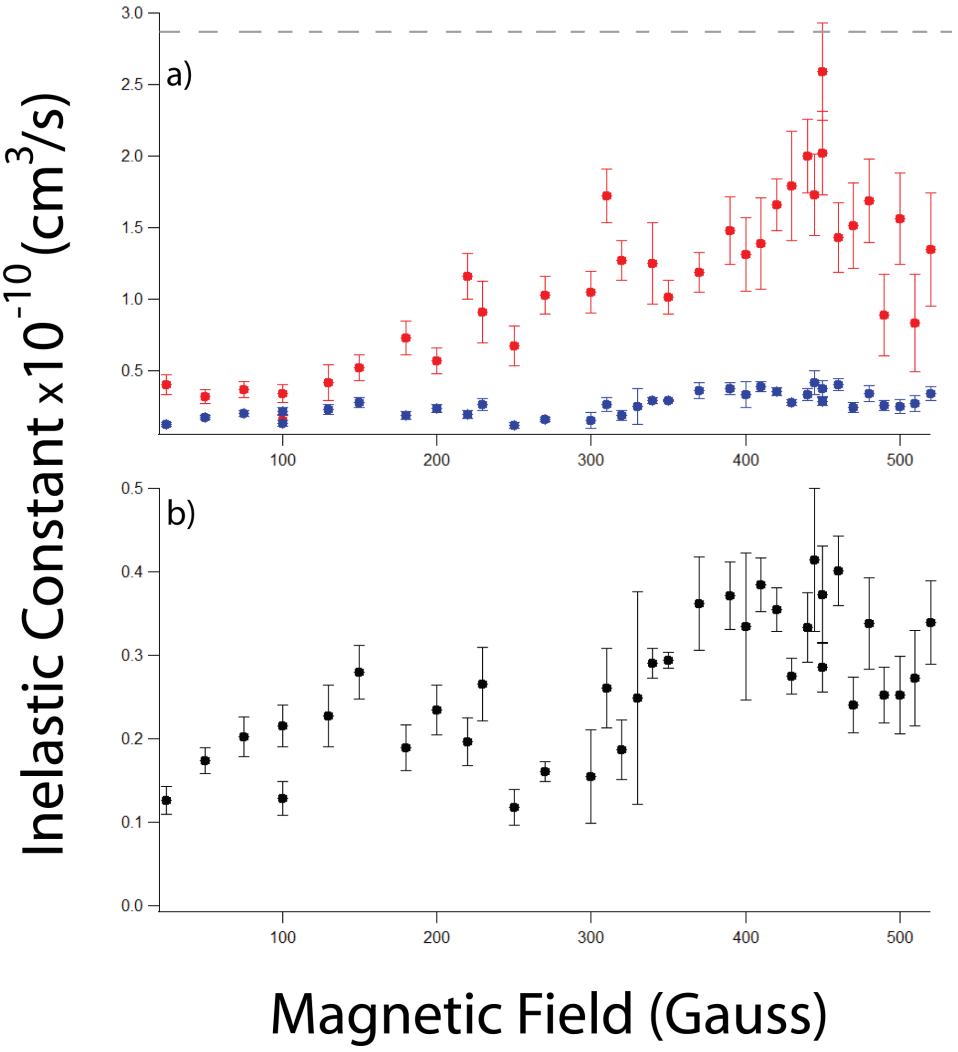

Figure 6.6: Inelastic loss spectra for the Yb*+Li system at 1.7μK. (a) The extracted Li+Yb* (red data) and Yb*+Yb* (blue data) loss constant as a function of magnetic field. The gray dashed line is the Li+Yb* universality limit for collisions at these temperatures. (b) The Yb*+Yb* inelastic loss constant spectrum.

Our collaborators at Temple University have created a theoretical model of the Yb*+Li system[87]. A full Yb*+Li scattering potential is constructed, and fit to the inelastic scattering data presented here. This theory indicates the 450G scattering peak is a Feshbach resonance, as well as indicating three weaker resonances near 310, 220, and 190G. The theory indicates these resonances are multi-channel induced; the scattering state couples to several bound states and the interference between these scattering phase shifts results in the resonance. Further study of the system is needed to confirm these results and ascertain the feasibility of using such anisotropic resonances.

Chapter 7

CONCLUSIONS AND OUTLOOK

This thesis has reported on an apparatus which produces ultracold co-trapped gases of atomic lithium and ytterbium. I have detailed the methods used to produce and measure properties of these gases. Experiments leading to quantum degeneracy of these gases and measurements of their interaction strength are briefly described.

The first explorations of the new ^{6}Li + metastable ytterbium system have been conducted. The transfer of ytterbium atoms to this trapped metastable state extends the possibilities of our ultracold mixture experiment. These possibilities include tunable interactions and potentially efficient molecule creation via magneto-association.

I have detailed the transfer of ytterbium atoms to the $^3P_2$ metastable state. A scheme to spin-purify the metastable ytterbium is also described. After purification, arbitrary spin compositions of the metastable state can be created via coherent RF transfer methods demonstrated in this thesis.

The microscopic interaction properties which determine bulk-gas dynamics has been described. Measurements of the bulk-gas dynamics between lithium and metastable ytterbium as a function of magnetic field have been conducted and reported in this thesis. The results of these measurements indicate that tunable interactions between ^{6}Li in the $|1\rangle$ state and metastable ^{174}Yb in the $m_J = -1$ state may be achievable through a potential Feshbach resonance near 450G. Such a Feshbach resonance may be an excellent path towards creation of ultracold ground state LiYb molecules. Further work must be conducted to confirm these results and investigate the potential usefulness of such a resonance.

Future experiments involving ^{6}Li and metastable ytterbium are planned. These

experiments will take advantage of the results obtained here to make several important technical improvements to the system. Direct excitation to the metastable state solves many of the problems faced in the work described in this thesis. Heating and momentum transfer are all but eliminated as each atom scatters just one photon. Direct excitation to spin-pure states is easily achieved for all substates, notably including the fermionic isotopes of ytterbium. Yb*+Yb* interactions are eliminated in a fermionic spin-purified sample resulting in a far more robust system with the potential for stronger Feshbach resonances. A 3-D optical lattice [55] can also eliminate metastable ytterbium contact interactions with both ytterbium and metastable ytterbium atoms by creating an $n = 1$ Mott insulator [55] of the ground state ytterbium atoms. The heating and recoil problems faced by this experiment can also be eliminated in a very strong lattice where $\hbar\omega$ is larger than the recoil energy.

Progress towards these goals is already being made. The dimple trap used in the experiments described here is derived from the intended vertical optical lattice beam. Successful Kaptiza-Dirac diffraction of the ytterbium atoms has been shown using this beam and its retro-reflection. Procurement of a laser source and locking scheme for the ultra-narrow ($2\pi \times 11$mHz) direct transition may prove a more difficult task.

Current research has shifted towards photo-association spectroscopy of ^{6}Li and ^{174}Yb . This work will provide precise measurements of the ^{6}Li -^{174}Yb s-wave scattering length. Work on two photon photo-association has just begun, which will map the ground state lithium-ytterbium interaction potential. This will provide vital knowledge of the molecule binding energies and wavefunctions which is required for efficient transfer of excited state molecules to the ground state. Should Feshbach resonances prove to be difficult for molecule creation, photo-association may also prove the best path towards creation of LiYb molecules.

A separate ongoing project is the development of an optical frequency comb. Once LiYb molecules are created in an excited state, either by Feshbach resonance or photo-association, transfer to the protected ground state is of utmost importance. A fre-

quency comb allows two lasers of vastly different wavelength to be locked to the same source. This allows efficient processes such as stimulated raman adiabatic passage to be used in transferring the molecules to the ground state.

It is an exciting time in the University of Washington ultracold lithium-ytterbium mixture experiment. Trapped LiYb molecules are just over the horizon, and one can expect transfer to the ground state to follow not long after.

Appendix A

PRODUCTION OF QUANTUM-DEGENERATE MIXTURES OF YTTERBIUM AND LITHIUM WITH CONTROLLABLE INTERSPECIES OVERLAP

Production of quantum-degenerate mixtures of ytterbium and lithium with controllable interspecies overlap

Anders H. Hansen, Alexander Y. Khramov, William H. Dowd, Alan O. Jamison, Benjamin Plotkin-Swing, Richard J. Roy, and Subhadeep Gupta

Department of Physics, University of Washington, Seattle, Washington 98195, USA

(Received 12 November 2012; published 16 January 2013)

Quantum-degenerate mixtures of one-electron and two-electron atoms form the starting point for studying few- and many-body physics of mass-imbalanced pairs as well as the production of paramagnetic polar molecules. We recently reported the achievement of dual-species quantum degeneracy of a mixture of lithium and ytterbium atoms. Here we present details of the key experimental steps for the all-optical preparation of these mixtures. Further, we demonstrate the use of the magnetic field gradient tool to compensate for the differential gravitational sag of the two species and control their spatial overlap.

DOI: 10.1103/PhysRevA.87.013615 PACS number(s): 67.85.Pq, 37.10.De, 34.20.−b, 05.30.Fk

I. INTRODUCTION

Elemental quantum mixtures provide a path toward ultracold diatomic polar molecules [1]. Utilizing a second, distinguishable atomic species, such mixtures may also allow for impurity probing of quantum phenomena in an ultracold gas. Interspecies Feshbach resonances can enable studies of few- and many-body phenomena in mass-imbalanced systems. There has been great progress in the development of ultracold bi-alkali-metal gases, motivated by applications towards sympathetic cooling of Fermi gases [2], studies of strongly interacting mass-mismatched systems [3], and production of ultracold polar molecules [4].

Extending the choice of mixture components to include other parts of the periodic table, new scientific opportunities arise. For instance, the ground state of the diatomic molecule might now have a magnetic moment, leading to *paramagnetic* polar molecules. This has been a key motivation for our pursuit of the lithium-ytterbium combination.

The $^2\Sigma$ ground state of the YbLi molecule makes it a candidate system for simulating lattice spin models with applications in topological quantum computation [5]. Additionally, the Yb-Li mixture possesses a very large mass ratio, and a range of isotopic combinations with Bose and Fermi statistics. Tunable interactions between the components can lead to the creation of novel Efimov states [6]. When confined in an optical lattice, a heavy-light fermion mixture can realize the binary alloy model [7], with applications in simulating exotic condensed matter phases (e.g., studies of pattern formation [8,9]).

In previous work, we assessed the collisional stability of the Yb-Li mixture in weakly interacting regimes, and explored the strengths of various inelastic channels in a three-component mixture with one resonantly interacting pair. In this paper we describe the experimental details of our setup, stressing the areas that have required development beyond typical single-species experiments. We report on the production of large-number Bose- and Fermi-degenerate ytterbium gases and assess the cooling limits of the Yb-Li mixture from interspecies interactions. Finally we report the demonstration of interspecies spatial overlap control over a large temperature range, using a magnetic field gradient.

The remainder of this paper is organized as follows. In Sec. II we describe the salient features of our trapping apparatus. Section III discusses our atom manipulation and cooling techniques. In Sec. IV we summarize the performance of our system for the production of degenerate Yb-Li mixtures in different interaction regimes. Section V describes our interspecies spatial-overlap control scheme. Finally, in Sec. VI we present our conclusions and outlook.

II. TRAPPING APPARATUS

Our trapping apparatus uses standard techniques for single-species experiments, applied to two independent atomic sources, as pictured in Fig. 1. Yb and Li beams emerge from separate effusion ovens, and are directed towards the common "main" chamber through individually optimized Zeeman slower sections. The long slower tubes [lengths 93 cm (Li) and 40 cm (Yb), inner diameter 18 mm] also provide differential pumping. An additional stage of differential pumping is provided by a short tube (length 11 cm, inner diameter 5 mm) separating each oven assembly from an independently pumped "intermediate" chamber. We maintain the vacuum in each subchamber with ion pumps, and augment the main chamber vacuum with a titanium sublimation pump. During standard operation, the pressures are approximately $P_{\text{Li oven}} \simeq 3 \times 10^{-8}$ Torr, $P_{\text{Yb oven}} \simeq 1 \times 10^{-7}$ Torr, and $P_{\text{main}} < 1 \times 10^{-10}$ Torr, as measured by ion gauges. Each beamline is equipped with a gate valve, positioned between the oven and intermediate chambers. This allows us to perform single-species experiments, even when the other oven is being serviced.

A. Lithium and ytterbium ovens

The effusion ovens each consist of a vertically oriented "cup," connected via a 90° elbow to a nozzle: a 4-mm-diameter aperture in the Conflat (CF) assembly. We stabilize the Yb (Li) cup temperatures to 400 (375) °C during operation. The nozzles are stabilized at 450 °C permanently to prevent deposition and congestion. The areas between each nozzle and gate valve contain mechanical beam shutters mounted on rotary feedthroughs to control the atom flow to the main chamber, and a copper cold plate (−7 °C) to collect the atomic flux not directed towards the main chamber.

All heated oven parts are of type-316 stainless steel, while the rest of the vacuum apparatus is type-304 stainless steel.

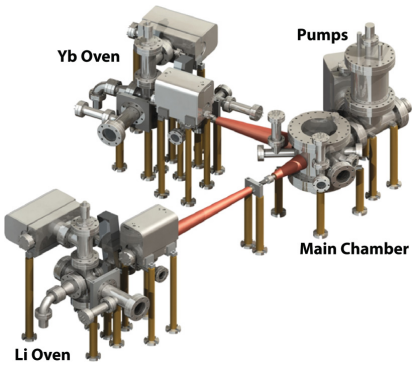

FIG. 1. (Color online) Schematic figure of dual-species apparatus. Ytterbium and lithium are prepared in separate ovens and slowed in individually optimized Zeeman slowers. Each oven is separated from the main chamber by two stages of differential pumping and an independently pumped intermediate chamber. The central part of each intermediate chamber (hidden from view) is a 2.75 in. six-way cross.

For the heated sections of the lithium oven we use nickel CF gaskets, which are more resilient than copper in high-temperature environments in the presence of lithium [10]. We have found, however, that nickel gaskets in the presence of hot Yb vapor undergo corrosive chemical reactions, which compromise the integrity of the vacuum after several months of operation. We now use copper gaskets in the ytterbium oven, which have been trouble-free for two years.

B. Main chamber

Our main chamber has a cylindrical geometry with ten viewports for optical access (Fig. 2). The top and bottom are sealed off by 10 in. CF flanges, into which custom-made re-entrant "buckets" for the electromagnets are recessed. Each bucket also has a 2.75 in. viewport for vertical MOT beams.

We keep the sapphire entry viewports for the Yb (Li) Zeeman slowing laser beams at a permanent 200 (250) °C; otherwise, metallic deposition is clearly evident. All other viewports are BK7 glass antireflection coated at the wavelengths for laser cooling and optical trapping of the two species.

Our experimental setup employs two pairs of electromagnetic coils, shown in Fig. 2. We apply antiparallel currents to the inner pair to generate the quadrupole field for the magneto-optical traps (MOTs), while the outer pair, arranged in parallel (Helmholtz) configuration, provide bias fields to access Feshbach resonances.

The MOT coils produce a vertical gradient of 1.0 G/cm/A, while the bias coils produce 4.2 G/A. We can electronically switch the MOT coils to parallel configuration, in which they yield 2.4 G/A . This allows for larger bias fields and improves the speed of magnetic field ramps.

Each coil is wound from hollow, square copper tubing (outer dimension 1/8 in., inner dimension 1/16 in.). A bias-field upper bound of 1000 G is set by the flow rate of the cooling water through the electromagnets at 100 psi building pressure.

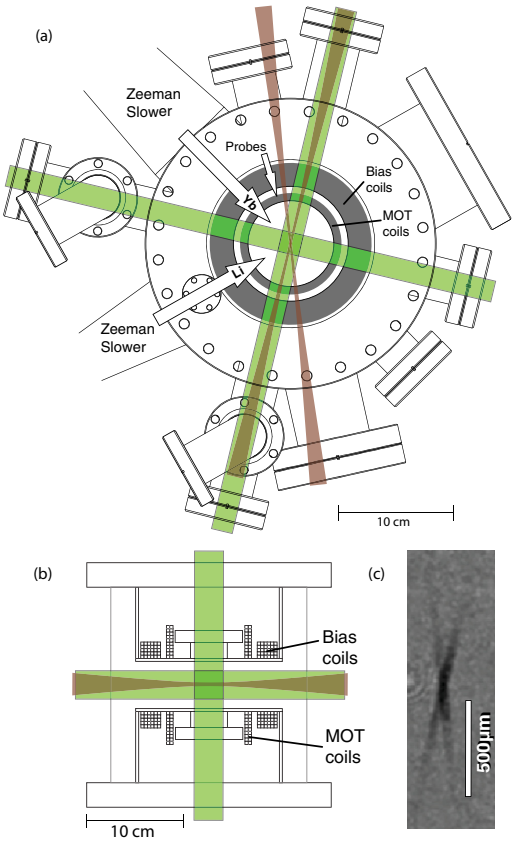

FIG. 2. (Color online) (a) Top view of main chamber, showing the configuration of magneto-optical trap (MOT) beams (green), optical dipole trap (ODT) beams (brown), magnetic coils (gray), and orientation of Yb and Li atomic beams and probe beams (arrows). Vertical MOT beams, vertical probe beams, slowing laser beams, and compensation coils are omitted for clarity. (b) Side view of main chamber, showing vertical and horizontal MOT beams, ODT beams, and recessed buckets with magnetic coils. (c) Sample in-trap absorption image of Yb atoms taken along the vertical axis, immediately after transfer to the ODT. The density distribution clearly shows the crossed-beam geometry. Upon further cooling, the atoms collect in the central crossing point of the two beams.

In order to reach higher fields (up to 1700 G), we employ a booster pump that raises the water pressure to 400 psi.

III. DUAL-SPECIES COOLING AND TRAPPING

We use three laser systems for slowing and laser cooling of lithium and ytterbium: one for ^{6}Li, addressing the $^2S_{1/2} \rightarrow {}^2P_{3/2}$ ($D2$) transition at 671 nm, and two for Yb, addressing the $^1S_0 \rightarrow {}^1P_1$ transition at 399 nm and $^1S_0 \rightarrow {}^3P_1$ (intercombination) transition at 556 nm (Fig. 3). We use acousto-optical modulators (AOMs) to provide all the required

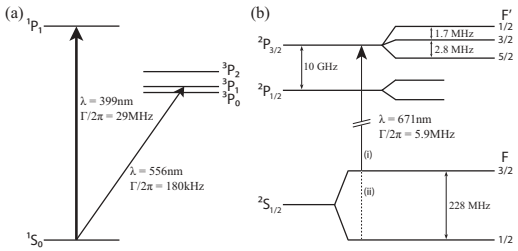

FIG. 3. Relevant energy levels for laser cooling of (a) ^{174}Yb and (b) ^{6}Li. Transitions used for trapping and cooling (see text) are indicated with arrows. In ^{173}Yb, only the excited states acquire hyperfine structure and the cooling lasers are tuned to the appropriate cycling transitions. To address lithium, we require separate frequency components for the cooling (i) and repumping (ii) transitions. The hyperfine splitting of the $^2P_{3/2}$ state is not resolved.

frequency shifts needed for slowing, trapping, repumping, and probing of the atoms.

We derive the 671 nm light from a commercial laser system (Toptica TA100), consisting of an external-cavity diode laser (ECDL) and a tapered amplifier (TA) system. We frequency-stabilize the laser using saturated absorption spectroscopy in a home-built vapor cell, with a lithium sample heated to 420 °C.

We derive the 399 nm light, used for slowing and imaging of Yb, from another commercial system (Toptica TA-SHG pro), consisting of an ECDL at 798 nm, a TA, and a second-harmonic generation (SHG) cavity. We frequency-stabilize this laser using saturated absorption spectroscopy in a commercial hollow-cathode lamp (Hamamatsu Laser Galvatron L2783).

We derive the 556 nm light, used for the Yb MOT, from another commercial system (Toptica FL-SHG pro), consisting of an ECDL, a fiber amplifier, and an SHG cavity. Since the linewidths of the blue and green transitions are different by more than two orders of magnitude, the two lasers require very different Yb column densities for spectroscopy. We frequency-stabilize this laser using saturated absorption spectroscopy in a home-built vapor cell with an ytterbium sample heated to 420 °C. In our setup, to reduce deposition on the cell viewports, we independently heat the viewport flanges while keeping the regions between the atomic sample and the glass at a lower temperature. We have also found it useful to reduce the diameter of the outermost section of the Yb cell on either end to reduce conduction.

A. Zeeman slowers

Each MOT loads from a separate Zeeman-slowed atomic beam. The solenoids for the Zeeman slowers are wound from the same copper wire as the MOT and bias coils. The Li slower uses a "spin-flip" configuration, consisting of a 60-cm-long decreasing-field section followed by a 15-cm-long increasing-field section. We operate each component at 30 A, yielding a net magnetic field variation $|\Delta\mathbf{B}|$ of 980 G. The atoms are slowed by a 40 mW laser beam, 732 MHz red-detuned from the $D2$ transition for the $F = \frac{3}{2}$ state. We derive the slower beam from an injection-locked diode laser. By adding a second injection beam 228 MHz blue-detuned from the first, we obtain light for repumping from the $F = \frac{1}{2}$ ground state within the slower.

The Yb slower consists of a single 40-cm-long increasing-field stage, operated at 15 A to yield $|\Delta\mathbf{B}| = 240$ G. The slowing beam has a power of 100 mW, and a red-detuning of 365 MHz from the $^1S_0 \rightarrow {}^1P_1$ transition.

Compensation coils, mounted opposite to each slower on the main chamber, cancel magnetic fringe fields at the position of the trapped atoms. Together with the vertical bias coils, the slower coils also serve as tools to move the center of the MOT quadrupole along all spatial axes, essential for relative positioning of the traps, as discussed below.

B. Magneto-optical traps

For magneto-optical trapping of the two species we use a standard single-species setup with retroreflected MOT beams [11], modified to accommodate a second atomic species. We combine the beams for the two species using a dichroic mirror, and divide the combined beam into three beams using broadband polarizing beam splitters. The polarizations are controlled by single-wavelength half-wave plates and dual-wavelength quarter-wave plates (Foctek).

Several factors have to be considered in determining the optimum parameters for dual-species laser cooling. Due to the difference in linewidth of the Li $D2$ and Yb intercombination lines (factor of 32) the two MOTs are optimized at very different magnetic gradients (see Table I). Furthermore, the optimal duration of the transitional cooling step (compression) before loading into the ODT differs greatly for the two species. Finally, the two species experience significant losses through inelastic collisions when the magneto-optical traps are spatially overlapped.

We find that the best performance in our setup is achieved using a sequential loading scheme, as described in [12], with typical parameters as listed in Table I. To summarize, we load Yb alone for 10–30 s, depending on experimental requirements. During this time, the detuning of the trapping light is modulated with an amplitude of 20 linewidths, at a frequency of 50 kHz, to increase the phase-space volume of the trapping region. We then compress Yb in 200 ms, and transfer it to the ODT. We subsequently optimize the

TABLE I. Typical experimental parameters for loading of ^{6}Li, ^{174}Yb, and ^{173}Yb: laser intensity I and red-detuning δ, and magnetic axial (vertical) field gradient B'. Two sets of numbers are provided for each isotope, reflecting the parameters for MOT loading and for the end point of compression (see the text) before transfer to the ODT. I refers to the total laser intensity in all three retroreflected beams; the total optical intensity at the atoms is twice the listed value. Γ and $I_{\rm sat}$ for Yb refer to the properties of the intercombination transition.

		^{6}Li $F = 3/2$	^{6}Li $F = 1/2$	^{174}Yb	^{173}Yb
Load	I	$60I_{\rm sat}$	$55I_{\rm sat}$	$750I_{\rm sat}$	$750I_{\rm sat}$
	δ	6Γ	3.5Γ	$(55 \pm 20)\Gamma$	$(40 \pm 20)\Gamma$
	B'	20 G/cm		3 G/cm	3 G/cm
Final	I	$0.07I_{\rm sat}$	$0.08I_{\rm sat}$	$0.8I_{\rm sat}$	$2I_{\rm sat}$
	δ	1.5Γ	3Γ	2Γ	4Γ
	B'	60 G/cm		18 G/cm	25 G/cm

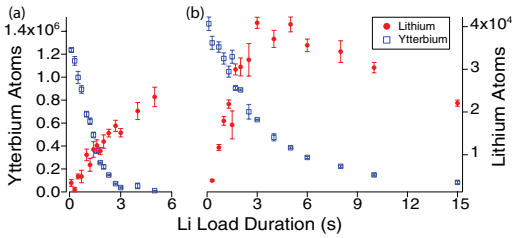

FIG. 4. (Color online) Number of trapped atoms, after a variable Li load time and 1 s hold in the ODT at fixed depth. (a) [(b)] shows results with a vertical bias field of 0 (2) G, corresponding to a 1 mm center-of-mass displacement of the Li MOT. In the favorably displaced case (b), Li numbers are optimized at a finite load time; at longer load times sympathetic cooling becomes inefficient due to low Yb numbers. Each error bar represents statistical fluctuations of four experimental iterations.

quadrupole field for lithium, load the Li MOT for 0.5–4 s (depending on experimental requirements), compress in 50 ms, and transfer to the ODT. A short (100 μs) pulse of light resonant with the Li $F = \frac{3}{2}$ $D2$ transition optically pumps the Li atoms into the ground $F = \frac{1}{2}$ state.

The positioning of the Li MOT during load is crucial for large dual-species samples as can be seen in Fig. 4. The large losses for suboptimal positioning can be interpreted as a consequence of elastic collisions that heat Yb through contact with the Li MOT, and also of inelastic collisions of ground-state Yb with electronically excited Li atoms in which both constituents are lost. The latter process also impedes the rate at which the Li MOT loads, as can be observed in Fig. 4.

We mitigate this effect by applying a bias field during the Li load, which spatially offsets the MOT from the ODT. With a vertical bias field of 2 G the lifetime of Yb atoms is quadrupled. Although this lifetime is less than the vacuum-limited lifetime of ∼45 s, this still leads to simultaneous confinement of 10^6 Yb atoms and 10^5 Li atoms in the ODT, immediately after switching off all the laser cooling beams.

Due to the greater abundance of Yb in the ODT, as well as its lower MOT temperature, Yb acts as a coolant for Li. At zero bias field we observe that, in the absence of Yb, most of the Li atoms spill from the trap during the first 1 s after transfer from the MOT. With a large bath of Yb present, these losses are mitigated, as the Li atoms thermalize with the bath.

C. Optical dipole trap

We derive our ODT from an ytterbium fiber laser (IPG Photonics YLR-100-LP) that can provide up to 100 W laser power at 1064 nm. During standard operation, we run the laser at 40 W. We send the laser output through an AOM and split the first-order output into two components of equal power and orthogonal polarization. Each component is focused to a waist of ≈26 μm and crossed at a 20° angle at the atoms. As shown in Fig. 2, both beams are horizontally aligned through the chamber. This configuration provides a straightforward geometry for our crossed ODT.

We perform evaporative cooling by controlling the efficiency of the ODT AOM. The geometry of the trap is thus preserved during evaporation, and trap frequencies may be interpolated between measurements at various depths [13].

D. Evaporative and sympathetic cooling strategies

For a given intensity of the 1064 nm ODT beam, the optical potential for Li is greater than that for Yb by a factor of about 2. Thus, at the same temperature, Yb will evaporate from the trap significantly faster than Li. For this reason, and because the Li (linear) size is smaller by a factor of 0.7 at equal temperature, the most practical cooling strategy involves sympathetically cooling Li in a bath of Yb. We thus optimize the initial conditions to a larger proportion ($\geqslant$90%) of trapped Yb, and set the rate of evaporative cooling to match the interspecies thermalization time, which is of order 1 s throughout. This method works well even in the regime of quantum degeneracy, since the condensation temperature for Yb is an order of magnitude lower than the Li Fermi temperature (for equal Li and Yb numbers). A more detailed discussion of this scheme can be found in [14].

We believe that this method of cooling will readily transfer to other alkali metal + spin-singlet systems, where some performance aspects may be even better than in Yb-Li. The number of interspecies collisions necessary for thermalization between particles of masses m_1 and m_2 is of order $2.7/\xi$, where the dimensionless parameter $1/\xi = (m_1 + m_2)^2/4m_1m_2$ [15]. For ^{6}Li and ^{174}Yb, $2.7/\xi = 21$, which is relatively large. Furthermore, since Li cannot be laser cooled to such low temperatures as Yb, a considerable amount of Yb is lost through evaporation during initial thermalization. Both of these effects will be less severe with other alkali-metal atoms such as Na, K, Rb, and Cs. We also note that a similar mismatch of trap depth in a 1064 nm ODT will exist and a similar immunity to two-body inelastic losses is expected, both advantageous for sympathetic cooling with Yb [16].

E. Simultaneous dual-species imaging

We simultaneously probe the collocated, optically trapped clouds of Li and Yb using absorption imaging. The imaging beams are overlapped before they enter the vacuum chamber, using a broadband polarizing beam splitter. The beams are split after they emerge from the vacuum chamber using dichroic mirrors, and the cloud images are projected onto two different regions of the CCD camera chip. Absorption images for both clouds are obtained for each experimental iteration.

IV. Yb-Li QUANTUM MIXTURES

Our quantum mixture preparation relies on the direct evaporative cooling of Yb which then cools the co-trapped Li sympathetically, as described in Sec. III D. Cooling in the absence of an external magnetic field leads to weakly interacting Bose-Fermi mixtures. By applying external magnetic fields, strongly interacting regimes may then be accessed through available Feshbach resonances. In this section, we first report our current system performance for producing quantum-degenerate gases of single-species Yb isotopes. We then present the production of weakly interacting Yb-Li mixtures through sympathetic cooling. Finally we briefly discuss regimes of strong interactions in Yb-Li mixtures.

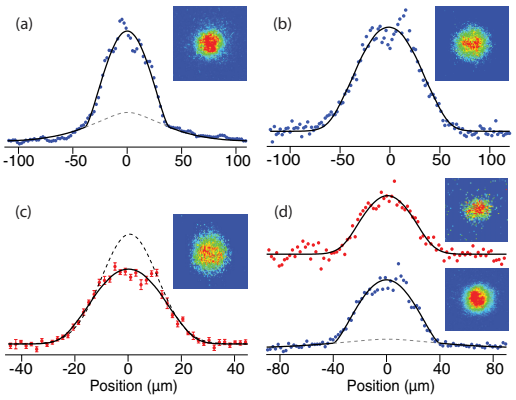

FIG. 5. (Color online) Density cross sections of lithium and ytterbium from absorption images (insets) of degenerate gases. (a) Quantum-degenerate gas of ^{174}Yb atoms with 2.5×10^5 atoms in the condensate imaged at a time of flight (TOF)12 ms. (b) Degenerate Fermi gas of 1×10^5 ^{173}Yb atoms with $T/T_F = 0.3$ and TOF 5 ms. (c) Degenerate Fermi gas of 1.6×10^4 ^{6}Li atoms with $T/T_F \approx 0.06$ and TOF 0.4 ms. (d) Simultaneous quantum degeneracy of ^{6}Li and ^{174}Yb with 2×10^4 (3×10^4) atoms of Li (Yb). $T/T_F \approx 0.2$ for Li and TOF 0.5 (10) ms. Solid lines are least-square fits to local-density-approximation models for Bose and Fermi gases, while dashed lines are classical fits to the wings of the distributions.

A. Quantum-degenerate ytterbium

Our current apparatus has several new features beyond what was reported in [14]. Our Yb laser cooling procedure now employs greater power and frequency sweep range in the MOT beams during load (see Sec. III). The optical trap now features electronic stabilization of depth and adjustable volume through a time-averaged potential generated by frequency modulation of the ODT AOM [18]. This "painting" of the potential increases the volume of the loading trap and allows a much larger load of Yb. Optimization of both loading and evaporation is obtained by continuously reducing the volume and the depth of the trap during evaporative cooling. Loading from 7×10^7 laser-cooled atoms at a temperature of $\simeq$20 μK, we achieve an optical trap load of up to 5×10^6 atoms and ^{174}Yb condensate numbers of 3×10^5 [Fig. 5(a)]. Applied to fermionic ^{173}Yb, we can achieve up to 1.2×10^5 [Fig. 5(b)] atoms in a mixture of the six spin states at $\frac{T}{T_F} = 0.3$. By reducing the loading and evaporative cooling sequence times, we can improve the repetition rate of Yb condensate production to 10 s, with (5×10^4)-atom Bose-Einstein condensates (BECs). Fast experimental repetition rates are crucial to precision measurements with BECs, which depend on large statistical data samples [19].

B. Weakly interacting quantum-degenerate Yb-Li mixture

For dual-species experiments in which Li is co-trapped and sympathetically cooled by Yb, the time-averaging option is not used as the accompanying reduction in trap depth is too great to efficiently load Li into the optical trap. As noted earlier, the larger polarizability of Li makes Yb a suitable sympathetic coolant. At the lowest temperatures, the large mass difference affects the standard procedure in two significant ways—the degeneracy temperatures for equal numbers are different by an order of magnitude, and the differential gravity-induced trap modification is relatively large.

By controlling the final depth of the evaporation ramp, we achieve simultaneous degeneracy, with similar atom numbers (few $\times 10^4$) of each species. The quantum-degenerate Yb-Li mixture at zero external magnetic field [Fig. 5(d)] is weakly interacting with interspecies scattering length of magnitude $13a_0$ [12,14,20]. In our system, $N_{\rm Li} \approx N_{\rm Yb}$ when the condensation temperature T_C is achieved. By this stage of the cooling the volume of the Li Fermi gas (constrained by Fermi degeneracy) is larger than that of the coolant Yb bosons. The reduction in size and heat capacity of the coolant, and the differential gravitational sag are all effects which can reduce the sympathetic cooling efficiency [14]. Further, we might expect a reduction in condensate number in the presence of Li, due to collisions between energetic Li atoms near the Fermi velocity $v_F \simeq 5$ cm/s and the Yb BEC (peak condensate speed of sound $v_c \simeq 1$ mm/s), which may explain the condensate number reduction reported in [20].

In spite of the aforementioned issues, sympathetic cooling can produce deeply degenerate Fermi gases in our apparatus. By sacrificing all of the coolant Yb through evaporation, temperatures below $0.1T_F$ can be achieved [Fig. 5(c)]. By keeping a small amount of Yb in the trap, we establish a system in which Yb may act as an impurity probe of the ^{6}Li degenerate Fermi gas.

C. Yb-Li mixtures in strongly interacting regimes

Two different regimes of strong interactions in the Yb-Li system are of current scientific interest. The first one is a three-component system of Yb and two resonantly interacting Li spin states, a regime recently explored experimentally by Khramov *et al.* [21]. Here studies of strongly interacting Fermi gases using Yb as a dissipative bath or an impurity probe may be carried out. While the strong interactions induce inelastic loss processes at unitarity, which are unobservable in the weakly interacting regime, the interspecies elastic processes still dominate and we have observed temperatures as low as $0.25T_F$.

The other strongly interacting regime of current interest is a Feshbach resonance between Yb and Li atoms. Theoretical calculations by Brue and Hutson [22], predict narrow magnetically induced Feshbach resonances between ^{173}Yb and ^{6}Li. These have not yet been experimentally observed.

A fundamental limiting factor in preserving interspecies contact in degenerate Yb-Li mixtures is the differential gravitational sag of the two species at low trap depths. In our trap, the Yb atoms, due to their greater mass and weaker optical confinement, become significantly displaced from the Li atoms at temperatures near 300 nK, compromising the efficiency of sympathetic cooling and generally the study of any interspecies interaction effects. A technique for circumventing this limitation is discussed in the following section.

V. CONTROL OF INTERSPECIES SPATIAL OVERLAP

Differences in internal properties between components of an ultracold mixture can result in a differential response to external fields. This sometimes leads to unwanted effects such as the differential vertical displacement due to gravity experienced in mixtures with unequal mass constituents. For the weak optical potentials needed to achieve the highest phase-space densities, this "gravitational sag" leads to reduced spatial overlap and reduced interspecies interactions. The differential gravitational sag is an important limiting factor for the molecule formation efficiency in the K-Rb mixture [23], where the mass ratio is 2.2. In the case of the Yb-Li mixture, where the mass ratio is 29, this effect is even more significant, leading to a nearly complete decoupling of the two species at the lowest temperatures [14]. Here we demonstrate that this differential gravitational sag can be mitigated by the use of a magnetic field gradient which exerts a force on only the lithium component.

In principle, one may use external magnetic fields to achieve independent control of any two atomic species. For instance, in alkali-metal atoms with half-integer nuclear spin there will exist states with magnetic projection $m_F = 0$ in the direction of the magnetic field, allowing one species to be made insensitive to magnetic gradients. However, this insensitivity does not extend to the high magnetic fields often required in experiments (e.g., to address Feshbach resonances) due to hyperfine decoupling. Furthermore, mixtures of high-field- and low-field-seeking atoms are prone to inelastic, internal state-changing collisions, which lead to trap losses.

Mixtures of alkali-metal and alkaline-earth-metal atoms avoid these limitations as the ground-state magnetic moment of the alkaline-earth-metal species is zero or nearly zero for all external fields. Furthermore, in isotopes with zero nuclear moment, spin-exchange collisions are suppressed entirely. This feature has been used to overlap clouds of magnetically trapped rubidium atoms with optically trapped ytterbium atoms [24]. Here we report on manipulating the relative displacement of two species that are confined in the same optical trapping potential, and over a large temperature range down to <1 μK.

When atoms in a trap are subjected to a uniform force $F = mg$, the center of mass is displaced by an amount $\Delta z = g/\omega^2$, where ω is the vertical trapping frequency. Due to differences in mass and polarizability, the trap frequencies for Li and Yb differ by a factor of 8, leading to substantial differential gravitational sag at low trap depths.

We demonstrate control of interspecies spatial overlap by applying a magnetic gradient which acts as a "pseudogravitational" force on Li only. We first prepare a mixture of ^{6}Li in its two lowest-energy states and the single ground state of ^{174}Yb at a particular optical trap depth. For experimental simplicity, we ramp the bias field to 530 G, where the two Li spin states have equal magnetic moments $1\mu_B$ and negligible interaction strength. We then turn on our MOT coils to add a magnetic quadrupole field to the vertical bias field, thereby creating a magnetic force in the direction of the bias field. Our system is capable of producing vertical gradients up to 170 G/cm; however, a more modest gradient of 65 G/cm is sufficient to make the atom clouds concentric.

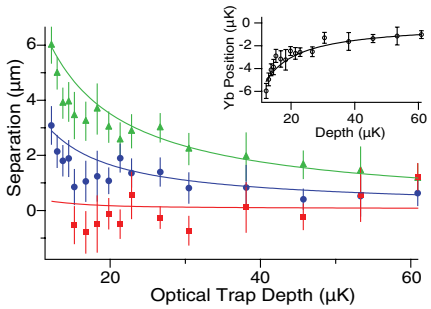

FIG. 6. (Color online) Relative displacement of centers of mass of Li and Yb clouds, versus optical trap depth for Yb atoms, at various magnetic gradients: -13 G/cm (filled triangles), 35 G/cm (filled circles), and 64 G/cm (filled squares). Each data point gives the average center-of-mass position of between 7 and 12 absorption images of lithium, subtracted from the average of 11 ytterbium images. The inset shows the displacement of Yb from the ODT beam center. The solid lines are results of a numerical model.

Figure 6 shows the separation of the cloud centers as a function of optical potential for different magnetic gradients. The gradient strength was determined by releasing the Li atoms and imaging them after a variable time to measure the acceleration $\mu_B B'/m_{\mathrm{Li}} + g$. The analysis also identified and corrected for slight ($<1^\circ$) deviations of the long trap axis from horizontal and the magnetic bias from vertical.

The lowest Yb optical trap depth for the data in Fig. 6 is 12 μK. Due to gravity, this corresponds to an effective trap depth of 4 μK, which goes to zero at an optical trap depth of 6 μK. We observe the onset of BEC at 15 μK optical depth when loading Yb alone.

At the lowest depths, the in-trap $1/e$ height of the ytterbium cloud is approximately 2 μm, whereas the Li cloud size is near the Fermi radius of 6 μm. Thus, in the absence of a magnetic gradient, the spatial overlap of the two clouds is critically reduced at trap depths below 20 μK.

Also shown in Fig. 6 is a set of theoretical curves of relative displacement, derived from a simple numerical model assuming a Gaussian trap profile. The only variable parameter in the model is the ODT (vertical) beam waist, which agrees at the 10% level with measurements of trap frequency via parametric excitation. We find reasonably good agreement between this model and the experimental data, although the calculation slightly overestimates the degree of sag at the lowest trap depths. One plausible explanation for this is a small vertical misalignment of the ODT beams, leading to a deviation from a Gaussian profile.

A side effect of this technique is that the applied gradient, while shifting the center of the trap, also effectively lowers the trap depth. Thus, for deeply degenerate Fermi clouds where the initial trap depth is close to the Fermi temperature, the "tilted" potential leads to spilling of Li atoms near the Fermi energy. This effect appears as a gradient-dependent Li number loss at

the lowest depths (when $T \lesssim 0.1T_F$) in our experiment and has been utilized elsewhere to measure interaction strength in Fermi gases [25] and to accelerate evaporative cooling in Bose gases [26].

We also note that the field inhomogeneity introduced by the magnetic gradient can limit its usefulness in experiments that require extremely homogeneous magnetic fields. For instance, a gradient of 65 G/cm corresponds to a magnetic field variation of tens of milligauss across the sample, much larger than the theoretical width of the predicted magnetic Feshbach resonances between ^{173}Yb and ^{6}Li [22].

Species-selective control of atomic samples has also been demonstrated using only optical fields. Bichromatic optical traps exploiting the different ac Stark shifts of atoms have been demonstrated [24]. Our technique has the advantage of requiring no additional lasers or sensitive alignment of optics. The effect is achieved entirely with existing hardware, operating under typical conditions.

In addition to the application described above, the magnetic gradient technique enables experiments involving the use of one atomic species as a local probe of the other. In the ^{6}Li-^{174}Yb system, the Yb acts as a "bath" at temperatures above degeneracy, where its cloud is much larger than that of Li. At low temperatures, Yb can act as a "probe," since the Yb cloud is much smaller than the Li Fermi radius [21]. Under the latter conditions, Yb can be a useful probe for studying the local properties of a Fermi gas in the weakly interacting as well as in the superfluid regime.

Beyond spatial control, one can also use magnetic gradients to achieve selective control of the momentum of the magnetically sensitive species, by changing the gradient nonadiabatically. Such velocity-control techniques may be useful for a range of studies, such as measures of viscosity and tests of superfluidity.

VI. CONCLUSIONS AND OUTLOOK

We have presented a detailed description of our apparatus to produce stable quantum mixtures of lithium and ytterbium atoms. We have also demonstrated a method of controlling the spatial overlap of the two species, general to combinations of magnetic and nonmagnetic atoms. When prepared near the ^{6}Li Feshbach resonance, bosonic Yb can act as a microscopic probe of the strongly interacting lithium Fermi gas. Other future applications of the mixture include the study of condensed matter models in an optical lattice, such as the binary-alloy model.

An interspecies Feshbach resonance between lithium and ytterbium will allow the exploration of three-body Efimov states with large mass mismatch, and potential studies of the many-body physics of mass-imbalanced pairs. While such resonances have not yet been observed, they may show up in the near future in experiments with the ground-state mixture, or by using Yb in an excited metastable state (such as $^{3}P_2$) [27]. An additional possibility is an interspecies optical Feshbach resonance [28]. Finally, the quantum-degenerate mixture of lithium and ytterbium provides the starting point for the production of quantum gases of paramagnetic polar molecules of YbLi. Such ultracold molecules are of general interest from the perspective of quantum simulation [5], quantum information [29], tests of fundamental symmetries [30], and probes of time variations of physical constants [31].

ACKNOWLEDGMENTS

We thank Lee Willcockson and Ryan Weh for major technical contributions during the early stages of the experiment. This work was supported by the National Science Foundation, the Air Force Office of Scientific Research, the Alfred P. Sloan Foundation, the UW Royalty Research Fund, and NIST.

[1] L. D. Carr, D. DeMille, R. V. Krems, and J. Ye, New J. Phys. **11**, 055049 (2009).
[2] Z. Hadzibabic, C. A. Stan, K. Dieckmann, S. Gupta, M. W. Zwierlein, A. Görlitz, and W. Ketterle, Phys. Rev. Lett. **88**, 160401 (2002).
[3] C. Kohstall, M. Zaccanti, M. Jag, A. Trenkwalder, P. Massignan, G. M. Bruun, F. Schreck, and R. Grimm, Nature (London) **485**, 615 (2012).
[4] K.-K. Ni, S. Ospelkaus, M. H. G. de Miranda, A. Peer, B. Neyenhuis, J. J. Zirbel, S. Kotochigova, P. S. Julienne, D. S. Jin, and J. Ye, Science **322**, 231 (2008).
[5] A. Micheli, G. K. Brennen, and P. Zoller, Nat. Phys. **2**, 341 (2006).
[6] E. Braaten and H. W. Hammer, Phys. Rep. **428**, 259 (2006).
[7] C. Ates and K. Ziegler, Phys. Rev. A **71**, 063610 (2005).
[8] M. M. Maska, R. Lemanski, J. K. Freericks, and C. J. Williams, Phys. Rev. Lett. **101**, 060404 (2008).
[9] M. M. Maska, R. Lemanski, C. J. Williams, and J. K. Freericks, Phys. Rev. A **83**, 063631 (2011).
[10] C. A. Stan and W. Ketterle, Rev. Sci. Instrum. **76**, 063113 (2005).
[11] H. J. Metcalf and P. Van der Straten, *Laser Cooling and Trapping* (Springer, Berlin, 1999).
[12] V. V. Ivanov, A. Khramov, A. H. Hansen, W. H. Dowd, F. Münchow, A. O. Jamison, and S. Gupta, Phys. Rev. Lett. **106**, 153201 (2011).
[13] At the highest laser powers (>50 W), however, we have observed thermal lensing effects in various optical components in the ODT path.
[14] A. H. Hansen, A. Khramov, W. H. Dowd, A. O. Jamison, V. V. Ivanov, and S. Gupta, Phys. Rev. A **84**, 011606(R) (2011).
[15] A. Mosk, S. Kraft, M. Mudrich, K. Singer, W. Wohlleben, R. Grimm, and M. Weidemüller, Appl. Phys. B: Lasers Opt. **73**, 791 (2001).
[16] Three-body losses may then be the dominant loss mechanism, as in the ^{174}Yb-^{87}Rb mixture [17].
[17] F. Baumer, F. Münchow, A. Görlitz, S. E. Maxwell, P. S. Julienne, and E. Tiesinga, Phys. Rev. A **83**, 040702(R) (2011).
[18] K. Henderson, C. Ryu, C. MacCormick, and M. Boshier, New J. Phys. **11**, 043030 (2009).
[19] A. O. Jamison, J. N. Kutz, and S. Gupta, Phys. Rev. A **84**, 043643 (2011).

[20] H. Hara, Y. Takasu, Y. Yamaoka, J. M. Doyle, and Y. Takahashi, Phys. Rev. Lett. **106**, 205304 (2011).
[21] A. Y. Khramov, A. H. Hansen, A. O. Jamison, W. H. Dowd, and S. Gupta, Phys. Rev. A **86**, 032705 (2012).
[22] D. A. Brue and J. M. Hutson, Phys. Rev. Lett. **108**, 043201 (2012).
[23] J. J. Zirbel, K.-K. Ni, S. Ospelkaus, J. P. D'Incao, C. E. Wieman, J. Ye, and D. S. Jin, Phys. Rev. Lett. **100**, 143201 (2008).
[24] S. Tassy, N. Nemitz, F. Baumer, C. Höhl, A. Batar, and A. Görlitz, J. Phys. B **43**, 205309 (2010).
[25] S. Jochim, M. Barternstein, A. Altmeyer, G. Hendl, S. Riedl, C. Chin, J. Hecker Deschlag, and R. Grimm, Science **302**, 2101 (2003).
[26] C.-L. Hung, X. Zhang, N. Gemelke, and C. Chin, Phys. Rev. A **78**, 011604(R) (2008).
[27] S. Kato, S. Sugawa, K. Shibata, R. Yamamoto, and Y. Takahashi, arXiv:1210.2483.
[28] S. Blatt, T. L. Nicholson, B. J. Bloom, J. R. Williams, J. W. Thomsen, P. S. Julienne, and J. Ye, Phys. Rev. Lett. **107**, 073202 (2011).
[29] D. DeMille, Phys. Rev. Lett. **88**, 067901 (2002).
[30] J. J. Hudson, D. M. Kara, I. J. Smallman, B. E. Sauer, M. R. Tarbutt, and E. A. Hinds, Nature (London) **473**, 493 (2011).
[31] M. Kajita, G. Gopakumar, M. Abe, and M. Hada, Phys. Rev. A **84**, 022507 (2011).

Appendix B

ULTRACOLD HETERONUCLEAR MIXTURE OF GROUND AND EXCITED STATE ATOMS

Ultracold Heteronuclear Mixture of Ground and Excited State Atoms

Alexander Khramov,[1] Anders Hansen,[1] William Dowd,[1] Richard J. Roy,[1] Constantinos Makrides,[2] Alexander Petrov,[2,3] Svetlana Kotochigova,[2] and Subhadeep Gupta[1]
[1]*Department of Physics, University of Washington, Seattle, Washington 98195, USA*
[2]*Department of Physics, Temple University, Philadelphia, Pennsylvania 19122, USA*
[3]*St. Petersburg Nuclear Physics Institute, Gatchina 188300, Russia, and Division of Quantum Mechanics, St. Petersburg State University, St. Petersburg 198904, Russia*
(Received 29 September 2013; published 23 January 2014)

We report on the realization of an ultracold mixture of lithium atoms in the ground state and ytterbium atoms in an excited metastable ($^3P_2$) state. Such a mixture can support broad magnetic Feshbach resonances which may be utilized for the production of ultracold molecules with an electronic spin degree of freedom, as well as novel Efimov trimers. We investigate the interaction properties of the mixture in the presence of an external magnetic field and find an upper limit for the background interspecies two-body inelastic decay coefficient of $K_2' < 3 \times 10^{-12}$ cm^3/s for the $^3P_2$ $m_J = -1$ substate. We calculate the dynamic polarizabilities of the Yb($^3P_2$) magnetic substates for a range of wavelengths, and find good agreement with our measurements at 1064 nm. Our calculations also allow the identification of magic frequencies where Yb ground and metastable states are identically trapped and the determination of the interspecies van der Waals coefficients.

DOI: 10.1103/PhysRevLett.112.033201 PACS numbers: 34.20.Cf, 32.10.Dk, 34.50.Cx, 37.10.De

Ultracold elemental mixtures provide unique opportunities to study few- and many-body physics with mass-mismatched atomic partners [1] and diatomic polar molecules [2,3]. While the bulk of elemental mixture experiments have been performed using ground state bialkali systems, the recent production of ground state mixtures of alkali-metal- and alkaline-earth-metal-like atoms [4–7] further extends the experimental possibilities. These include powerful quantum simulation and information protocols [8] and tests of fundamental symmetries [9] with paramagnetic polar molecules. While tunable two-body interactions that are important for these advances have been proposed in such mixtures [10], they have not yet been experimentally detected.

In this Letter we report the realization of a new class of heteronuclear mixtures in which one atomic component is in an electronically excited state, using lithium (^{6}Li) and ytterbium (^{174}Yb) atoms. This establishes a highly mass-mismatched atomic mixture where tunable anisotropic interactions are expected to play a strong role [11], laying a foundation for future studies of ultracold trapped paramagnetic polar molecules and Efimov trimers with very large mass imbalance [12]. We measure inelastic interactions in the mixture and observe the relative suppression of interspecies inelastic processes. Our experimental methods also demonstrate new techniques of production and manipulation of spin components in the metastable $^3P_2$ state of Yb.

The study and control of anisotropic interactions is an increasingly important topic in ultracold atomic systems. In addition to their impact on many-body physics [3,8,13], anisotropic two-body interactions are proving to be of great interest for generating magnetically tunable interactions, as has been calculated theoretically [14] and observed experimentally in a mixture of ground and excited state Yb atoms [15]. The latter result applied in the context of the Li + Yb combination points to an alternative route towards tunable interactions, where the ground state Feshbach resonances are predicted to be extremely narrow [16] and experimentally difficult to access.

An important component of the work reported here is the successful trapping of Yb atoms in the $^3P_2$ state (Yb*) in a 1064 nm optical dipole trap (ODT), where Li atoms can be cotrapped. Our scheme for preparation and detection of Yb* is similar to an earlier one that was used to populate a spin mixture of Yb* in a 532 nm ODT [17] but is modified to produce pure spin states in a 1064 nm trap at an arbitrary external magnetic field. We confine ground state ^{174}Yb atoms in a horizontally oriented single-beam ODT and evaporatively cool them to the microkelvin regime. We then produce the Yb* state by optical pumping (see Fig. 1) using the $^1S_0 \rightarrow {}^3D_2$ electric quadrupole transition at 404 nm [18]. With this setup [19], we can achieve a $^1S_0 \rightarrow {}^3P_2$ pumping rate of up to 50 Hz per atom. Remaining ground state atoms are removed with 399 nm light. Yb* atoms are detected by transferring them back to the ground $^1S_0$ state using light at 770/649 nm immediately prior to absorption imaging on the 399 nm transition. Further details can be found in the Supplemental Material [19].

Our method of preparing pure spin states of Yb* takes advantage of dipole selection rules and differential Stark shifts between spin states. By using an external magnetic

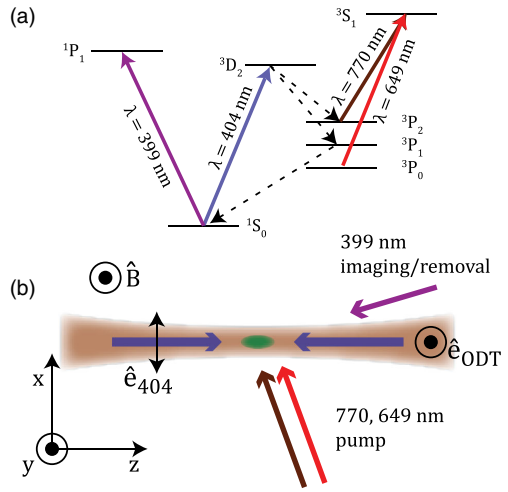

FIG. 1 (color online). Yb* preparation and detection scheme. (a) Low-lying energy levels of ytterbium with solid (dashed) lines indicating the relevant laser excitation (spontaneous decay) processes. The natural linewidths of the short-lived $\{^1P_1, ^3P_1, ^3D_2, ^3S_1\}$ excited states are $2\pi \times \{28, 0.18, 0.35, 12\}$ MHz, respectively. (b) Top-down view of experimental setup. Two counterpropagating 404 nm excitation beams (blue arrows) are overlapped with the ODT (brown). Laser beams at 649 and 770 nm (red, brown arrows) pump atoms back to the ground state prior to absorption imaging using the 399 nm beam (purple arrow).

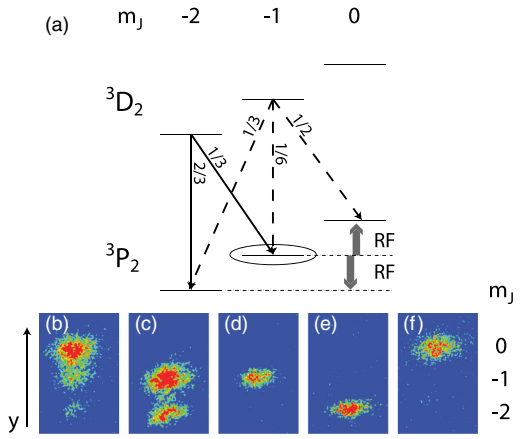

FIG. 2 (color online). Yb*state preparation. (a) A particular magnetic substate of $^3D_2$ can be resolved via Zeeman splitting and selectively excited with 404 nm light. This state will subsequently spontaneously decay to substates in the $^3P_2$ manifold according to the indicated branching ratios. Radio frequency transitions within the $^3P_2$ manifold are spectroscopically resolved due to the state-dependent Stark shifts in the 1064 nm ODT. (b)–(f) Absorption images of different $^3P_2$ spin compositions after Stern-Gerlach separation. The images correspond to (b) transfer via the $^3D_2$ $m_J = -1$ substate; (c) transfer via the $^3D_2$ $m_J = -2$ substate; (d) transfer via $^3D_2$ $m_J = -2$ substate with an applied in-trap gradient to obtain a pure sample of $^3P_2$ $m_J = -1$ atoms; (e) and (f) are the same as (d), followed by rf π-pulse transfer to $m_J = -2$ and $m_J = 0$, respectively, of the $^3P_2$ manifold. The rf pulses in (e) and (f) are 300 μs long with frequencies close to the Zeeman splitting of 26 MHz but separated by 430 kHz due to the state-dependent Stark shift.

field, we spectrally resolve magnetic substates within the $^3D_2$ manifold, from which the atoms decay into $^3P_2$ [see Fig. 2(a)]. The resultant population in a particular spin state of $^3P_2$ is determined by a combination of the branching ratio for spontaneous emission into that state and potential atom loss due to a trap depth reduction from the state dependent polarizability. We determine the spin composition of our trapped Yb* samples using the Stern-Gerlach technique to spatially separate the states during expansion from the trap [see Figs. 2(b)–2(f)]. The initial composition of atoms trapped in $^3P_2$ from an excitation to the $^3D_2$ $m_J = -1(-2)$ state is shown in panel b (c) of Fig. 2. For our trap, the $^3P_2$ $m_J = -2$ is very weakly trapped compared to the $^3P_2$ $m_J = -1$ state, leading to a substantial, ODT beam power-dependent loss of $m_J = -2$ atoms due to gravitational spilling. By reducing ODT power and applying a vertical magnetic gradient field during the 404 nm exposure, we can make this state untrapped. We thus obtain a pure sample of $m_J = -1$ Yb* atoms [Fig. 2(d)]. By applying a transverse radiofrequency (rf) magnetic field, we can drive transitions to other m_J states of Yb*. Taking advantage of the spectroscopic resolution created by the differential Stark shift of neighboring states, we obtain pure samples of either $m_J = -2$ or 0 using rf π pulses [Figs. 2(e) and 2(f)] [20].

The relevant property for controlling a particular atomic state in an optical trap is its dynamic polarizability $\alpha(\omega, \vec{\epsilon})$, a function of radiation frequency ω and polarization $\vec{\epsilon}$. The polarizability of each of the $^1S_0$ ground and $^3P_2$ metastable states of Yb is determined by the dipole couplings to all other atomic states [21]. We calculate the polarizability from a combination of experimental transition frequencies and oscillator strengths between atomic levels available from the literature [22] and additional theoretical calculations of these characteristics for other transitions using a relativistic multiconfiguration Dirac-Fock-Sturm method, described in [23]. Figure 3 shows the resulting polarizability as a function of laser frequency of light linearly polarized parallel to the quantization axis for ground state Yb and the five magnetic sublevels $m_J = 0, \pm 1$, and ± 2 of Yb*. The polarizability is singular at atomic transition energies and strongly depends on the absolute value of m_J. In fact, it has opposite signs for different m_J over significant ranges of frequencies. The intersections of ground and excited state curves in Fig. 3 indicate magic wavelengths for ultranarrow optical transitions. We find good agreement with earlier measurements at

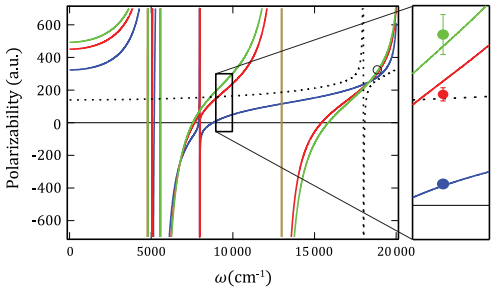

FIG. 3 (color online). Calculated dynamic polarizability of Yb* as a function of frequency of light polarized parallel to the quantization axis. Green, red, and blue solid lines correspond to the $|m_J| = 0$, 1, and 2 substates, respectively, and the dashed line to the ground state. The open circle indicates measurements of the ac polarizability at 532 nm [24]. Our polarizability ratio measurements at 1064 nm, scaled to the calculated $^1S_0$ value, are shown as solid circles in inset.

532 nm [24]. The transition frequencies and oscillator strengths used in calculating the dynamic polarizability also enable us to construct both relativistic and nonrelativistic van der Waals C_6 coefficients for the Yb* + Yb* and Yb* + Li collision systems. A more detailed description of this procedure is given in the Supplemental Material [19]. From these we determine the p-wave threshold for two-body collisions in the above systems to be 24 μK and 2.1 mK, respectively.

We experimentally determine polarizabilities at 1064 nm to compare to our calculated values. We measure the trap frequencies of the $m_J = 0, -1$, and -2 substates and compare to an identical measurement for the ground $^1S_0$ state. The trap frequencies were measured by observing the oscillation of cloud size (breathing mode) following a diabatic increase in trap depth. These values were also verified by using the parametric excitation technique. The experimentally obtained polarizability ratios are $\alpha_{-1}/\alpha_g = 1.04(6)$, $\alpha_0/\alpha_g = 1.6(2)$, and $\alpha_{-2}/\alpha_g = 0.20(2)$. These agree well with our theoretically calculated ratios (see inset of Fig. 3).

With the facility to produce, manipulate, and detect Yb* added to our Li-Yb apparatus [5,25], we investigate the mixture of Yb* and Li. Here, we focus on a mixture of the lowest hyperfine state of ^{6}Li (denoted $|1\rangle$) and the $m_J = -1$ state of Yb*. Starting with an optically trapped and cooled mixture of ^{174}Yb ($^1S_0$) and ^{6}Li ($|1\rangle$), we change the magnetic field to a desired value and prepare the $m_J = -1$ state of Yb* as discussed above [19]. We subsequently compress the trap in order to suppress atom loss due to evaporation and to improve interspecies spatial overlap against differential gravitational sag. Further details can be found in the Supplemental Material [19].

The number and temperature evolution of an Yb* + Li mixture prepared in this way at an external magnetic field of 12 G is shown in Fig. 4. The initial temperature difference between the species is due to thermal decoupling at the lowest trap depths [5,19] and is a useful starting point to monitor elastic interspecies interactions. One-body effects from Yb* spontaneous decay, from collisions with background atoms, and from off-resonant scattering of ODT photons are negligible on the time scale of the experiment. Since our lithium component is a single state fermion deep in the s-wave regime [26], the Li-Li interactions are negligible for our parameters. From our calculated values for the p-wave threshold for two-body collisions in the Yb* + Yb* and Yb* + Li systems, we infer that all two-body interactions are s-wave dominated. For the starting peak density of $n_{Yb^*(Li)} = 5.3(1.2) \times 10^{12}$ cm^{-3} and large evaporation parameter $\eta_{Yb^*(Li)} = U_{Yb^*(Li)}/k_B T_{Yb^*(Li)} = 24(20)$, it is reasonable to expect that all number losses result from two-body inelastic processes. Here U and T are the trap depths and temperatures of the two species, respectively. We observe that the system retains its initial temperature disparity throughout the time scale of the experiment. This suggests that interspecies s-wave elastic collisions play a negligible part in the system dynamics.

A striking feature of Fig. 4 is the stability of the Li number on the time scale of Yb* decay, suggesting a dominance of inelastic effects from Yb* + Yb* collisions over Li + Yb* collisions. We model the atomic densities with the coupled differential equations

$$\dot{n}_{Yb^*} = -K_2' n_{Li} n_{Yb^*} - K_2 n_{Yb^*}^2,$$

$$\dot{n}_{Li} = -K_2' n_{Li} n_{Yb^*},$$

where $n_{Yb^*(Li)}$ and $K_2(K_2')$ are the densities of Yb*(Li) and the (volume-independent) two-body decay coefficients of

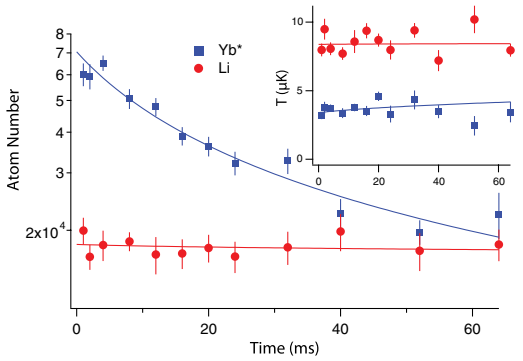

FIG. 4 (color online). Number and temperature (inset) evolution of Yb* and Li in the ODT at an external magnetic field of 12 G. Lines show fits based on a model including two-body inelastic effects (see text).

Yb^*-Yb^* (Yb^*-Li). The temperature evolution is given by the heating from the density dependence of the inelastic processes which favor atom loss from near the trap center [27]. Best fits with this model (solid lines in Fig. 4) yield $K_2 = 2.5 \times 10^{-11}$ cm^3/s, and K_2' consistent with zero [28]. The estimated statistical error provides an upper bound of $K_2' < 3 \times 10^{-12}$ cm^3/s. By considering the elastic cross section needed for interspecies thermalization on the experimental time scale, we can also place an upper bound of $300a_0$ on the magnitude of the interspecies s-wave scattering length. Here a_0 is the Bohr radius.

Our study of interspecies interactions can be extended to arbitrary values of the external magnetic field and also to different magnetic substates of Yb^* using the methods described above. Repeating the above experiment at 94 G we observe a similarly long lifetime of Li atoms in the presence of Yb^*. These low values of background interspecies inelastic rates bode well for future searches for Feshbach resonances between spin-polarized samples of Yb^* and Li, where interspecies inelastic rates should be resonantly enhanced and could be observed by monitoring the Li population as a function of magnetic field. By working in an optical lattice and/or using a fermionic Yb isotope, the inelastic effects of $Yb^* + Yb^*$ collisions may be suppressed, allowing for a more precise investigation of interspecies phenomena in the mixture. We note that complementary theoretical work has already been initiated [11,29].

In conclusion, we produced spin polarized samples of ytterbium atoms in the $^3P_2$ (Yb^*) state in a 1064 nm ODT. Our demonstrated method to manipulate the spin state of Yb^* is extendable to production of arbitrary spin superpositions within the $^3P_2$ manifold and could be applicable towards quantum information schemes reliant on the long-range magnetic dipole-dipole interaction [30]. We measured the dynamic polarizabilities of different spin substates and found good agreement with our calculated theoretical values. These calculations also identify magic wavelength points, of relevance for potential optical clock transitions between ground and long-lived metastable ($^3P_2$) states of Yb [31,32]. We cotrapped lithium with metastable ytterbium and investigated the interaction properties of the mixture at large magnetic fields. We found a dominance of intraspecies inelastic effects over interspecies ones. Possible applications of this mixture include investigations of universal few-body physics [12], and the synthesis of ultracold paramagnetic polar molecules for quantum simulation [8] and tests of fundamental symmetries [9].

We thank J. M. Hutson, P. S. Julienne, and Y. Takahashi for useful discussions, and A. O. Jamison for valuable technical contributions and discussions. We gratefully acknowledge funding from NSF Grants No. PHY-1308573, No. PHY-0847776, No. PHY-1306647, AFOSR Grants No. FA9550-11-1-0243, No. FA9550-12-10051, and ARO MURI Grant No. W911NF-12-1-0476.

Note added.—Recently, related work was reported in which the polarizabilities of Yb^* substates were determined at 1070 nm using optical spectroscopy [34].

[1] C. Kohstall, M. Zaccanti, M. Jag, A. Trenkwalder, P. Massignan, G. Bruun, F. Schreck, and R. Grimm, Nature (London) **485**, 615 (2012).
[2] K.-K. Ni, S. Ospelkaus, D. Wang, G. Quemener, B. Neyenhuis, M. H. G. de Miranda, J. Bohn, J. Ye, and D. Jin, Nature (London) **464**, 1324 (2010).
[3] B. Yan, S. A. Moses, B. Gadway, J. P. Covey, K. R. A. Hazzard, A. M. Rey, D. S. Jin, and J. Ye, Nature (London) **501**, 521 (2013).
[4] N. Nemitz, F. Baumer, F. Münchow, S. Tassy, and A. Görlitz, Phys. Rev. A **79**, 061403(R) (2009).
[5] V. V. Ivanov, A. Khramov, A. H. Hansen, W. H. Dowd, F. Münchow, A. O. Jamison, and S. Gupta, Phys. Rev. Lett. **106**, 153201 (2011).
[6] H. Hara, Y. Takasu, Y. Yamaoka, J. M. Doyle, and Y. Takahashi, Phys. Rev. Lett. **106**, 205304 (2011).
[7] B. Pasquiou, A. Bayerle, S. M. Tzanova, S. Stellmer, J. Szczepkowski, M. Parigger, R. Grimm, and F. Schreck, Phys. Rev. A **88**, 023601 (2013).
[8] A. Micheli, G. K. Brennen, and P. Zoller, Nat. Phys. **2**, 341 (2006).
[9] J. J. Hudson, D. M. Kara, I. J. Smallman, B. E. Sauer, M. R. Tarbutt, and E. A. Hinds, Nature (London) **473**, 493 (2011).
[10] P. S. Zuchowski, J. Aldegunde, and J. M. Hutson, Phys. Rev. Lett. **105**, 153201 (2010).
[11] M. L. Gonzalez-Martinez and J. M. Hutson, Phys. Rev. A **88**, 020701(R) (2013).
[12] E. Braaten and H. W. Hammer, Phys. Rep. **428**, 259 (2006).
[13] T. Lahaye, C. Menotti, L. Santos, M. Lewenstein, and T. Pfau, Rep. Prog. Phys. **72**, 126401 (2009).
[14] A. Petrov, E. Tiesinga, and S. Kotochigova, Phys. Rev. Lett. **109**, 103002 (2012).
[15] S. Kato, S. Sugawa, K. Shibata, R. Yamamoto, and Y. Takahashi, Phys. Rev. Lett. **110**, 173201 (2013).
[16] D. A. Brue and J. M. Hutson, Phys. Rev. Lett. **108**, 043201 (2012).
[17] A. Yamaguchi, S. Uetake, D. Hashimoto, J. M. Doyle, and Y. Takahashi, Phys. Rev. Lett. **101**, 233002 (2008).
[18] C. J. Bowers, D. Budker, S. J. Freedman, G. Gwinner, J. E. Stalnaker, and D. DeMille, Phys. Rev. A **59**, 3513 (1999).
[19] See Supplemental Material at http://link.aps.org/supplemental/10.1103/PhysRevLett.112.033201, which provides experimental details of $^3P_2$ state preparation and mixture preparation procedures, as well as details of the polarizability calculation and the derived C_6 coefficients.
[20] Another method to achieve pure spin states in Yb^* has been shown earlier [33], but relies on the availability of an ultranarrow laser.
[21] S. Kotochigova and E. Tiesinga, Phys. Rev. A **73**, 041405 (R) (2006).
[22] Y. Ralchenko, A. Kramida, and J. Reader, and NIST ASD Team, NIST Atomic Spectra Database (NIST, Gaithersburg, MD), http://physics.nist.gov/asd (retrieved 2011).

[23] S. Kotochigova, K. P. Kirby, and I. Tupitsyn, Phys. Rev. A **76**, 052513 (2007).
[24] A. Yamaguchi, S. Uetake, S. Kato, H. Ito, and Y. Takahashi, New J. Phys. **12**, 103001 (2010).
[25] A. H. Hansen, A. Y. Khramov, W. H. Dowd, A. O. Jamison, B. Plotkin-Swing, R. J. Roy, and S. Gupta, Phys. Rev. A **87**, 013615 (2013).
[26] Z.-C. Yan, J. F. Babb, A. Dalgarno, and G. W. F. Drake, Phys. Rev. A **54**, 2824 (1996).
[27] T. Weber, J. Herbig, M. Mark, H.-C. Nagerl, and R. Grimm, Phys. Rev. Lett. **91**, 123201 (2003).
[28] By fitting the Yb^* number according to $\dot{n}_{Yb^*} = -K_2 n_{Yb^*}^2$ at the average temperature of 3.6 μK, we obtain the value of $K_2 = 2.6 \times 10^{-11}$ cm^3/s.
[29] C. Makrides, A. Petrov, and S. Kotochigova (unpublished).
[30] A. Derevianko and C. C. Cannon, Phys. Rev. A **70**, 062319 (2004).
[31] J. Hall, M. Zhu, and P. Buch, J. Opt. Soc. Am. B **6**, 2194 (1989).
[32] N. D. Lemke, A. D. Ludlow, Z. W. Barber, T. M. Fortier, S. A. Diddams, Y. Jiang, S. R. Jefferts, T. P. Heavner, T. E. Parker, and C. W. Oates, Phys. Rev. Lett. **103**, 063001 (2009).
[33] S. Uetake, R. Murakami, J. M. Doyle, and Y. Takahashi, Phys. Rev. A **86**, 032712 (2012).
[34] H. Hara, H. Konishi, S. Nakajima, Y. Takasu, and Y. Takahashi, J. Phys. Soc. Jpn. **83**, 014003 (2014).

Appendix C

MAGNETIC FIELD DEPENDENT INTERACTIONS IN AN ULTRACOLD LI-YB($^3P_2$) MIXTURE

Magnetic field dependent interactions in an ultracold Li-Yb($^3P_2$) mixture

William Dowd,[1] Richard J. Roy,[1] Rajendra K. Shrestha,[1] Alexander Petrov,[2,*]
Constantinos Makrides,[2] Svetlana Kotochigova,[2] and Subhadeep Gupta[1]

[1] *Department of Physics, University of Washington, Seattle WA 98195, USA*
[2] *Department of Physics, Temple University, Philadelphia PA 19122, USA*

(Dated: December 19, 2014)

Magnetic Feshbach resonances have allowed great success in the production of ultracold diatomic molecules from bi-alkali mixtures, but have so far eluded observation in mixtures of alkali and alkaline-earth-like atoms. Inelastic collisional properties of ultracold atomic systems exhibit resonant behavior in the vicinity of such resonances, providing a detection signature. We study magnetic field dependent inelastic effects via atom loss spectroscopy in an ultracold heteronuclear mixture of alkali ^{6}Li in the ground state and alkaline-earth-like ^{174}Yb in an excited electronic metastable state ($^3P_2$, $m_J = -1$). We observe a variation of the interspecies inelastic two-body rate coefficient by nearly one order of magnitude over a $100 - 520$ G magnetic field range. By comparing to ab-initio calculations we link our observations to interspecies Feshbach resonances arising from anisotropic interactions in this novel collisional system.

I. INTRODUCTION

The ground electronic doublet-sigma ($^2\Sigma$) state of a diatomic molecule composed of an alkali and an alkaline-earth-like atom is endowed with an unpaired electron. This electronic degree of freedom distinguishes it from the spinless singlet-sigma ($^1\Sigma$) ground state of the bi-alkali molecules familiar to the ultracold gas community. In particular, it opens up new possibilities in the field of quantum simulation that exploit both electric and magnetic dipole moments [1], and provides new opportunities to test fundamental physical theories through, for instance, electron electric dipole moment measurements [2].

Magnetic Feshbach resonances[3–5] have been crucial in the production of ground-state bi-alkali molecules [6, 7], allowing for the transformation of free atoms into weakly-bound "Feshbach" molecules. These Feshbach molecules can then be transferred into the ground state using coherent two-photon processes. Current experimental efforts with ultracold mixtures of alkali and alkaline-earth-like atoms [8–11] now face the challenge of locating and utilizing suitable Feshbach resonances to create doublet-sigma molecules. Unfortunately, recent theoretical studies indicate that Feshbach resonances between the ground states of alkali and alkaline-earth-like atoms are extremely narrow and located at inconveniently high fields [12]. Such resonances have not yet been experimentally observed.

On the other hand, alkaline-earth-like atoms offer an additional avenue of collisional physics to explore due to the presence of long-lived (metastable) electronically excited ^3P states. Earlier studies of these metastable states in alkaline-earth atoms calcium and strontium [13, 14] and alkaline-earth-like ytterbium [15] revealed both elastic and inelastic collisional behavior. Resonances between ground and metastable ytterbium were recently reported[16] and attributed to anisotropy in the atomic interactions[17]. Our group recently realized a heteronuclear mixture of metastable ytterbium and alkali lithium [18], where broad interspecies Feshbach resonances of sev-

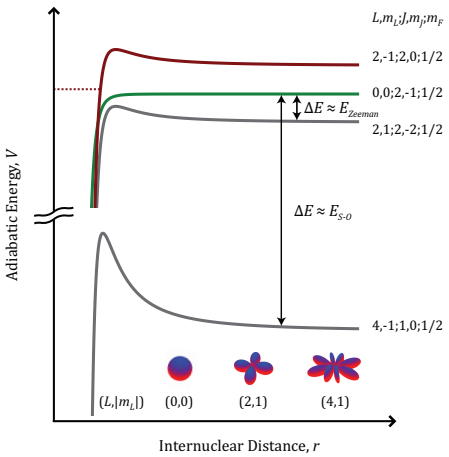

FIG. 1: (Color online). Schematic of Yb*+Li two-body collisions showing a subset of the various possible adiabatic potentials. All collision channels satisfying $m_{\rm Yb}+m_{\rm Li}+m_l = -1/2$ are allowed (see text). Anisotropy in the interspecies interaction can couple entrance and exit channels with different rotational angular momentum l (with Δl even). Potentials asymptoting to lower energy (grey) than the entrance channel (green) can lead to inelastic losses while those with higher energy can support Feshbach resonances via magnetic-field tunable bound states (red).

*Alternative address: St. Petersburg Nuclear Physics Institute, Gatchina, 188300; Division of Quantum Mechanics, St. Petersburg State University, 198904, Russia.

eral Gauss width are theoretically predicted [19]. Such resonances would be accompanied by peaks in the interspecies inelastic collision rate.

In this paper we report on the collisional properties of ^{174}Yb in the metastable $^3P_2(m_J = -1)$ state both with itself, and with ground state ^{6}Li over a wide range of magnetic fields. We observe nearly one order of magnitude variation in the interspecies inelastic two-body collision rate coefficient. We also perform ab-initio calculations for this collisional system which link our experimental observations to the different collision channels (see Fig. 1) and to the presence of anisotropy-induced interspecies Feshbach resonances.

II. PREPARATION OF THE ULTRACOLD LI-YB* MIXTURE

The experiment is performed in our mixture apparatus described in reference [20]. We sequentially load compressed magneto-optical traps of Yb and Li into a single beam 1064 nm optical dipole trap. Orthogonal to this main beam, we add a much weaker beam (1070 nm) which serves to increase the increase the axial confinement. After 4 s of forced evaporative cooling consisting of lowering the intensity of the main beam, and concurrent interspecies thermalization, we obtain a mixture with $500(25) \times 10^3$ Yb(Li) atoms at 1.1μK, with Yb in the ground $^1S_0$ state and Li in the ground $^2S_{1/2}$ state, spin-purified to the lowest energy Zeeman state ($|m_J, m_I\rangle = |-1/2, +1\rangle$ at high field).

We achieve spin-purified metastable ytterbium in the $^3P_2$, $m_J = -1$ state (Yb*) using the scheme detailed in prior work [18]. Briefly, we optically pump using the $^1S_0 \rightarrow {}^3D_2$ electric quadrupole transition at 404 nm[21] which decays to the $^3P_2$ state with a 12% branching ratio. The remaining fraction decays to $^3P_1$ which returns to $^1S_0$ with a $< 1\,\mu$s decay time and the cycle repeats. We use 1 mW of 404 nm light focused to 30 μm aligned along the long axis of our dipole trap. In 10 ms we achieve 25% transfer to the metastable state, populating the $m_J = -1$ and -2 sublevels. The $^3P_2$ substate polarizabilities are sensitive to the angle between the electric field of the trapping laser and the magnetic quantization axis. We exploit this effect to maximize (minimize) the trap depth for the $m_J = -1(-2)$ state by orienting the linear polarization of our optical trap parallel to the magnetic bias field (vertical in our case). Together with a 50 G/cm vertical magnetic field gradient applied against gravity, this spills the $m_J = -2$ atoms, resulting in a pure gas of Yb* atoms [22]. Any atoms remaining in the ground state are subsequently removed by a resonant laser pulse on the strong $^1S_0 \rightarrow {}^1P_1$ transition. At the end of the transfer process there are $2(1)\times10^4$ Yb*(Li) atoms at 1.7(1.5) μK with a peak density of $1.0(5.1) \times 10^{12}$/cm^3 for Yb*(Li).

The entire transfer process is done at a moderate field of 100 G which is a compromise between minimizing losses due to inelastics during the transfer process and ramp time to the largest magnetic fields. Once transfer is complete, we ramp the electromagnets at 50 G/ms to the desired field. Coincident with this, we lower the magnetic gradient to 20 G/cm, eliminating the effect of gravitational sag for the Yb* atoms and hence maximizing the spatial overlap with the Li atoms. We allow the gases to interact for up to 40 ms before imaging the remaining atoms.

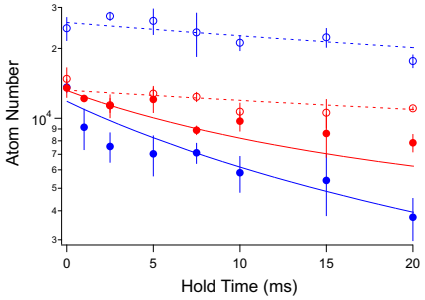

FIG. 2: (Color online). Sample lifetime curves of Yb*(blue) and Li(red) taken at 100 G (open circles) and 450 G (closed circles) are shown. Also shown are best fit curves (see text) for both 100 G (dashed) and 450 G (solid) datasets.

III. ANALYSIS OF FIELD-DEPENDENT INTERACTIONS

Since the temperature of the system is far below the p-wave threshold for the system [18], we consider only $l = 0$ rotational states in the entrance channel for collisions between $m_{\rm Yb} = m_{J,\rm Yb} = -1$ and $m_{\rm Li} = m_{J,\rm Li} + m_{I,\rm Li} = +1/2$ atoms. The electronic interaction between Yb* and Li conserves $m_{\rm Yb} + m_{\rm Li} + m_l = -1/2$ (see Fig. 1). We analyze the time evolution of our ultracold mixture at different magnetic fields B in terms of two field-dependent two-body inelastic parameters representing all Yb*-Yb* and all Yb*-Li inelastic collisions.

The time evolution of the atomic densities in our two-species mixture (Fig. 2) is fit according to the coupled differential equations

$$\dot{n}_{\rm Yb} = -K_2'(B) n_{\rm Yb} n_{\rm Li} - 2K_2(B) n_{\rm Yb}^2 \qquad (1)$$

$$\dot{n}_{\rm Li} = -K_2'(B) n_{\rm Yb} n_{\rm Li} \qquad (2)$$

where $n_{\rm Yb(Li)}$ is the Yb*(Li) density and $K_2(K_2')$ are the field dependent Yb*+Yb*(Yb*+Li) inelastic coefficients. Decay rates for single-body processes and for Li-Li interactions are negligible for this system [18] and are therefore excluded from this analysis. Three-body decay rates of the form $K_3 n_{\rm Yb}^3$ and $K_3' n_{\rm Yb}^2 n_{\rm Li}$ can also contribute to

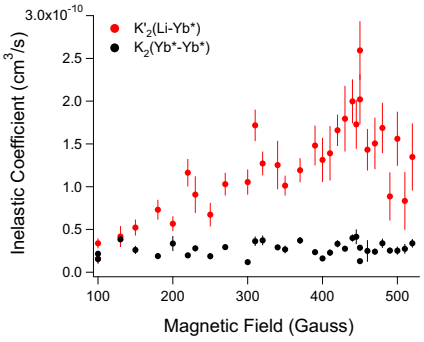

FIG. 3: (Color online). Spectra of inelastic decay coefficients as a function of magnetic field for Yb*+Yb* (black) and Yb*+Li (red).

system dynamics, but are expected to be much weaker given the relatively low densities involved.

The extracted inelastic coefficients depend sensitively on the spatial overlap of the gases, which is affected by temperatures, trap frequencies, and spatial offsets. The temperature itself is a dynamic quantity; atoms from the densest (and thus lowest energy) regions of the trap are preferentially removed, thus increasing the temperature. In addition, the excitation scheme preferentially heats the Yb* atoms from photon recoil. To guard against this, we measure the temperature dynamics of the two gases at several magnetic fields, and find that the temperature does not appreciably change over the short timescale of the experiment [23].

We pay careful attention to the spatial overlap of the two clouds during the evolution time, limiting our analysis to the duration within which the two species have not lost more than 10% overlap. This typically limits the datasets for analysis to the $0-20\,\mathrm{ms}$ regime [24].

At each magnetic field, we take a separate set of data with all Li atoms removed from the trap. This allows us to independently fit the K_2 parameter associated with Yb*+Yb* inelastic processes. This results in dramatically improved fits and uncertainties for the K_2' parameter.

The resulting spectrum of inelastic rates for $100-520\,\mathrm{G}$ is shown in Fig. 3. We find that the intra-species inelastic rate is much weaker than the inter-species rate. The intra-species coefficient $K_2(B)$ remains mostly constant throughout this range. The inter-species coefficient $K_2'(B)$, however, displays an overall growth with magnetic field from $100-450\,\mathrm{G}$ of about a factor of eight. Of particular note is the peak at $450\,\mathrm{G}$ which approaches the unitarity limit of $2.9\times10^{-10}\,\mathrm{cm}^3/\mathrm{s}$ [25] for two-body Li-Yb interactions at these temperatures.

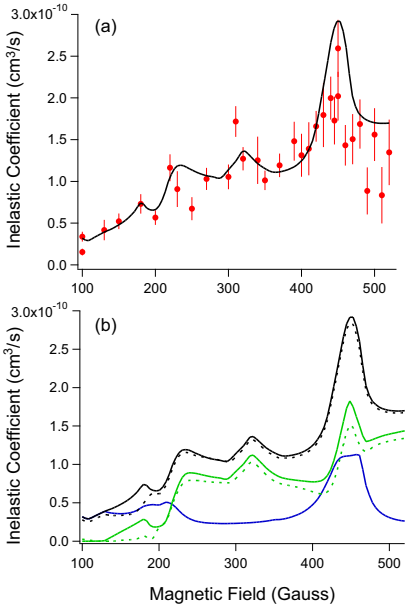

FIG. 4: (Color online). (a) shows the theoretical (solid black) curve with optimized short-range potentials (see text) for the inelastic loss rate coefficient between ^{6}Li and ^{174}Yb together with experimental data (red points). (b) Inelastic loss rate to the $^3P_2 m_J = -2$ (green) and $^3P_1$ (blue) channels together with the total loss rate (black). The dashed lines correspond to the same calculations performed without $l = 0$ channels.

IV. THEORETICAL MODEL

The collisional properties of the Li($^2S_{1/2}$)+Yb($^3P_2$) system are determined by (i) constructing the short-range and long-range electronic interaction potentials and (ii) performing a close coupling calculation that treats the hyperfine and Zeeman interaction, molecular rotation, magnetic dipole-dipole interaction, and the electronic interactions on equal footing. The four non-relativistic short-range potentials that dissociate to the ^3P limit are calculated using the configuration-interaction method. The details of this calculation are given in Ref. [26]. The long-range behavior of the potentials is constructed by adding the isotropic and anisotropic dispersion and magnetic dipole-dipole interactions, defined by the C_6 and C_3 parameters that were presented in our previous study [18] (Supplemental Material). By setting up a coupled-channels model for the collision between ground state Li and metastable Yb atoms we determine the existence and major characteristics of Feshbach resonances as a function of magnetic field B for a few of the lowest hyperfine and Zeeman sublevels. A de-

tailed account of the theoretical model of our collisional system can be found in [26]. We note that the agreement between our experimental and theoretical spectrum is only obtained after a study of the dependencies of the rate coefficient on the short-range shape of the $^{2,4}\Sigma^+$ and $^{2,4}\Pi$ electronic potentials. We cannot exclude the existence of other shapes of potentials that will lead to loss rates consistent with the experimental data.

The resultant inelastic scattering coefficient for fields between 100 Gauss and 520 Gauss is shown together with the experimental values in Fig. 4(a). We observe one clear resonance at 450 G, and some weak modulations at lower fields. These resonances have multi-channel dependence and cannot be characterized by a single partial wave, only converging to their final locations when collision channels up to $l = 8$ are included in the calculation (see Fig. 4(b)). Our bound-state calculation of the LiYb* molecule allows us to assign the 450 G feature as arising from a resonance with a bound state of 60% d-wave and 40% g-wave character. Other quantum labels for this resonance arise from the eigenstates of the atomic Zeeman plus hyperfine Hamiltonian [26] of ^{6}Li and ^{174}Yb, with $(m_J, m_I) = (1/2, -1)$ for lithium and $(J, m_J) = (2, -1)$ for ytterbium. We find that the dominant loss process is to the Yb $^3P_2, m_J = -2$ manifold (see Fig. 4(b)), suggesting that the inelastic rate can be reduced significantly by eliminating this decay channel in future experiments. We also see that the contributions are principally from $l \neq 0$ channels, indicating the importance of anisotropic interactions.

V. SUMMARY AND CONCLUSIONS

We observe a strong feature in the inelastic rate of the ^{174}Yb $^3P_2, m_J = -1 + {}^6$Li $^2S_{1/2}, |m_J, m_I\rangle = |-1/2, +1\rangle$ system at 450 G. When combined with a theoretical model of the system which fits the obtained inelastic rate spectrum, this provides evidence for anisotropy-induced magnetic Feshbach resonances in this collisional system. Future work includes a more careful study of the nature of these Li-Yb* resonances and their applicability towards molecule formation. A direct $^1S_0 \rightarrow {}^3P_2(m)$ optical transfer scheme [27] will allow experiments to efficiently access each Zeeman state individually. Of particular interest is the lowest Zeeman state of fermionic ^{173}Yb where the intra-species inelastic effects should be suppressed due to Pauli-blocking of $s-$wave collisions and background inter-species inelastic effects should be reduced from being in the lowest energy collision channel in the $^3P_2$ Zeeman manifold.

We thank Alaina Green for experimental assistance. We gratefully acknowledge financial support from NSF Grants No. PHY-1306647, No. PHY-1308573, AFOSR Grants No. FA9550-12-10051, No. FA9550-14-1-0321, and ARO MURI Grant No. W911NF-12-1-0476.

[1] A. Micheli, G.K. Brennen, and P. Zoller, Nature Physics **2**, 341 (2006).
[2] J.J. Hudson, D.M. Kara, I.J. Smallman, B.E. Sauer, M.R. Tarbutt, and E.A. Hinds, Nature **473**, 493 (2011).
[3] S. Inouye, M.R. Andrews, J. Stenger, H.-J. Miesner, D.M. Stamper-Kurn, W. Ketterle, Nature **392**, 151 (1998).
[4] Ph. Courteille, R.S. Freeland, D.J. Heinzen, F.A. van Abeelen, and B.J. Verhaar, Phys. Rev. Lett. **81**, 69 (1998).
[5] V. Vuletić, A.J. Kerman, C. Chin, and S. Chu, Phys. Rev. Lett. **82**, 1406 (1999).
[6] J.G. Danzl, E. Haller, M. Gustavsson, M.J. Mark, R. Hart, N. Bouloufa, O. Dulieu, H. Ritsch, H-C. Nagerl, Science **321**, 1062 (2008).
[7] K.K. Ni, S. Ospelkaus, M.H.G. de Miranda, A. Peer, B. Neyenhuis, J.J. Zirbel, S. Kotochigova, P.S. Julienne, D.S. Jin, J. Ye, Science **322**, 231 (2008).
[8] V. Ivanov, A. Khromov, A. Hansen, W. Dowd, F. Münchow, A. Jamison, and S. Gupta, Phys. Rev. Lett. **106**, 153201 (2011).
[9] H. Hara, Y. Takasu, Y. Yamaoka, J. Doyle, Y. Takahashi, Phys. Rev. Lett. **106**, 205304 (2011).
[10] B. Pasquiou, A. Bayerle, S.M. Tzanova, S. Stellmer, J. Szczepkowski, M. Parigger, R. Grimm, and F. Schreck, Phys. Rev. A. **88**, 023601 (2013).
[11] F. Baumer, F. Münchow, A. Görlitz, S.E. Maxwell, P.S. Julienne, and E. Tiesinga, Phys. Rev. A **83**, 040702 (2011).
[12] P.S. Zuchowski, J. Aldegunde, and J.M. Hutson, Phys. Rev. Lett. **105**, 153201 (2010).
[13] D. Hansen, J. Mohr, and A. Hemmerich, Phys. Rev. A **67**, 021401 (2003).
[14] S.B. Nagel, C.E. Simien, S. Laha, P. Gupta, V.S. Ashoka, and T.C. Killian, Phys. Rev. A **67**, 011401 (2003).
[15] A. Yamaguchi, S. Uetake, D. Hashimoto, J.M. Doyle, and Y. Takahashi, Phys. Rev. Lett. **101**, 233002 (2008).
[16] S. Kato, S. Sugawa, K. Shibata, R. Yamamoto, and Y. Takahashi, Phys. Rev. Lett. **110**, 173201 (2013).
[17] A. Petrov, E. Tiesinga, and S. Kotochigova, Phys. Rev. Lett. **109**, 103002 (2012).
[18] A. Khramov, A. Hansen, W. Dowd, R. Roy, C. Makrides, A. Petrov, S. Kotochigova, and S. Gupta, Phys. Rev. Lett. **112**, 033201 (2014).
[19] M.L. González-Martínez and J.M. Hutson, Phys. Rev. A **88**, 020701 (2013).
[20] A. Hansen, A. Khramov, W. Dowd, A. Jamison, B. Plotkin-Swing, R. Roy, and S. Gupta, Phys. Rev. A. **87**, 013615 (2013).
[21] C.J. Bowers, D. Budker, S.J. Freedman, G. Gwinner, J.E. Stalnaker, and D. DeMille, Phys. Rev. A **59** 3513 (1999).
[22] The choice to use the $^3P_2, m_J = -1$ state is primarily a technical one. The ideal experiment would use the $m_J = -2$ substate to reduce the number of decay channels for the system. However, our optical pumping scheme will always produce $m_J = -1$ together with

$m_J = -2$. At our optical trap wavelength, there is no relative orientation of electric and magnetic field orientation that produces a sufficiently weaker trap for $m_J = -1$ to facilitate purification via spilling. Transfer of our purified sample to the $m_J = -2$ substate via a radiofrequency pulse would require the polarization of the optical trap to also be rapidly changed to provide sufficient trapping, a technique that could be implemented in the future.

[23] Including these temperature variations in the analysis led to $< 5\%$ variation in the extracted inelastic coefficients, which is smaller than the reported error bars.

[24] The interspecies overlap during the mixture evolution time can be affected by relative cloud center-of-mass motion from small intensity imbalances in the two counterpropagating 404 nm excitation beams, which we experimentally minimize. Another contributor is a small magnetic field gradient along the weakest trap axis which differentially affect the two species.

[25] Z. Idziaszek and P. Julienne, Phys. Rev. Lett. **104**, 113202 (2010)

[26] A. Petrov, C. Makrides, S. Kotochigova, to be published in this issue of New J. Phys. (2015).

[27] S. Uetake, R. Murakami, J. Doyle, and Y. Takahashi, Phys. Rev. A **86**, 032712 (2012).

BIBLIOGRAPHY

[1] M.A. Khamehchi, Y. Zhang, C. Hamner, T. Busch, and P. Engels. Measurement of collective excitations in a spin-orbit-coupled Bose-Einstein condensate. *Physical Review A*, 90:063624, 2014.

[2] M.J.H. Ku, W. Ji, B. Mukherjee, E. Guardado-Sanchez, L.W. Cheuk, T. Yefsah, and M.W. Zwierlein. Motion of a solitonic vortex in the BEC-BCS crossover. *Physical Review Letters*, 113:065301, 2014.

[3] I. Bloch, J. Dalibard, and S. Nascimbène. Quantum simulations with ultracold quantum gases. *Nature Physics*, 8:267-276, 2012.

[4] A.O. Jamison, B. Plotkin-Swing, and S. Gupta. Advances in precision contrast interferometry with Yb Bose-Einstein condensates. *Physical Review A*, 90:063606, 2014.

[5] R. Bouchendira, P. Cladé, S. Guellati-Khélifa, F. Nez, and F. Biraben. New determination of the fine structure constant and test of the quantum electrodynamics. *Physical Review Letters*, 106:080801, 2011.

[6] G. Rosi, L. Cacciapuoti, F. Sorrentino, M. Menchetti, M. Prevedelli, and G.M. Tino. Measurement of the gravity-field curvature by atom interferometry. *Physical Review Letters*, 114:013001, 2015.

[7] A.L. Migdall, J.V. Prodan, W.D. Phillips, T.H. Bergeman, and H.J. Metcalf. First observation of magnetically trapped neutral atoms. *Physical Review Letters*, 54:2596, 1985.

[8] S. Chu, J.E. Bjorkholm, A. Ashkin, and A. Cable. Experimental observation of optically trapped atoms. *Physical Review Letters*, 57:314, 1986.

[9] A. Aspect, J. Dalibard, A. Heidmann, C. Salomon, and C. Cohen-Tannoudji. Cooling atoms with stimulated emission. *Physical Review Letters*, 57:1688, 1986.

[10] M.H. Anderson, J.R. Ensher, M.R. Matthews, C.E. Wieman, and E.A. Cornell. Observation of Bose-Einstein condensation in a dilute atomic vapor. *Science*, 269:198, 1995.

[11] K.B. Davis, M.-O. Mewes, M.R. Andrews, N.J. van Druten, D.S. Durfee, D.M. Kurn, and W. Ketterle. Bose-Einstein condensation in a gas of sodium atoms. *Physical Review Letters*, 75:(22):3969, 1995.

[12] B. DeMarco and D.S. Jin. Onset of Fermi degeneracy in a trapped atomic gas. *Science*, 285: 1703, 1999.

[13] N. Hinkley, J.A. Sherman, N.B. Phillips, M. Schippo, N.D. Lemke, K. Beloy, M. Pizzocaro, C.W. Oates, and A.D. Ludlow. An atomic clock with 10^{-18} instability. *Science*, 341:1215, 2013.

[14] G. Wilpers, T. Binneswies, C. Degenhardt, U. Sterr, J. Helmcke, and F. Riehle. Optical clock with ultracold neutral atoms. *Physical Review Letters*, 89:230801, 2002.

[15] B.J. Bloom, T.L. Nicholson, J.R. Williams, S.L. Campbell, M. Bishof, X. Zhang. W. Zhang, S.L. Bromley, and J. Ye. An optical lattice clock with accuracy and stability at the 10^{-18} level. *Nature*, 506:12941, 2014.

[16] H. Feshbach and E. Lomon. Nucleon-Nucleon scattering. *Physical Review*, 102:891, 1956.

[17] B.S. Rem, A.T. Grier, I. Ferrier-Barbut, U. Eismann, T. Langen, N. Navon, L. Khaykovich, F. Werner, D.S> Petrov, F. Chevy, and C. Salomon. Lifetime of the Bose gas with resonant interactions. *Physical Review Letters*, 110:163202, 2013.

[18] D.E. Miller, J.K. Chin, C.A. Stan, Y. Liu, W. Setiawan, C. Sanner, and W. Ketterle. *Physical Review Letters*, 99:070402, 2007.

[19] J.J. Zirbel, K.-K. Ni, S. Ospelkaus, J.P. D'Incao, C.E. Wieman, J. Ye, and D.S. Jin. *Physical Review Letters*, 100:143201, 2008.

[20] P.K. Molony, P.D. Gregory, Z. Ji, B. Lu, M.P. Köppinger, C. Ruth Le Sueur, C.L. Blackley, J.M. Hutson, and S.L. Cornish. Creation of ultracold $^{87}Rb^{133}Cs$ molecules in the rovibrational ground state. *Physical Review Letters*, 113:255301, 2014.

[21] C. Haimberger, J. Kleinert, M. Bhattacharya, and N.P. Bigelow. Formation and detection of ultracold ground-state polar molecules. *Physical Review A*, 70:021402, 2004.

[22] S. Stellmer, B. Pasquiou, R. Grimm, and F. Schreck. Creation of ultracold Sr_2 molecules in the electronic ground state. *Physical Review Letters*, 109:115302, 2012.

[23] K.-K. Ni, S. Ospelkaus, M.H.G. de Miranda, A. Peer, B. Neyenhuis, J.J> Zirbel, S. Kotochigova, P.S. Julienne, D.S. Jin, and J. Ye. A high phase-space density gas of polar molecules. *Science*, 322:231, 2008

[24] J.G. Danzl, E. Haller, M. Gustavsson, M.J. Mark, R. Hart, N. Bouloufa, O. Dulieu, H. Ritsch, H.-C. Nägerl. Quantum gas of deeply bound ground state molecules. *Science*, 321:5892, 2008.

[25] E.S. Shuman, J.F. Barry, and D. DeMille. Laser cooling of a diatomic molecule. *Nature*, 467:09443, 2010.

[26] J.F. Barry, D.J. McCarron, E.B. Norrgard, M.H. Steinecker, and D. DeMille. Magneto-optical trapping of a diatomic molecule. *Nature*, 512:13634, 2014.

[27] M.T. Hummon, M. Yeo, B.K. Stuhl, A.L. Collopy, Y. Xia, and J. Ye. 2D magneto-optical trapping of diatomic molecules. *Physical Review Letters*, 110:143001, 2013.

[28] A. Micheli, G.K. Brennen, and P. Zoller. A toolbox for lattice-spin models with polar molecules. *Nature Physics*, 2:341, 2006.

[29] O. Dannenberg, M. Mackie, and K.-A. Suominen. Shortcut to a Fermi-Degenerate gas of molecules via cooperative association. *Physical Review Letters*, 91:210404, 2003.

[30] A.H.H. Hansen. *Interacting Quantum Gases of Lithium and Ytterbium*. PhD thesis, University of Washington, 2013.

[31] A. Khramov. *Experiments in the Ultracold Lithium - Ytterbium System*. PhD thesis, University of Washington, 2013.

[32] C.A. Stan and W. Ketterle. Multiple species atom source for laser-cooling experiments. *Reviews of Scientific Intruments*, 76:063113, 2005.

[33] K. Dieckmann, R.J.C. Spreeuw, M. Weidermüller, and J.T.M. Walraven. Two-dimensional magneto-optical trap as a source of slow atoms. *Physical Review A*, 58:3891, 1998.

[34] A.Y. Khramov, A.H. Hansen, A.O. Jamison, W.H. Dowd, and S. Gupta. Dynamics of Feshbach molecules in an ultracold three-component mixture. *Physical Review A*, 86:032705, 2012.

[35] A.T. Grier, I. Ferrier-Barbut, B.S. Rem, M. Delahaye, L. Khaykovich, F. Chevy, and C. Salomon. Lambda-enhanced sub-Doppler cooling of lithium atoms in D_1 gray molasses. *Physical Review A*, 87:063411, 2013.

[36] P. Hamilton, G. Kim, T. Joshi, B. Mukherjee, D. Tiarks, and H. Müller. Sisyphus cooling of lithium. *Physical Review A*, 89:023409, 2014.

[37] C. Wieman and T.W. Hänsch. Doppler-Free laser polarization spectroscopy. *Physical Review Letters*, 36:1170, 1976.

[38] S. Taie, R. Yamazaki, S. Sugawa, and Y. Takahashi. An SU(6) Mott insulator of an atomic Fermi gas realized by large-spin Pomeranchuk cooling. *Nature Physics*, 8:825, 2012.

[39] K. Honda, Y. Takahashi, T. Kuwamoto, M. Fujimoto, K. Toyoda, K. Ishikawa, and T. Yabuzaki. Magneto-optical trapping of Yb atoms and a limit on the branching ratio of the $^1P_1$ state. *Physical Review A*, 59:R934, 1999.

[40] T. Loftus, J.R. Bochinski, and T.W. Mossberg. Magnetic trapping of ytterbium and the alkaline-earth metals. *Physical Review A*, 66:013411, 2002.

[41] C.J. Bowers, D. Budker, E.D. Commins, D. DeMille, S.J. Freedman, A.-T. Nguyen, and S.-Q. Shang. Experimental investigation of excited-state lifetimes in atomic ytterbium. *Physical Review A*, 53:3103, 1996.

[42] B. Karacoban and L. Özdemir. Energies, Landé factors, and lifetimes for some excited levels of neutral ytterbium (Z=70). *Acta Physica Polonica A*, 119, 2011.

[43] A. Khramov, A. Hansen, W. Dowd, R.J. Roy, C. Makrides, A. Petrov, S. Kotochigova, and S. Gupta. Ultracold heteronuclear mixture of ground and excited state atoms. *Physical Review Letters*, 112:033201, 2014.

[44] A. Yamaguchi, S. Uetake, D. Hashimoto, J.M. Doyle, and Y. Takahashi. Inelastic collisions in optically trapped ultracold metastable ytterbium. *Physical Review Letters*, 101:233002, 2008.

[45] A. Yamaguchi. *Metastable State of Ultracold and QUantum Degenerate Ytterbium Atoms: High-Resolution Spectroscopy and Cold Collisions.* PhD thesis, Kyoto University, 2007.

[46] T. Hong, C. Cramer, E. Cook, W. Nagourney, and E.N. Fortson. Observation of the $^1S_0$-$^3P_0$ transition in atomic ytterbium for optical clocks and qubit arrays. *Optical Letters*, 30:2644, 2005.

[47] K.-K. Ni, S. Ospelkaus, D. Wang, G. Quemener, B. Neyenhuis, M.H.G. deMiranda, J. Bohn, J. Ye, and D. Jin. Dipolar collisions of polar molecules in the quantum regime. *Nature*, 464:1324, 2010.

[48] S. Uetake, A. Yamaguchi, D. Hashimoto, and Y. Takahashi. High-resolution laser spectroscopy of ultracold yttebrium atoms using spin-forbidden electric quadrupole transition. *Applied Physics B*, 93:409, 2008.

[49] A.M. Kaufman, B.J. Lester, and C.A. Regal. Cooling a single atom in an optical tweezer to its quantum ground state. *Physical Review X*, 2:041014, 2012.

[50] E.L. Raab, M. Prentiss, A. Cable, S. Chu, and D. Pritchard. Trapping of neutral sodium atoms with radiation pressure. *Physical Review Letters*, 59:2631, 1987.

[51] G. Nienhuis, P. Van der Straten, and S.-Q. Shang. Operator description o flaser cooling below the Doppler limit. *Physical Review A*, 44:462, 1991.

[52] R. Grimm, M. Weidemüller, and Y.B. Ovchinnikov. Optical dipole traps for neutral atoms. *Advances in Atomic, Molecular, and Optical Physics*, 42:95, 200.

[53] J.D. Miller, R.A. Cline, and D.J. Heinzen. Far-off-resonance optical trapping of atoms. *Physical Review A*, 47:R4567(R), 1993.

[54] H. Hara, H. Konishi, S. Nakajima, Y. Takasu, and Y. Takahashi. *Journal of the Physical Society of Japan*, 83:014003, 2013.

[55] D. Jaksch, C. Bruder, J.I. Cirac, C.W. Gardiner, and P. Zoller. Cold bosonic atoms in optical lattices. *Physical Review Letters*, 81:3108, 1998.

[56] K.M. O'Hara, M.E. Gehm, S.R. Granade, and J.E. Thomas. Scaling laws for evaporative cooling in time-dependent optical traps. *Physical Review A*, 64:051403(R), 2001.

[57] F.A. van Abeelen, B.J. Verhaar, and A.J. Moerdijk. Sympathetic cooling of ^6Li atoms. *Physical Review A*, 55:4377, 1997.

[58] S.R. Granade, M.E. Gehm, K.M. O'Hara, and J.E. Thomas. All-optical production of a degenerate Fermi gas. *Physical Review Letters*, 88:120405, 2002.

[59] A.H. Hansen, A.Y. Khramov, W.H. Dowd, A.O. Jamison, B. Plotkin-Swing, R.J. Roy, and S. Gupta. Production of quantum-degenerate mixtures of ytterbium and lithium with controllable interspecies overlap. *Physical Review A*, 87:013615, 2012.

[60] A.H. Hansen, A. Khramov, W.H. Dowd, A.O. Jamison, V.V. Ivanov, and S. Gupta. Quantum degenerate mixture of ytterbium and lithium atoms. *Physical Review A*, 84:011606(R), 2011.

[61] R.J. Dodd, M. Edwards, C.J. Williams, C.W. Clark, M.J. Holland, P.A. Reprecht, and K. Burnett. *Physical Review A*, 54:661, 1996.

[62] M.W. Zwierlein, C.A. Stan, C.H. Schunck, S.M.F. Raupach, A.J. Kerman, and W. Ketterle. *Physical Review Letters*, 92:120403, 2004.

[63] S. Giorgini, L.P. Pitaevskii, and S. Stringari. Theory of ultracold atomic Fermi gases. *Reviews of Modern Physics*, 80:1215, 2008.

[64] Y. Sagi, T.E. Drake, R. Paudel, R. Chapurin, and D.S. Jin. Probing local quantities in a strongly interacting Fermi gas. *Journal of Physics: Conference Series*, 467:012010, 2013.

[65] F. Baumer, F. Münchow, A. Görlitz, S.E. Maxwell, P.S. Julienne, and E. Tiesinga. Spatial separation in a thermal mixture of ultracold ^{174}Yb and ^{87}Rb atoms. *Physical Review A*, 83:040702(R), 2011.

[66] S. Kotochigova, T. Zelevinsky, and J. Ye. Prospects for application of ultracold Sr_2 molecules in precision measurements. *Physical Review A*, 79:012504, 2009.

[67] P. Zhang, H.R. Sadeghpour, and A. Dalgarno. Structure and spectroscopy of ground and excited states of LiYb *Journal of Chemical Physics*, 133:044306, 2010.

[68] A. Derevianko, J.F. Babb, and A. Dalgarno High-precision calculations of van der Waals coefficients for heteronuclear alkali-metal dimers. *Physical Review A*, 63:052704, 2001.

[69] M.S. Safronova, S.G. Porsev, and C.W. Clark. Ytterbium in quantum gases and atomic clocks: van der Waals interactions and blackbody shifts. *Physical Review Letters*, 109:230802, 2012.

[70] R. Côté, A. Dalgarna, Y. Sun, and R.G. Hulet. Photoabsorption by ultracold atoms and the scattering length. *Physical Review Letters*, 74:3581, 1995.

[71] M. Kitagawa, K. Enomoto, K. Kasa, Y. Takahashi, R. Ciurylo, P. Naidon, and P.S. Julienne. *Physical Review A*, 77:012719, 2008.

[72] V.V. Ivanov, A. Khramov, A.H. Hansen, W.H. Dowd, F. Münchow, A.O. Jamison, and S. Gupta. Sympathetic cooling in an optically trapped mixture of alkali and spin-singlet atoms. *Physical Review Letters*, 106:143201, 2011.

[73] H. Hara, Y. Takasu, Y. Yamaoka, J.M. Doyle, and Y. Takahashi. Quantum degenerate mixtures of alkali and alkaline-earth-like atoms. *Physical Review Letters*, 106:205304, 2011.

[74] M. Mudrich, S. Kraft, K. Singer, R. Grimm, A. Mosk, and M. Weidemüller. Sympathetic cooling with two atomic species in an optical trap. *Physical Review Letters*, 88:253001, 2002.

[75] C. Chin, R. Grimm, P. Julienne, and E. Tiesinga. Feshbach resonances in ultracold gases. *Review of Modern Physics*, 82:1225, 2010.

[76] M. Houbiers, H.T.C. Stoof, W.I. McAlexander, and R.G. Hulet. Elastic and inelastic collisions of ^6Li atoms in magnetic and optical traps.

[77] C.H. Schunck, M.W. Zwierlein, C.A. Stan, S.M.F. Raupach, W. Ketterle, A. Simoni, E. Tiesinga, C.J. Williams, and P.S. Julienne. Feshbach resonances in fermionic ^{6}Li. *Physical Review A*, 71:045601, 2005.

[78] E. Hodby, S.T. Thompson, C.A. Regal, M. Greiner, A.C. Wilson, D.S. Jin, E.A. Cornell, and C.E. Weiman. Production efficiency of ultracold Feshbach molecules in bosonic and fermionic systems. *Physical Review Letters*, 94:120402, 2005.

[79] K. Bergmann, H. Theuer, and B.W. Shore. Coherent population transfer among quantum states of atoms and molecules. *Reviews of Modern Physics*, 70:1003, 1998.

[80] D.A. Brue and J.M. Hutson. Magnetically tunable Feshbach resonances in ultracold Li-Yb mixtures. *Physical Review Letters*, 108:043201, 2012.

[81] R.V. Krems, G.C> Groenenboom, and A. Dalgarno. Electronic interaction anisotropy between atoms in arbitrary angular momentum states. *Journal of Physical Chemistry*, 108:8941, 2004.

[82] A. Petrov, E. Tiesinga, and S. Kotochigova. Anisotropy-induced Feshbach resonances in a quantum dipolar gas of highly magnetic atoms. *PHysical Review Letters* 109:103002, 2012.

[83] S. Kato, S. Sugawa, K. Shibata, R. Yamamoto, and Y. Takahashi. Control of resonant interaction between electronic ground and excited states. *Physical Review Letters*, 110:173201, 2013.

[84] W. Dowd, R.J. Roy, R.K. Shrestha, A. Petrov, C. Makrides, S. Kotochigova, and S. Gupta. Magnetic field dependent interactions in an ultracold Li-Yb($^3P_2$) mixture. arXiv:1412.5690, 2014.

[85] C. Bowers, D. Budker, E. Commins, D. DeMille, S. Freedman, A. Nguyen, and S. Shang. Experimental investigation of excited-state lifetimes in atomic ytterbium. *Physical Review A*, 53:3103, 1996.

[86] M.L. GonzÍez-Martńez and J.M. Hutson. Magnetically tunable Feshbach resonances in Li + Yb (^3P_J). *Physical Review A*, 88:020701(R), 2013.

[87] A. Petrov, C. Makrides, and S. Kotochigova. Magnetic control of ultra-cold ^{6}Li and ^{174}Yb($^3P_2$) atom mixtures with Feshbach resonances. arXiv:1502.04973, 2015.